

Cause-and-effect of linear mechanisms sustaining wall turbulence

Adrián Lozano-Durán^{1†}, Navid C. Constantinou²,
Marios-Andreas Nikolaidis³, and Michael Karp¹

¹Center for Turbulence Research, Stanford University, CA 94305, USA

²Research School of Earth Sciences and ARC Centre of Excellence for Climate Extremes,
Australian National University, Canberra ACT 2601, Australia

³Department of Physics, National and Kapodistrian University of Athens, Athens 157 72,
Greece

(Received xx; revised xx; accepted xx)

Despite the nonlinear nature of turbulence, there is evidence that part of the energy-transfer mechanisms sustaining wall turbulence can be ascribed to linear processes. The different scenarios stem from linear stability theory and comprise exponential instabilities, neutral modes, transient growth from non-normal operators, and parametric instabilities from temporal mean-flow variations, among others. These mechanisms, each potentially capable of leading to the observed turbulence structure, are rooted in simplified physical models. Whether the flow follows any or a combination of them remains elusive. Here, we evaluate the linear mechanisms responsible for the energy transfer from the streamwise-averaged mean-flow (\mathbf{U}) to the fluctuating velocities (\mathbf{u}'). To that end, we use cause-and-effect analysis based on interventions: manipulation of the causing variable leads to changes in the effect. This is achieved by direct numerical simulation of turbulent channel flows at low Reynolds number, in which the energy transfer from \mathbf{U} to \mathbf{u}' is constrained to preclude a targeted linear mechanism. We show that transient growth is sufficient for sustaining realistic wall turbulence. The self-sustaining cycle of turbulence persists when exponential instabilities, neutral modes, and parametric instabilities of the mean flow are suppressed. We further show that a key component of transient growth is the Orr/push-over mechanism induced by spanwise variations of the base flow. Finally, we demonstrate that an ensemble of simulations with various frozen-in-time \mathbf{U} arranged so that only transient growth is active, can faithfully represent the energy transfer from \mathbf{U} to \mathbf{u}' as in realistic turbulence. Our approach provides direct cause-and-effect evaluation of the linear energy-injection mechanisms from \mathbf{U} to \mathbf{u}' in the fully nonlinear system and simplifies the conceptual model of self-sustaining wall turbulence.

Key words:

1. Introduction

Turbulence is a highly nonlinear phenomenon. Nevertheless, there is ample agreement that some of the processes sustaining wall-turbulence can be faithfully represented by linearising the equations of motion about an appropriate reference flow state, i.e., base flow (Malkus 1956; Reynolds & Tiederman 1967; Hussain & Reynolds 1970; Landahl

† Email address for correspondence: adrianld@stanford.edu

1975; Butler & Farrell 1993; Jiménez 2013). One of these processes is the transfer of kinetic energy from the mean flow to the fluctuating velocities. The different mechanisms originate from linear stability theory and constitute the foundations of many control and modelling strategies (e.g. Kim & Bewley 2006; Schmid & Henningson 2012; McKeon 2017; Rowley & Dawson 2017; Zare *et al.* 2020; Jovanović 2020). As such, establishing the relevance of a particular theory is consequential to comprehend, model, and control the structure of wall-bounded turbulence by linear methods (e.g. Höglberg *et al.* 2003; Del Álamo & Jiménez 2006; Hwang & Cossu 2010c; Zare *et al.* 2017; Morra *et al.* 2019; Towne *et al.* 2020). Despite the ubiquity of linear theories, their significance in wall turbulence remains outstanding. One of the main limitations to assess the role of a concrete linear process in the flow has been the lack of conclusive cause-and-effect assessment of the mechanisms in question. In the present work, we devise a collection of numerical experiments of turbulent flows over a flat wall, in which the Navier–Stokes equations are minimally altered to suppress the causal link entailing the energy-transfer from the mean flow to the fluctuating velocities via various linear mechanisms.

Before diving into the intricacies of the different linear mechanisms, one may ask why we should insist on describing this energy transfer using linear theories if turbulence is undoubtedly a nonlinear phenomenon. One reason is that the energy source for fluctuations in wall turbulence is controlled by spatial changes in the mean velocity (i.e, mean shear) (Batchelor & Proudman 1954; Brown & Roshko 1974; Jiménez 2013). When the flow is decomposed into a mean velocity (\mathbf{U}) and fluctuations (\mathbf{u}'), the equations naturally reduce to a system with a linear term and a nonlinear term,

$$\frac{\partial \mathbf{u}'}{\partial t} = \underbrace{\mathcal{L}(\mathbf{U})\mathbf{u}'}_{\substack{\text{linear} \\ \text{processes}}} + \underbrace{\mathbf{N}(\mathbf{u}')}_{\substack{\text{nonlinear} \\ \text{processes}}}. \quad (1.1)$$

Under some conditions (see §2.2), the linear term in (1.1) is the sole source of energy for \mathbf{u}' , which explains the unceasing surge of interest in linear theories. It has been demonstrated in many occasions that numerous features of the energy-containing scales can be elucidated from the linear dynamics in (1.1) (e.g., Reed *et al.* 1996; Cambon & Scott 1999; Schmid 2007; McKeon 2017). This is the case for strongly inhomogeneous environments, such as wall turbulence with large-scale pressure or body forces imposed (e.g., in the streamwise direction), and geophysical flows, in which rotation and stratification impose strong constraints on the flow (Farrell & Ioannou 2019). An additional (less glamorous) motivation for the use of linear theories is a matter of practicality: our current framework to analyse linear systems is well beyond the tools to understand nonlinear equations. Hence, inasmuch the linear equations meaningfully represents the physics of the problem, linear tools greatly aid the analysis and facilitate the development of prediction and control strategies.

The rationale behind the formulation and validation of a linear theory for the energy transfer between flow structures comprises four elements: (i) the existence in wall turbulence of recurrent fluid motions (or coherent structures) involved in a self-sustaining process, (ii) the selection of a base flow which (iii) enables the prediction of these coherent motions via linear theory, and (iv) a cause-and-effect framework to evaluate the presence of the linear mechanism in actual nonlinear turbulence. These four points are discussed below.

1.1. Coherent structures and self-sustaining wall turbulence

Since the experiments by Klebanoff *et al.* (1962); Kline *et al.* (1967) and Kim *et al.* (1971), it was realised that despite the conspicuous disorder of wall turbulence, the flow in the vicinity of walls can be apprehended as a collection of recurrent patterns, usually referred to as coherent structures (Richardson 1922). Of particular interest are those structures carrying most of the kinetic energy and momentum, further categorised as streaks (regions of high and low velocity aligned with the mean-flow direction) and rolls/vortices (regions of rotating fluid) (Robinson 1991; Panton 2001; Adrian 2007; Smits *et al.* 2011; Jiménez 2012, 2018).

Close to the wall in the so-called buffer layer, the current consensus is that these energy-containing structures are involved in a quasi-periodic self-sustaining process and that their space-time structure plays a crucial role in the maintenance of shear-driven turbulence (e.g. Kim *et al.* 1971; Jiménez & Moin 1991; Butler & Farrell 1993; Hamilton *et al.* 1995; Waleffe 1997; Jiménez & Pinelli 1999; Schoppa & Hussain 2002; Farrell & Ioannou 2012; Jiménez 2012; Constantinou *et al.* 2014; Farrell *et al.* 2016, 2017a). The self-sustaining process is based on the emergence of streaks from wall-normal ejections of fluid (Landahl 1975) followed by the meandering and breakdown of the newborn streaks (Swearingen & Blackwelder 1987; Waleffe 1995, 1997; Kawahara *et al.* 2003). The cycle is restarted by the generation of new vortices from the perturbations created by the disrupted streaks. The interwoven relation between vortices and streaks was demonstrated by Jiménez & Pinelli (1999), who showed that damping out either of them inevitably interrupts the turbulence cycle. A similar but more disorganised scenario is hypothesised to occur for the larger energy-containing structures further away from the wall within the logarithmic layer (e.g. Flores & Jiménez 2010; Hwang & Cossu 2011; Cossu & Hwang 2017; Lozano-Durán *et al.* 2019), although the focus of the present work is on the buffer layer (i.e. low Reynolds numbers). Linear theories have been instrumental in unfolding and explaining various stages of the self-sustaining process, and the existence of coherent structures has aided the selection of particular base flows to linearise the equations of motion.

The self-sustaining nature of wall turbulence has also been investigated from the viewpoint of dynamical-systems theory. In this framework, the spatio-temporal structure of turbulence is thought of as a low-dimensional manifold around which the dynamical system spends a substantial fraction of time (Jiménez 1987). According to the dynamical-systems perspective, the simplest description of turbulence is then given by a collection of fixed points and unstable periodic orbits embedded in a high-dimensional turbulent attractor (Kawahara *et al.* 2012). The first dynamical-system investigations of turbulence in shear flows began with the discovery of nonlinear equilibrium states, referred to as ‘exact coherent structures’, of Couette flow (Nagata 1990). Since then, there have been multiple descriptions of such equilibrium states in shear flows in channels and pipes, often involving unstable travelling waves (e.g., Waleffe 2001; Kawahara & Kida 2001; Wedin & Kerswell 2004; Gibson *et al.* 2009; van Veen & Kawahara 2011; Kreilos & Eckhardt 2012; Park & Graham 2015; Hwang *et al.* 2016). Particularly relevant for the study of self-sustaining processes is the discovery of time-periodic solutions by Kawahara & Kida (2001) and later by others (e.g., Toh & Itano 2003; Viswanath 2007; Kawahara *et al.* 2012). These time-periodic solutions were first found for plane Couette flow and exhibited a full regeneration cycle comprising the formation and breakdown of streamwise vortices and low-velocity streaks. The simplicity provided by these solutions has facilitated the inspection for linear processes at a given stage in the self-sustaining cycle. However, while realistic turbulence does share some similarities with these exact coherent solutions, the

latter have been restricted to very low Reynolds numbers. The actual dynamics of wall turbulence are significantly more complex and chaotic, and the relationship of realistic high-Reynolds number turbulent flows with the exact coherent states interpretation remains unsettled.

Another theoretical nonlinear framework to describe self-sustaining processes and transition has been proposed by Hall & Smith (1988) and Hall & Smith (1991) in terms of vortex–wave interactions (VWI). The approach has been shown to be the equivalent high-Reynolds-number representation of the exact coherent structures discussed above (Hall & Sherwin 2010). VWI theory involves an intricately delicate balance between an unstable wave, a roll and a streak. According to VWI, a single downstream propagating wave interacts with itself to produce a spanwise periodic stress jump which drives a roll. The roll then interacts with a neutrally stable mean streamwise flow to produce a streak. Subsequent developments of the VWI theory include extensions to laminar to turbulent transition (Wang *et al.* 2007) and multiscale motions consistent with the logarithmic layer (Hall 2018). Other descriptions of self-sustaining turbulence in the vein of VWI include studies by Deguchi *et al.* (2013) and Deguchi & Hall (2015), and the semi-analytic model by Chini *et al.* (2017) and Montemuro *et al.* (2020); the latter devoted to the formation and maintenance of uniform momentum zones and interlaced vortical fissures. While the theories above could provide a plausible explanation for how turbulence self-sustains, we are still lacking direct evidence regarding whether one or a combination of the above-mentioned mechanisms are actually at work in realistic turbulent flows.

1.2. Base flow

In formulating a linear theory, the flow is decomposed into two components: a base flow defined through some averaging procedure over the instantaneous flow, and fluctuations (or perturbations) about that base flow. The existence of coherent structures in wall turbulence has motivated the selection of particular base flows to linearise the flow about, such that these base flows are the seeds for the inception of new coherent structures consistent with observations in real turbulence. The resulting distorted flow might be used again as a base flow, which describes the generation of new coherent structures and so forth. In this manner, the ultimate cause maintaining turbulence is conceptualised as the energy transfer from the base flow to the fluctuating flow, as sketched in figure 1. The selection of the base flow stands as the most important decision in the linearisation process, as the physical mechanisms ascribed to the linearised equations depend crucially on this choice.

Hereafter, we consider the turbulent flow over a flat plate where x , y and z are the streamwise, wall-normal and spanwise directions respectively; see figure 1. Common choices for the base flow are the average of the streamwise velocity u over homogeneous directions (x and z) and time (t), denoted by $\langle u \rangle_{xzt}$, or only over x or z , denoted by $\langle u \rangle_x$ and $\langle u \rangle_z$, respectively. The notation $\langle u \rangle_{ij\dots}$ denotes averaging over the coordinates i, j, \dots , and it is formally introduced in §2. In turbulent boundary layers and channels, the y -dependent base flow $\langle u \rangle_{xzt}$ has been successful in predicting the formation of streaks, a process sometimes referred to as primary instability. The resulting streaky base flow (now represented by $\langle u \rangle_x$) can be utilised as the new base flow to generate the subsequent vortices or, more generally, disorganised fluctuations. This process is usually referred to as secondary instability.

1.3. Linear theories of self-sustaining wall turbulence

Several linear mechanisms have been proposed as plausible scenarios to rationalise the transfer of energy from the large-scale mean flow to the fluctuating velocities. We discuss

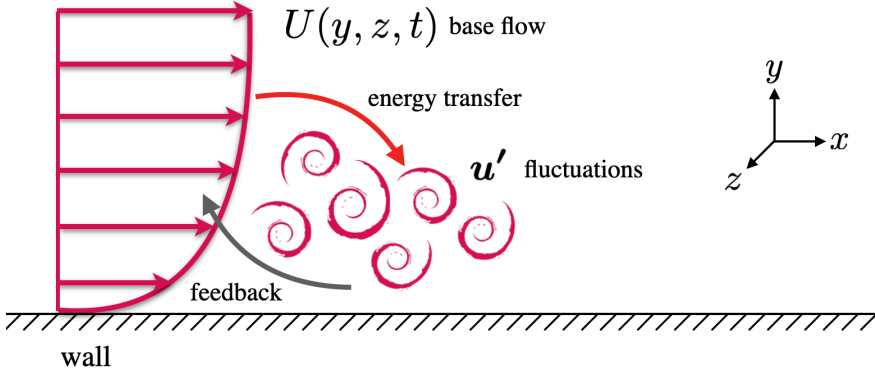


Figure 1: Schematic of the energy transfer from the base flow $\mathbf{U} = U(y, z, t)\hat{x}$ to the fluctuating velocities \mathbf{u}' . The energy transfer (red arrow) from \mathbf{U} to \mathbf{u}' can be investigated via the linear dynamics of the governing equation of \mathbf{u}' . The cycle is closed by the nonlinear feedback from \mathbf{u}' back to \mathbf{U} (gray arrow).

below the linear processes ascribed to two of the most widely used base flows, namely, the y -dependent streakless mean velocity profile $\langle u \rangle_{xzt}$, and the $y-z$ -dependent time-varying streaky base flow $\langle u \rangle_x$. The predictions by the two base flows should not be considered contradictory but rather complementary, as the former might be thought as the cause of the latter.

In fact, it is generally agreed that the linearisation about $\langle u \rangle_{xzt}$ is able to explain the formation of the streaks $U_{\text{streak}} = \langle u \rangle_x - \langle u \rangle_{xzt}$. The process involves the redistribution of fluid near the wall by streamwise vortices leading to the formation of streaks through a combination of the Orr/lift-up mechanisms (Orr 1907; Landahl 1975; Lee *et al.* 1990; Farrell & Ioannou 1993a; Butler & Farrell 1993; Kim & Lim 2000; Jiménez 2012; Encinar & Jiménez 2020). In this case, the base flow, while being exponentially stable, supports the growth of perturbations for a period of time due to the non-normality of the linear operator about that very base flow; a process referred to as non-modal transient growth (e.g. Gustavsson 1991; Trefethen *et al.* 1993; Butler & Farrell 1993; Farrell & Ioannou 1996; Del Álamo & Jiménez 2006; Schmid 2007; Cossu *et al.* 2009). Other studies suggest that the generation of streaks is due to the structure-forming properties of the linearised Navier–Stokes operator, independent of any organised vortices (Chernyshenko & Baig 2005), or due to the interaction of the background free-stream turbulence and the roll-streak structures (Farrell *et al.* 2017b), but the non-modal nature of the linear operator is still crucially invoked. Input–output analysis of the linearised Navier–Stokes equations has also been successful in characterising the non-modal response of the base flow $\langle u \rangle_{xzt}$ (Farrell & Ioannou 1993b; Jovanović & Bamieh 2005; Hwang & Cossu 2010a; Zare *et al.* 2017; Ahmadi *et al.* 2019; Jovanović 2020). The approach combines the linearised Navier–Stokes equations with harmonic or stochastic forcing (white or coloured in time) to qualitatively predict structural features of turbulent shear flows. Similarly, resolvent analysis (McKeon & Sharma 2010; McKeon 2017) provides pairs of response and nonlinear-forcing modes consistent with the linear Navier–Stokes operator with respect to the base flow $\langle u \rangle_{xzt}$ and enables the identification of the most amplified energetic motions in wall turbulent flows. A key aspect of the latter energy transfer is the formation

of critical layers or regions where the wave velocity is equal to the base flow (see also Moarref *et al.* 2013). Note that both input–output and resolvent analysis formulate the problem in the frequency domain, and the sustained response of the perturbations should be understood through a persistent forcing in time. These amplification mechanisms can be classified as resonant or pseudoresonant, depending on whether the amplification of perturbations is associated with modal instabilities or non-normality of the operator, respectively. Interestingly, the flow structures responsible for the energy transfer obtained in the frequency-domain are remarkably similar to the structures identified with non-normal transient growth posed as an initial value problem (Hwang & Cossu 2010b; Symon *et al.* 2018), i.e. the genesis of streaks from cross flow perturbation via Orr/lift-up mechanism. Here, we favour the time-domain formulation over the frequency-domain approach as the former is easily understood as a sequence of events, which facilitates the cause-and-effect analysis of self-sustaining turbulence.

The scenarios described in the paragraph above pertain to the study of y -dependent base flows and, as such, are concerned with primary instability processes. The summary of studies in the left column of table 1 shows that, except for a handful of studies performed under very particular conditions, most investigations advocate for transient growth as the main cause for the genesis of the streamwise streaks via energy transfer from $\langle u \rangle_x$ to U_{streak} . Indeed, the few works which do not support the transient growth are from the 1950's or performed in a different context, such as transition. There is hardly any controversy regarding the formation of the streaks, and here we focus on the linear mechanisms underpinned by $\langle u \rangle_x$ once the streak is formed.

We take our base flow \mathbf{U} to consist of the instantaneous streamwise-averaged velocity $U(y, z, t) = \langle u \rangle_x$ in the streamwise direction with zero wall-normal and spanwise flow, i.e., $\mathbf{U} = (U, 0, 0)$. Our choice is supported by previous studies in the literature, and most of the works reported on table 1 (right column) conducted their analysis by linearising the equations of motion about $U(y, z, t)$. Yet, there is no obvious *a priori* justification for selecting $U(y, z, t)$ in favour of other alternative base flows, and one of the goals here is to investigate whether $U(y, z, t)$ is a meaningful choice to describe the energy transfer from the large scales to the fluctuating flow.

The linear mechanisms supported by $U(y, z, t)$ can be categorised into three groups: (i) modal instability of the mean streamwise flow, (ii) non-modal transient growth, and (iii) non-modal transient growth assisted by parametric instability of the time-varying base flow. Table 1 (right columns) compiles the literature in favour of one or other mechanism. The table, while not an exhaustive compilation of existing works on the topic, hints at a lack of consensus on which is the prevailing linear mechanism responsible for the energy transfer from the streaky mean-flow to the fluctuations, or if any, it implies that the dominant idea is that exponential instability is the one responsible. We show in this work that the latter is not the case; modal instabilities of the mean streamwise flow are not crucial for self-sustaining turbulence. Next, we briefly describe mechanisms (i), (ii) and (iii).

In mechanism (i), it is hypothesised that the energy is transferred from the mean flow $U(y, z, t)$ to the fluctuating flow through modal inflectional instability in the form of strong flow variations in the spanwise direction (Hamilton *et al.* 1995; Waleffe 1997; Karp & Cohen 2017) or wall-normal direction (Chini *et al.* 2017; Montemuro *et al.* 2020), corrugated vortex sheets (Kawahara *et al.* 2003), or intense localised patches of low-momentum fluid (Andersson *et al.* 2001; Hack & Moin 2018). Inasmuch as the instantaneous realisations of the streaky flow are strongly inflectional, the flow $U(y, z, t)$ is invariably unstable at a frozen instant of time (Lozano-Durán *et al.* 2018). These inflectional instabilities are markedly robust and, therefore, their excitation has been

Reference	Linear mechanism for y -dependent base flow $\langle u \rangle_{xzt}$	Reference	Linear mechanism for (y, z) -dependent base flow $\langle u \rangle_x$
Malkus (1956)	NEU	Schoppa & Hussain (2002)	TG
Kim <i>et al.</i> (1971)	EXP (V)	Hoeppfner <i>et al.</i> (2005)	TG & EXP (S)
Skote <i>et al.</i> (2002)	EXP (V)	de Giovanetti <i>et al.</i> (2017)	TG & EXP (S)
Jovanović & Bamieh (2005)	EXP/TG	Cassinelli <i>et al.</i> (2017)	TG & EXP (S)
Landahl (1990)	TG	Farrell & Ioannou (2012)	TG PARA
Lee <i>et al.</i> (1990)	TG	Thomas <i>et al.</i> (2015)	TG PARA
Reddy & Henningson (1993)	TG	Farrell <i>et al.</i> (2016)	TG PARA
Butler & Farrell (1993)	TG	Nikolaidis <i>et al.</i> (2016)	TG PARA
Trefethen <i>et al.</i> (1993)	TG	Swearingen & Blackwelder (1987)	EXP (S)
Kim & Lim (2000)	TG	Hall & Smith (1991)	EXP (S)
Chernyshenko & Baig (2005)	TG	Yu & Liu (1991)	EXP (S)
Del Álamo & Jiménez (2006)	TG	Yu & Liu (1994)	EXP (S)
Cossu <i>et al.</i> (2009)	TG	Li & Malik (1995)	EXP (S/V)
Pujals <i>et al.</i> (2009)	TG	Park & Huerre (1995)	EXP (S)
Hwang & Cossu (2010b)	TG	Hamilton <i>et al.</i> (1995)	EXP (S)
Hwang & Cossu (2010a)	TG	Bottaro & Klingmann (1996)	EXP (S)
McKeon & Sharma (2010)	TG	Waleffe (1997)	EXP (S)
Jiménez (2013)	TG	Reddy <i>et al.</i> (1998)	EXP (S)
Alizard (2015)	TG	Andersson <i>et al.</i> (2001)	EXP (S)
Jiménez (2015)	TG	Asai <i>et al.</i> (2002)	EXP (S)
Encinar & Jiménez (2020)	TG	Kawahara <i>et al.</i> (2003)	EXP (S)
		Hall & Sherwin (2010)	EXP (S)
		Marquillie <i>et al.</i> (2011)	EXP (S)
		Park <i>et al.</i> (2011)	EXP (S)
		Alizard (2015)	EXP (S)
		Chini <i>et al.</i> (2017)	EXP (V)
		Hack & Moin (2018)	EXP (V)
		Montemuro <i>et al.</i> (2020)	EXP (V)
		Wang <i>et al.</i> (2007)	NEU
		Hall & Sherwin (2010)	NEU
		Deguchi <i>et al.</i> (2013)	NEU
		Deguchi & Hall (2015)	NEU
		Hall (2018)	NEU

Table 1: Proposed linear mechanisms responsible for the energy transfer from the base flow to fluctuations for: left-columns, y -dependent base flows (primary instability); right-columns, (y, z) -dependent base flows (secondary instability). Mechanisms are abbreviated as: EXP, exponential instability; TG, transient growth; TG PARA, transient growth assisted by parametric instability; NEU, modally neutral. For EXP, V and S refer to varicose and sinuous instabilities, respectively. The work by Hack & Moin (2018) considered a (x, y, z) -dependent base flow, but it was included in the right-columns as it is devoted to the study of secondary instability. The label TG for studies formulated in the frequency-domain should be understood as pseudoresonant amplification of perturbations due to non-normality of the linear operator. Swearingen & Blackwelder (1987); Yu & Liu (1991, 1994); Hall & Smith (1991); Bottaro & Klingmann (1996); Li & Malik (1995); Park & Huerre (1995) study the secondary instability in Taylor-Görtler vortices. Asai *et al.* (2002); Bottaro & Klingmann (1996); Park & Huerre (1995); Reddy & Henningson (1993); Hoeppfner *et al.* (2005); Jovanović & Bamieh (2005); Wang *et al.* (2007) investigate laminar-to-turbulent transition and suggest that the mechanism might be at play in the turbulent regime. The works by Kim *et al.* (1971); Swearingen & Blackwelder (1987); Bottaro & Klingmann (1996) and Asai *et al.* (2002) are laboratory experiments, whereas the remainder are numerical investigations. Farrell & Ioannou (2012); Thomas *et al.* (2015); Farrell *et al.* (2016); Nikolaidis *et al.* (2016) are carried out in the context of Restricted NonLinear Navier-Stokes. Additionally, some works focus on the buffer layer, logarithmic layer, or outer layer. The table highlights one or two linear mechanisms from each reference, but many works acknowledge the presence of other mechanisms which are not mentioned in the table. The reader is referred to each particular work for details.

proposed to be the mechanism that replenishes the perturbation energy of the turbulent flow (Hamilton *et al.* 1995; Waleffe 1997; Andersson *et al.* 2001; Kawahara *et al.* 2003; Marquillie *et al.* 2011; Hack & Zaki 2014; Hack & Moin 2018). Other studies have speculated that the streaky base flow $U(y, z, t)$ might originate from the primary Taylor-Görtler instability. In this case, the varying wall shear induced by large scales structures gives rise to sufficient streamline curvature in x to trigger the instability (Brown & Thomas 1977; Phillips *et al.* 1996; Saric *et al.* 2003). Consequently, it has also been hypothesised that the following secondary exponential instability of the Taylor-Görtler base-flow is the mechanisms to generate turbulence fluctuations (Swearingen & Blackwelder 1987; Yu & Liu 1991, 1994; Hall & Smith 1991; Bottaro & Klingmann 1996; Li & Malik 1995; Park & Huerre 1995; Karp & Hack 2018). Exponential instabilities above are commonly classified according to their symmetries as varicose and sinuous. The varicose instability (symmetric in the streamwise and wall-normal velocities) is commonly associated with inflection points in the base flow along the wall-normal direction, while the sinuous instability (symmetric in the spanwise velocity) relates to inflection points in the spanwise directions (Schmid & Henningson 2012). In all of the scenarios above, the exponential instability of the streak is thought to be central to the maintenance of wall turbulence. Additionally, the modal character of the base flow also plays a key role in the VWI theory, in which it is postulated that the regeneration cycle is supported by the interaction of a roll with the neutrally stable mean streamwise-flow (Hall & Smith 1991; Deguchi *et al.* 2013; Hall 2018).

Mechanism (ii), transient growth, involves the redistribution of energy from the streak to the fluctuations via transient algebraic amplification. The transient growth scenario of the streaky base flow $U(y, z, t)$ (not to be confused with the transient growth of $\langle u \rangle_{xzt}(y)$ discussed above) gained popularity since the work by Schoppa & Hussain (2002), who argued that transient growth may be the most relevant mechanism not only for streak formation but also for their eventual breakdown. Schoppa & Hussain (2002) showed that most streaks detected in actual wall-turbulence simulations are indeed exponentially stable for the set of wavenumbers considered. Hence, the loss of stability of the streaks would be better explained by the transient growth of perturbations that would lead to vorticity sheet formation and nonlinear saturation. The findings by Schoppa & Hussain (2002) have long been criticised, and the absence of unstable streaks can be also interpreted as an indication that instability is important, as the unstable streaks break fast and are harder to observe. Other criticism argues that, far from the wall, streaks might not provide a reservoir of energy large enough to sustain the flow fluctuations (Jiménez 2018). Some authors have further argued that distinguishing between streak transient growth and streak modal instability would be virtually impossible, as both emerge almost concurrently during the streak breakdown (Höpffner *et al.* 2005; de Gioanetti *et al.* 2017; Cassinelli *et al.* 2017), and hence both are driving mechanisms of self-sustaining turbulence.

Finally, mechanism (iii) has been advanced in recent years by Farrell, Ioannou and coworkers (Farrell & Ioannou 1999, 2012; Farrell *et al.* 2016; Nikolaidis *et al.* 2016; Farrell *et al.* 2017a; Bretheim *et al.* 2018). They adopted the perspective of statistical state dynamics (SSD) to develop a tractable theory for the maintenance of wall turbulence. Within the SSD framework, the perturbations are maintained by an essentially time-dependent, parametric instability of the base flow. The concept of “parametric instability” refers here to perturbation growth that is inherently caused by the time-dependence of U . The self-sustaining mechanism proposed by SSD still relies on the highly non-normal streamwise roll and streak structure. However, it differs from other mechanisms above in that it requires the time-variations of U for the growth of perturbations to be

supported. Furthermore, it implies that mechanisms based on critical layers and modal or non-modal growth processes alone (Hall & Smith 1988, 1991; Waleffe 1997; Schoppa & Hussain 2002) are not responsible for the energy transfer from U to \mathbf{u}' , as they ignore both the intrinsic time-dependence of the base flow or the non-normal aspect of the linear dynamics.

1.4. Cause-and-effect of linear mechanisms

The scenarios (i), (ii), and (iii), although consistent with the observed turbulence structure (Robinson 1991; Panton 2001; Jiménez 2018), are rooted in simplified theoretical arguments. It remains to establish whether self-sustaining turbulence follows predominantly one of the above mentioned mechanisms, or a combination of them. One major obstacle to assess linear theories arises from the lack of tools in turbulence research that resolve the cause-and-effect dilemma and unambiguously attributes a set of observed dynamics to well-defined causes. This brings to attention the issue of causal inference, which is a central theme in many scientific disciplines but is barely discussed in turbulence research with the exception of a handful of works (Tissot *et al.* 2014; Liang & Lozano-Durán 2017; Bae *et al.* 2018a; Lozano-Durán *et al.* 2019). It is via cause-and-effect relationships that we gain a sense of understanding of a given phenomenon, namely, that we are able to shape the course of events by deliberate actions or policies (Pearl 2009). It is for that reason that causal thinking is so pervasive. Typically, causality is inferred from *a posteriori* analysis of frozen flow snapshots or, at most, by time-correlation between pairs of signals extracted from the flow. However, elucidating causality, which inherently occurs over the course of time, is challenging using a frozen-analysis approach, and time-correlations lack the directionality and asymmetry required to guarantee causation (i.e., correlation does not imply causation) (Beebe *et al.* 2012). Recently, Lozano-Durán *et al.* (2019) introduced a probabilistic measure of causality to study self-sustaining wall turbulence based on the Shannon entropy that relies on a non-intrusive framework for causal inference. In the present work, we provide a complementary ‘intrusive’ viewpoint.

Here, we evaluate the contribution of different linear mechanisms via direct numerical simulation of channel flows with constrained energy extraction from the streamwise-averaged mean-flow. To that end, we modify the Navier–Stokes equations to suppress the causal link for a targeted linear mechanism, while maintaining a fully nonlinear system. This approach falls within the category of “instantiated” causality, i.e., intrusively perturbing a system (cause) and observing the consequences (effect) (Pearl 2009). In our case, altering the system has the benefit of providing a clear cause-and-effect assessment of the importance of each linear mechanism implicated in sustaining the flow. These ‘conceptual numerical experiments’ have been long practised in turbulence research and many notorious examples can be found in the literature (e.g., Jiménez 2018, 2020). However, the connection between conceptual numerical experiments and causality has been loose. In the present work, we aim to promote the formalisation and systematic use of cause-and-effect analysis to solve new and long-standing unsettled problems in Fluid Mechanics.

The study is organised as follows: § 2 contains the numerical details of the turbulent channel flow simulations. The statistics of interest for wall turbulence are reviewed in § 3. In § 4, we briefly outline the linear theories of self-sustaining wall turbulence and evaluate *a posteriori* their potential relevance for sustaining the flow. In § 5 we discuss the discovery of cause-and-effect relationships by interventions in the system. The actual relevance of different linear mechanisms from a cause-and-effect perspective is investigated in § 6. The section is further subdivided into four subsections devoted to

the cause-and-effect of exponential instabilities and transient growth with and without parametric instability. Finally, we conclude in § 7.

2. Minimal turbulent channel flows units

2.1. Numerical experiments

To investigate the role of different linear mechanisms, we perform direct numerical simulations of incompressible turbulent channel flows driven by a constant mean pressure gradient. Hereafter, the streamwise, wall-normal, and spanwise directions of the channel are denoted by x , y , and z , respectively, the corresponding flow velocity components by u , v , w , and pressure by p . The density of the fluid is ρ , the kinematic viscosity of the fluid is ν , and the channel height is h . The wall is located at $y = 0$, where no-slip boundary conditions apply, whereas free stress and no penetration conditions are imposed at $y = h$. The streamwise and spanwise directions are periodic.

The simulations are characterised by the friction Reynolds number, Re_τ , defined as the ratio of the channel height to the viscous length-scale $\delta_v = \nu/u_\tau$, where u_τ is the characteristic velocity based on the mean skin friction at the wall $u_\tau^2 \equiv \nu \langle \partial u(x, 0, z, t) / \partial y \rangle_{xzt}$. Here, the Reynolds number is $\text{Re}_\tau = h/\delta_v \approx 180$. The streamwise, wall-normal, and spanwise sizes of the computational domain are $L_x^+ \approx 337$, $L_y^+ \approx 186$, and $L_z^+ \approx 168$, respectively, where the superscript + denotes quantities scaled by ν and u_τ . Jiménez & Moin (1991) showed these ‘minimal channels’ contains an elementary turbulent flow unit comprised of a single streamwise streak and a pair of staggered quasi-streamwise vortices, that reproduce the dynamics of the flow in larger domains. Hence, the current numerical experiment isolates the few, most relevant, coherent structures involved in self-sustaining turbulence in the buffer layer. It also provides an ideal testbed for studying linear mechanisms, as it enables the identification of a meaningful base flow for these elementary coherent structures. In Appendix A, we assess the sensitivity of the key results presented in this study to changes in the domain extent (L_x and L_z). We find that our conclusions still hold when the size of computational domain is doubled in each direction.

We integrate the incompressible Navier–Stokes equations

$$\frac{\partial \mathbf{u}}{\partial t} = -\mathbf{u} \cdot \nabla \mathbf{u} - \frac{1}{\rho} \nabla p + \nu \nabla^2 \mathbf{u} + \mathbf{f}, \quad (2.1a)$$

$$\nabla \cdot \mathbf{u} = 0, \quad (2.1b)$$

with $\mathbf{u} \stackrel{\text{def}}{=} (u, v, w)$ and $\mathbf{f} = (u_\tau^2/h, 0, 0)$.

The simulations are performed with a staggered, second-order, finite differences scheme (Orlandi 2000) and a fractional-step method (Kim & Moin 1985) with a third-order Runge-Kutta time-advancing scheme (Wray 1990). The solution is advanced in time using a constant time step chosen appropriately so that the Courant–Friedrichs–Lewy condition is below 0.5. The code has been presented in previous studies on turbulent channel flows (Lozano-Durán & Bae 2016; Bae *et al.* 2018b, 2019). In addition, we performed various numerical experiments (summarised in the second column of table 2) in which we time-advance two sets of equations: one for the base flow \mathbf{U} and one for the fluctuations \mathbf{u}' . In this manner, we are able to independently control the dynamics of \mathbf{U} and \mathbf{u}' . We discuss in detail these additional experiments in §6.

The streamwise and spanwise grid resolutions are $\Delta x^+ \approx 6.5$ and $\Delta z^+ \approx 3.3$, respectively, and the minimum and maximum wall-normal resolutions are $\Delta y_{\min}^+ \approx 0.2$ and $\Delta y_{\max}^+ \approx 6.1$. The corresponding number of grid points in x , y , and z are $64 \times 90 \times 64$,

respectively. All the simulations presented here were run for at least $300h/u_\tau$ units of time after transients. This time-period is orders of magnitude longer than the typical lifetime of individual energy-containing eddies (Lozano-Durán & Jiménez 2014), and allows us to collect meaningful statistics of the self-sustaining cycle.

2.2. Base flow

We partition the flow into fluctuating velocities $\mathbf{u}' \stackrel{\text{def}}{=} (u', v', w')$ and base flow \mathbf{U} , defined as the time-varying mean streamwise velocity $\mathbf{U} \stackrel{\text{def}}{=} (U, 0, 0)$, where

$$U(y, z, t) \stackrel{\text{def}}{=} \langle u \rangle_x = \frac{1}{L_x} \int_0^{L_x} u(x, y, z, t) \, dx, \quad (2.2)$$

such that $u' \stackrel{\text{def}}{=} u - U$, $v' \stackrel{\text{def}}{=} v$, and $w' \stackrel{\text{def}}{=} w$. Hereafter, $\langle \cdot \rangle_{ijk\dots}$ denotes averaging over the directions (or time) $i, j, k\dots$, for example,

$$\langle u \rangle_{xzt} = \frac{1}{L_x L_z T_s} \int_0^{L_x} \int_0^{L_z} \int_0^{T_s} u(x, y, z, t) \, dt dz dx, \quad (2.3)$$

where T_s is a time-horizon long enough to remove any fluctuations. Figure 2 illustrates this flow decomposition and figure 3 depicts three typical snapshots of the base flow defined in (2.2). Note that because we are using a minimal box for the channel, only a single energy-containing eddy fits in the domain. Hence, U computed in minimal boxes is a meaningful base flow ‘‘felt’’ by individual flow structures. This would not be the case in larger domains in which the contribution of the multiple structures present in the flow cancels out and does not contribute to U .

We have not included in the base flow (2.2) the contributions from the streamwise averages of v and w components, $V \stackrel{\text{def}}{=} \langle v \rangle_x$ and $W \stackrel{\text{def}}{=} \langle w \rangle_x$, as these are not traditionally included in the study of stability of the streaky flow. Indeed, the vast majority of studies reported in table 1 do not account for V and W in the analysis. The results obtained using $(U, 0, 0)$ as base flow were repeated for a base flow consisting of (U, V, W) , and a concise overview of the findings can be found in Appendix B. In summary, the conclusions drawn for base flows $(U, 0, 0)$ or (U, V, W) are similar, and thus we focus on the former for simplicity.

The equation of motion for the base flow $\mathbf{U} = (U, 0, 0)$ is obtained by averaging the Navier–Stokes equations (2.1) in the streamwise direction,

$$\frac{\partial \mathbf{U}}{\partial t} + \mathbf{U} \cdot \nabla \mathbf{U} = -\mathcal{D}\langle \mathbf{u}' \cdot \nabla \mathbf{u}' \rangle_x - \frac{\mathcal{D}}{\rho} \nabla \langle p \rangle_x + \nu \nabla^2 \mathbf{U} + \mathbf{f}, \quad (2.4a)$$

$$\nabla \cdot \mathbf{U} = 0, \quad (2.4b)$$

where the operator \mathcal{D} sets the $y-$ and $z-$ components of the nonlinear terms and pressure to zero for consistency with $\mathbf{U} = (U, 0, 0)$ (see Appendix B). Subtracting (2.4) from (2.1) we get that the fluctuating flow \mathbf{u}' is governed by

$$\frac{\partial \mathbf{u}'}{\partial t} = \underbrace{\mathcal{L}(U)\mathbf{u}'}_{\text{linear processes}} + \underbrace{\mathbf{N}(\mathbf{u}')}_{\text{nonlinear processes}}, \quad (2.5)$$

where $\mathcal{L}(U)$ is the linearised Navier–Stokes operator for the fluctuating state vector about the instantaneous \mathbf{U} (see figure 2b) such that

$$\mathcal{L}(U)\mathbf{u}' = \mathcal{P} [-\mathbf{U} \cdot \nabla \mathbf{u}' - \mathbf{u}' \cdot \nabla \mathbf{U} + \nu \nabla^2 \mathbf{u}']. \quad (2.6)$$

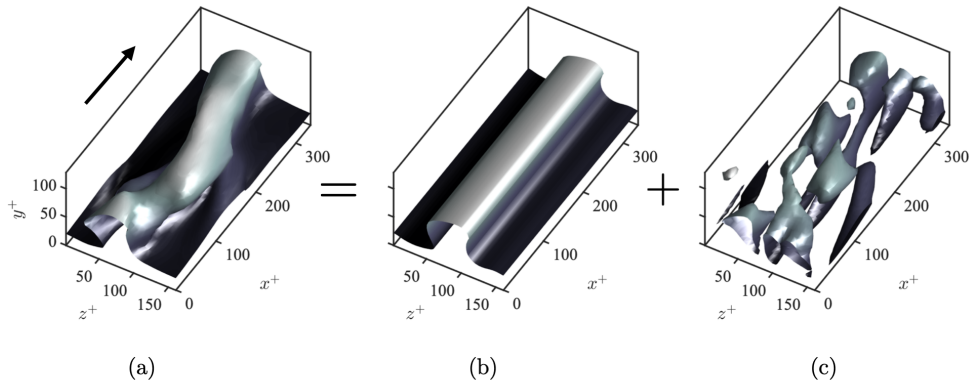


Figure 2: Decomposition of the instantaneous flow into a streamwise mean base flow and fluctuations. Instantaneous isosurface of streamwise velocity for (a) the total flow u , (b) the streak base flow U , and (c) the absolute value of the fluctuations $|u'|$. The values of the isosurfaces are 0.6 (a and b) and 0.1 (c) of the maximum streamwise velocity. Shading represents the distance to the wall from dark ($y = 0$) to light ($y = h$). The arrow in panel (a) indicates the mean flow direction. Results for case R180.

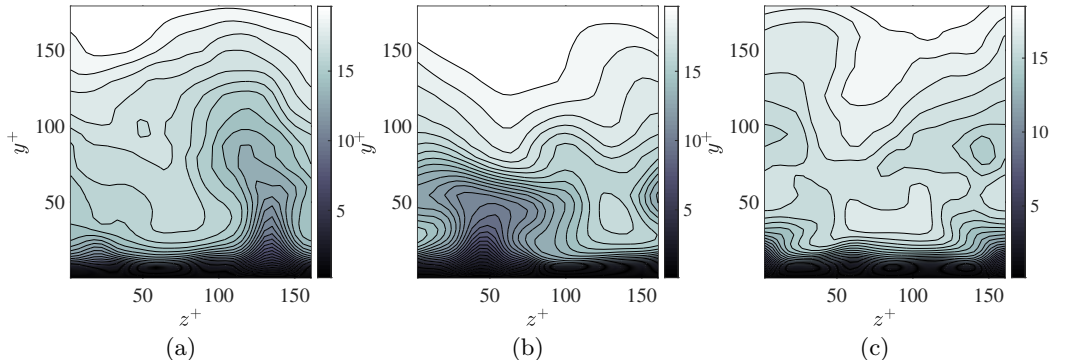


Figure 3: Examples of base flow, defined as $U(y, z, t) \stackrel{\text{def}}{=} \langle u \rangle_x$, for a turbulent channel flow at $\text{Re}_\tau \approx 180$ (case R180 from § 3). The examples are representative instances with (a,b) strong streak activity (c) and quiescent times.

The operator \mathcal{P} accounts for the kinematic divergence-free condition, $\nabla \cdot \mathbf{u}' = 0$. Conversely, $\mathbf{N}(\mathbf{u}')$ collectively denotes the nonlinear terms, which are quadratic with respect to fluctuating flow fields,

$$\mathbf{N}(\mathbf{u}') = \mathcal{P}[-\mathbf{u}' \cdot \nabla \mathbf{u}' + \mathcal{D}\langle \mathbf{u}' \cdot \nabla \mathbf{u}' \rangle_x]. \quad (2.7)$$

We are interested on the dynamics of \mathbf{u}' governed by (2.5). Note that the flow partition $\mathbf{U} + \mathbf{u}'$ implies that the energy injection into the velocity fluctuations is ascribed to

linear processes from $\mathcal{L}(U)$, since the term $\mathbf{N}(\mathbf{u}')$ is only responsible for redistributing the energy in space and scales among the fluctuations, i.e., the domain-integral of $\mathbf{u}' \cdot \mathbf{N}$ vanishes identically and thus

$$\frac{\partial}{\partial t} \langle E \rangle_{xyz} = \langle \mathbf{u}' \cdot \mathcal{L}(U) \mathbf{u}' \rangle_{xyz}, \quad (2.8)$$

where $E \stackrel{\text{def}}{=} \frac{1}{2} |\mathbf{u}'|^2$ is the fluctuating turbulent kinetic energy.

In the rest of the paper, in addition to solutions of the Navier-Stokes equations (2.1), we modify (2.6) to preclude the energy transfer from \mathbf{U} to \mathbf{u}' for targeted linear mechanisms. The simulations carried out are summarised in table 2, which includes the active linear mechanisms for energy transfer from \mathbf{U} to \mathbf{u}' and whether the cases are capable of sustaining turbulent fluctuations. The details on how the equations of motion are modified for each case are discussed in the remainder of the paper.

3. Regular wall turbulence

First, we solve the Navier-Stokes equations without any modification, so that all mechanisms for energy transfers from the base flow to the fluctuations are naturally allowed. We refer to this case as the “regular channel” (R180). We provide an overview of the self-sustaining state of the flow and one-point statistics for R180. The results are used as a reference solution in forthcoming sections. The governing equations for the regular channel flow are (2.4) and (2.5):

$$\frac{\partial \mathbf{u}'}{\partial t} = \mathcal{L}(U) \mathbf{u}' + \mathbf{N}(\mathbf{u}'), \quad (3.1a)$$

$$\frac{\partial \mathbf{U}}{\partial t} = -\mathbf{U} \cdot \nabla \mathbf{U} - \mathcal{D} \langle \mathbf{u}' \cdot \nabla \mathbf{u}' \rangle_x - \frac{\mathcal{D}}{\rho} \nabla \langle p \rangle_x + \nu \nabla^2 \mathbf{U} + \mathbf{f}, \quad \nabla \cdot \mathbf{U} = 0. \quad (3.1b)$$

The history of the domain-averaged turbulent kinetic energy, $\langle E \rangle_{xyz}$, is shown in figure 4(a). The evolution of $\langle E \rangle_{xyz}$ reveals the widely documented intermittent behaviour of the turbulent kinetic energy: relatively low turbulent kinetic energy states followed by occasional spikes usually ascribed to the regeneration and bursting stages of the self-sustaining cycle. As an example, figure 5 contains the streamwise velocity at three instants with different degrees of turbulence activity. If we interpret bursts events as moments of intense turbulent kinetic energy, the time-autocorrelation of $\langle E \rangle_{xyz}$ allows us to define a characteristic burst duration (T_b), and the period between two consecutive bursts (T_p). Figure 4(b) shows that $T_b \approx h/u_\tau$ measured as the time for zero correlation, while $T_p \approx 4h/u_\tau$ given by the time-distance between two consecutive maxima. Later on, we compare this burst period T_b with the characteristic time-scales for energy-injection into \mathbf{u}' .

A useful representation of the high-dimensional dynamics of the solution is obtained by projecting the instantaneous flow trajectory onto the two-dimensional space defined by the domain-averaged production and dissipation rates

$$\langle P \rangle_{xyz} \stackrel{\text{def}}{=} \left\langle -u'v' \frac{\partial U}{\partial y} - u'w' \frac{\partial U}{\partial z} \right\rangle_{xyz}, \quad (3.2)$$

$$\langle D \rangle_{xyz} \stackrel{\text{def}}{=} \langle -2\nu \mathcal{S} : \mathcal{S} \rangle_{xyz}, \quad (3.3)$$

where \mathcal{S} is the rate of strain tensor for the fluctuating velocities, and the colon denotes double inner product. The statistically stationary state of the system requires $\langle P \rangle_{xyzt} = -\langle D \rangle_{xyzt}$. The results, plotted in figure 6(a), show that the projected solution revolts

Case Sustained?	Equation for \mathbf{u}'	Equation for \mathbf{U}	Feedback from $\mathbf{u}' \rightarrow \mathbf{U}$	Active linear mechanisms for energy transfer from $\mathbf{U} \rightarrow \mathbf{u}'$
R180	(3.1a)	$U(y, z, t)$ from (3.1b)	✓	Exponential instabilities Transient growth Parametric instabilities
NF180	(6.2)	Precomputed $U(y, z, t)$ from R180	✗	Exponential instabilities Transient growth Parametric instabilities
NF-SEI180	(6.8)	Precomputed $U(y, z, t)$ from R180	✗	Transient growth Parametric instabilities
R-SEI180	(6.12a)	$U(y, z, t)$ from (6.12b)	✓	Transient growth Parametric instabilities
NF-TG180	(6.13)	Precomputed $U(y, z, t_0)$ from R180 at a frozen t_0	✗	Transient growth
NF-NLU180	(6.24), (6.30), (6.23c), (6.23d)	Precomputed $U(y, z, t)$ from R180	✗	Exponential instabilities Transient growth without lift-up Parametric instabilities
NF-NPO180	(6.25), (6.23b), (6.23c), (6.23d)	Precomputed $U(y, z, t)$ from R180	✗	Exponential instabilities Transient growth without push-over Parametric instabilities
NF-NO180	(6.23a), (6.30), (6.23c), (6.23d)	Precomputed $U(y, z, t)$ from R180	✗	Exponential instabilities Transient growth without Orr Parametric instabilities

Table 2: List of cases of turbulent channel flows with and without constrained linear mechanisms. The friction Reynolds number is $\text{Re}_\tau \approx 180$ for all cases. The cases are labelled following the nomenclature: R, regular wall turbulence with feedback $\mathbf{U} \rightarrow \mathbf{u}'$ allowed; NF, no-feedback from $\mathbf{U} \rightarrow \mathbf{u}'$ allowed; SEI, suppressed exponential instabilities; TG, only transient growth without exponential nor parametric instabilities; NLU, no linear lift-up of the streak; NPO, no linear push-over of the streak; NO, no linear Orr of the streak.

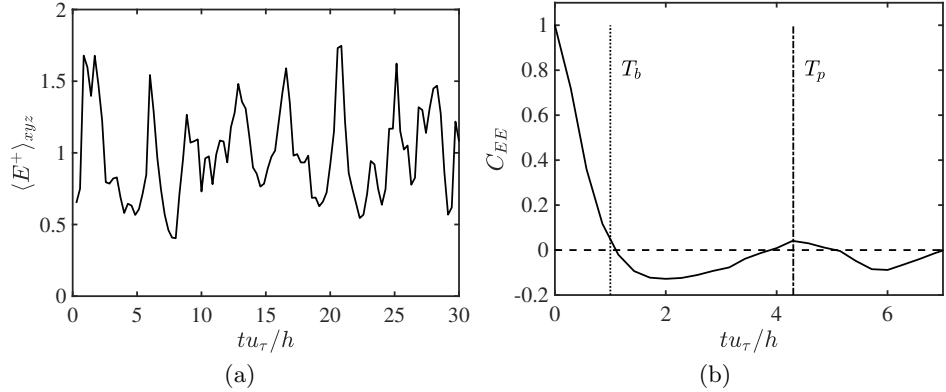


Figure 4: (a) The history of the domain-averaged turbulent kinetic energy of the fluctuations $\langle E \rangle_{xyz}$. Note that only $30h/u_\tau$ units of time are shown in the panel but the simulation was carried out for more than $300h/u_\tau$. (b) The time-autocorrelation of $\langle E \rangle_{xyz}$. The vertical dotted and dash-dotted lines are $t = h/u_\tau \approx T_b$ (burst duration) and $t = 4.3h/u_\tau \approx T_p$ (time between bursts), respectively. Results for regular channel flow R180.

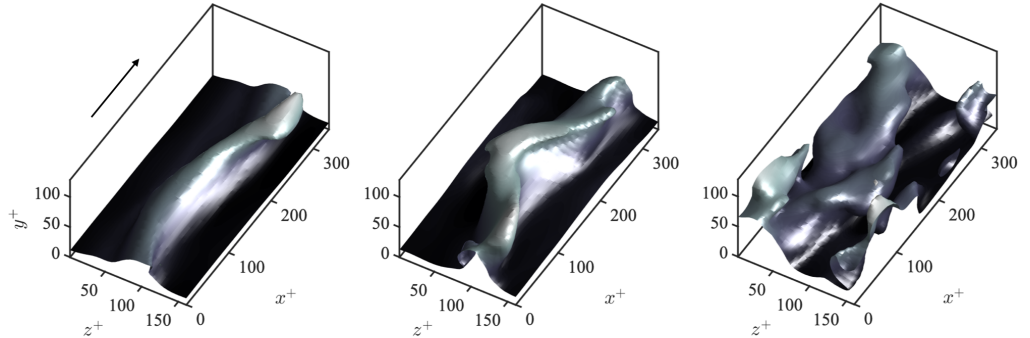


Figure 5: Instantaneous isosurface of the streamwise velocity u at different times for R180. The value of the isosurface is 0.65 of the maximum streamwise velocity. Shading represents the distance to the wall from dark ($y = 0$) to light ($y = h$). The arrow indicates the mean flow direction.

around $\langle P \rangle_{xyzt} = -\langle D \rangle_{xyzt}$ and is characterised by excursions into the high dissipation and high production regions, consistent with previous works (e.g. Jiménez *et al.* 2005; Kawahara *et al.* 2012).

The mean velocity profile and root-mean-squared (rms) fluctuating velocities for the regular channel are shown in figures 6(b–e). The results are compiled for the statistical steady state after initial transients. These have also been reported in the literature, with the worth noting difference that here the streamwise fluctuating velocity is defined as $u' = u - \langle u \rangle_x$, while in previous studies it is common to choose $u'' = u - \langle u \rangle_{xzt}$ instead. Figures 6(b–e) also contain the one-point statistics for a non-minimal channel flow with $L_x^+ \times L_z^+ = 2312 \times 1156$ ($L_x \times L_z \approx 12.5h \times 6.3h$) denoted by L180. The mean profile and cross-flow fluctuations in larger unconstrained domains are essentially captured in the

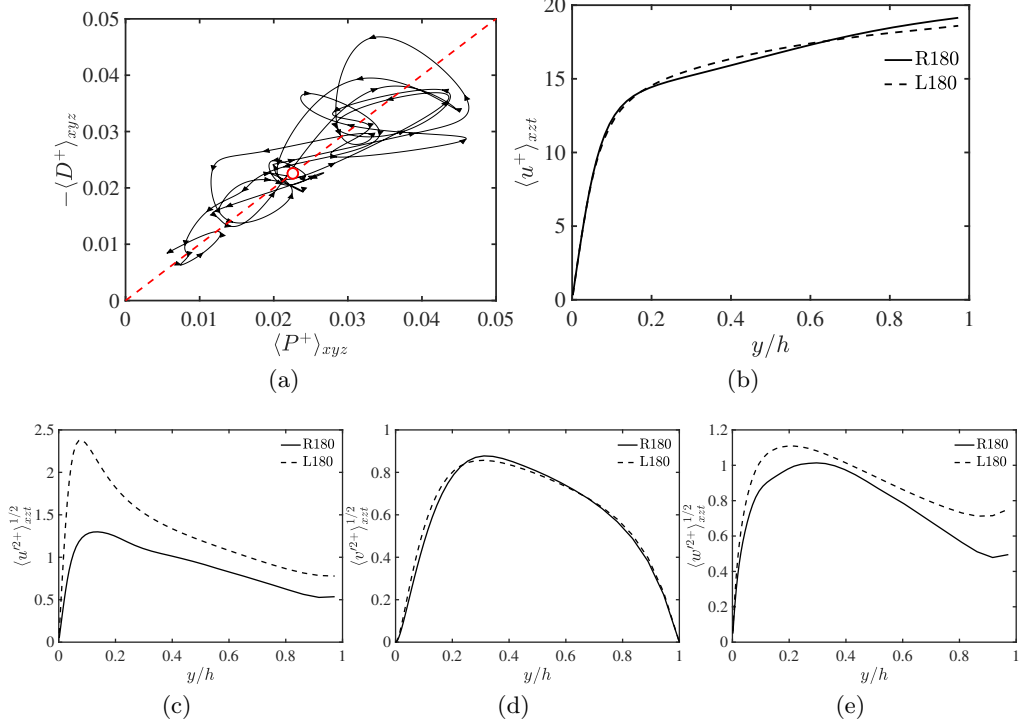


Figure 6: (a) Projection of the flow trajectory for R180 onto the average production rate $\langle P \rangle_{xyz}$ and dissipation rate $\langle D \rangle_{xyz}$ plane. The arrows indicate the time direction of the trajectory, which on average rotates counter-clockwise. The red dashed line is $\langle P \rangle_{xyz} = -\langle D \rangle_{xyz}$ and the red circle $\langle P \rangle_{xyzt} = -\langle D \rangle_{xyzt}$. The trajectory projected covers $15h/u_\tau$ units of time. (b) Streamwise mean velocity profile and (c) streamwise, (d) wall-normal, and (e) spanwise root-mean-squared fluctuating velocities as a function of the wall-normal distance for R180 (—) and equivalent non-minimal channel L180 (---) with $L_x^+ \times L_z^+ = 2312 \times 1156$ ($L_x \times L_z \approx 12.5h \times 6.3h$).

minimal box, while u' is underpredicted. The missing u' is due to larger-scale motions that do not participate in the buffer layer self-sustaining cycle (Jiménez & Moin 1991; Flores & Jiménez 2010). A large amount of u' is recovered when minimal channel domain is enlarged in the streamwise direction and Appendix A shows that our conclusions still hold when the minimal channel streamwise length is doubled.

4. Linear theories of self-sustaining wall turbulence: *a posteriori* analysis

The expected scenario of the full self-sustaining cycle in wall turbulence is the linear amplification of \mathbf{u}' induced by the operator $\mathcal{L}(U)$ followed by nonlinear saturation of \mathbf{u}' , scattering and generation of new disturbances by \mathbf{N} . We focus here is on the linear component of (2.5),

$$\frac{\partial \mathbf{u}'_{\text{linear}}}{\partial t} = \mathcal{L}(U)\mathbf{u}'_{\text{linear}}. \quad (4.1)$$

We revisit the linear mechanisms to transfer energy from the base flow to the fluctuating velocities, namely, modal exponential instability, non-modal transient growth, and non-modal transient growth assisted by parametric instability. The plausibility of each mechanism in $\mathcal{L}(U)$ as a contender to transfer energy from \mathbf{U} to \mathbf{u}' is investigated in a non-intrusive manner by interrogating the data from R180. This constitutes an *a posteriori* analysis and the actual relevance of the mechanisms for the flow physics is assessed in §6.

4.1. Energy transfer via exponential instability

The first mechanism considered is modal instability of the instantaneous base flow. At any given time, the exponential instabilities are obtained by eigen-decomposition of the matrix representation of the linear operator $\mathcal{L}(U)$ in (2.5),

$$\mathcal{L}(U) = \mathcal{Q}\Lambda\mathcal{Q}^{-1}, \quad (4.2)$$

where \mathcal{Q} consists of the eigenvectors organised in columns, \mathcal{Q}^{-1} is the inverse of \mathcal{Q} , and Λ is the diagonal matrix of associated eigenvalues, $\lambda_j + i\omega_j$, with $\lambda_j, \omega_j \in \mathbb{R}$. The solution of (4.1) is $\mathbf{u}'_{\text{linear}} \sim \mathbf{c} \exp[(\lambda_j + i\omega_j)t]$, with \mathbf{c} a constant. Hence, we say that the base flow is unstable if any of the growth rates λ_j is positive. More details on the stability analysis are provided in Appendix C along with the validation of our implementation in Appendix D. Figure 7 shows a representative example of the streamwise velocity for an unstable eigenmode. The predominant eigenmode has typically a sinuous structure of positive and negative patches of velocity flanking the velocity streak side by side, which may lead to its subsequent meandering and eventual breakdown. Varicose-type modes are also observed but they are less frequent.

Figure 8(a) shows the probability density functions of the growth rate of the four least stable eigenvalues of $\mathcal{L}(U)$. On average, the operator $\mathcal{L}(U)$ contains 2 to 3 unstable eigenmodes at any given instant. Denoting the Fourier streamwise wavenumber as k_x , the most unstable eigenmode usually corresponds to $k_x = 2\pi/L_x$, although occasionally modes with $k_x = 2\pi/(2L_x)$ become the most unstable. The sensitivity of our results to L_x is further discussed in Appendix A. The history of the maximum growth rate supported by $\mathcal{L}(U)$, denoted by $\lambda_1 = \lambda_{\max}$, is shown in figure 8(b). The flow is exponentially unstable ($\lambda_{\max} > 0$) more than 90% of the time. The average e-folding time for an exponentially unstable perturbation is roughly h/u_τ , which is comparable to the bursting duration T_b .

The ansatz underlying modal instability is that the spatial structure of the base flow remains constant in time. Therefore, we expect the above linear instability to manifest in the flow only when λ_{\max} is much larger than time rate of change of the base flow U , defined as

$$\lambda_U \stackrel{\text{def}}{=} \left\langle \frac{1}{2} \frac{|dE_U/dt|}{E_U} \right\rangle_{yz}, \quad (4.3)$$

where $E_U \stackrel{\text{def}}{=} \frac{1}{2}U^2$ is the energy of the base flow. The ratio λ_{\max}/λ_U for $\lambda_{\max} > 0$, shown in figure 8(c), is about 5 on average and occasionally achieves values above 20, i.e., the time-changes of U might be 5 to 20 times slower than e-folding time of the most unstable eigenmode. The growth of the modal instabilities is not overwhelmingly faster than the changes on the base flow. However, considering that the exponential growth of disturbances is supported for a non-negligible fraction of the flow history (roughly 90% of the time as shown before), modal instability of $\mathcal{L}(U)$ still stands as a potential mechanism sustaining the fluctuations. Note that the argument above does not imply that exponential instabilities are necessarily relevant for the flow when λ_{\max}/λ_U is large,

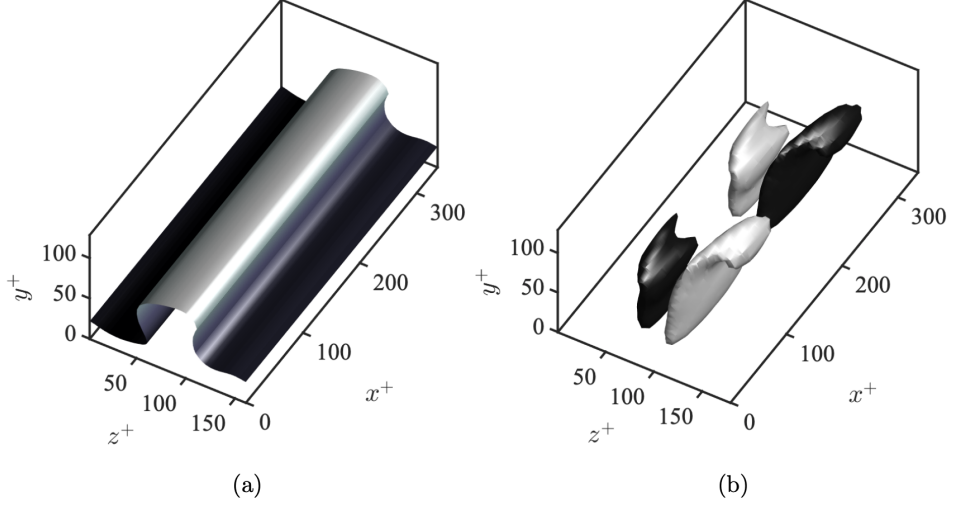


Figure 7: Representative exponential instability of the streak. (a) Instantaneous isosurface of the base flow U . The value of the isosurface is 0.6 of the maximum and the colour represents the distance to the wall. (b) Isosurface of the instantaneous streamwise velocity for the eigenmode associated with the most unstable eigenvalue $\lambda_{\max}h/u_\tau \approx 3$ at $t = 5.1h/u_\tau$. The flow structure of the eigenmode is consistent with a sinuous instability. The values of the isosurface are -0.5 (dark) and 0.5 (light) of the maximum streamwise velocity.

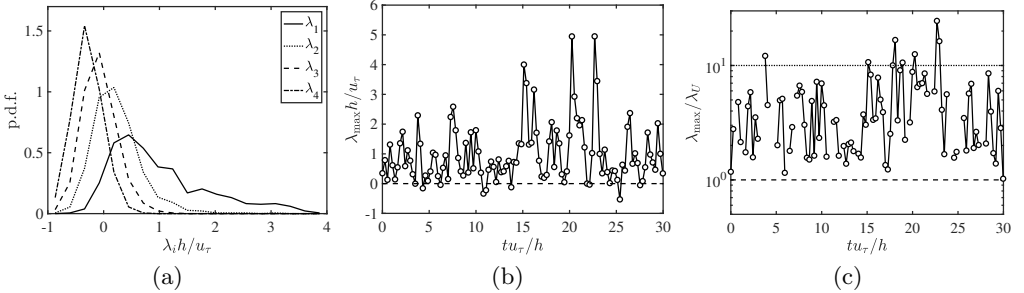


Figure 8: (a) Probability density functions of the growth rate of the four least stable eigenvalues of $\mathcal{L}(U)$, $\lambda_1 > \lambda_2 > \lambda_3 > \lambda_4$. (b) The time-series of the most unstable eigenvalue $\lambda_{\max} = \lambda_1$ of $\mathcal{L}(U)$. (c) The time-series of the ratio of λ_{\max}/λ_U , where λ_U is the growth rate of the base flow given by (4.3). The horizontal dashed and dotted lines are $\lambda_{\max}/\lambda_U = 1$ and $\lambda_{\max}/\lambda_U = 10$, respectively. Results for regular channel R180.

but only that they could manifest based on their characteristic time-scales. In fact, we show in §6.2 that exponential instabilities are not a requisite to sustain turbulence.

4.2. Energy transfer via transient growth

The second linear mechanism considered is the non-modal transient growth of the fluctuations. The linear dynamics of (4.1) can be formally written as:

$$\mathbf{u}'_{\text{linear}}(t + T) = \Phi_{t \rightarrow t+T} \mathbf{u}'_{\text{linear}}(t). \quad (4.4)$$

The propagator $\Phi_{t \rightarrow t+T}$ maps the fluctuating flow from time t to time $t+T$ and represents the cumulative effect of the linear operator $\mathcal{L}(U)$ during the period from t to $t+T$. If the base flow remains constant for $t \in [t_0, t_0 + T]$, then the propagator simplifies to

$$\Phi_{t_0 \rightarrow t_0+T} = \exp(\mathcal{L}_0 T), \quad (4.5)$$

where \mathcal{L}_0 denotes $\mathcal{L}(U(y, z, t_0))$.

Equation (4.4) accounts for both the modal and non-modal growth of \mathbf{u}' for $t \in [t_0, t_0 + T]$. The exponential growth of the fluctuating velocities was already quantified in § 4.1. Here we are concerned with the transient growth of \mathbf{u}' supported by \mathcal{L}_0 . To that end, we exclude from the analysis any growth of fluctuations due to the modal instabilities of \mathcal{L}_0 . This is achieved by the modified operator $\tilde{\mathcal{L}}_0$,

$$\tilde{\mathcal{L}}_0 \stackrel{\text{def}}{=} Q \tilde{\Lambda} Q^{-1}, \quad (4.6)$$

where $\tilde{\Lambda}$ is the stabilised counterpart of Λ in (4.2) obtained by setting the real part (λ_j) of all unstable eigenvalues of Λ equal to $-\lambda_j$, while their phase speed and eigenmode structure are left unchanged. A similar experiment was done by [Farrell & Ioannou \(2012\)](#) for Couette flow at low Reynolds numbers. We assessed that the transient growth properties of $\tilde{\mathcal{L}}_0$ are mostly insensitive to the amount of stabilisation introduced in Λ when $\lambda_j > 0$ are replaced by $-a\lambda_j$ with $a \in [1/10, 10]$. The potential effectiveness of transient growth due to a base flow $U(y, z, t_0)$ is then characterised by the energy gain G over some time-period T , defined as

$$G(t_0, T, \mathbf{u}'_0) \stackrel{\text{def}}{=} \frac{\langle \mathbf{u}'_T \cdot \mathbf{u}'_T \rangle_{xyz}}{\langle \mathbf{u}'_0 \cdot \mathbf{u}'_0 \rangle_{xyz}}, \quad (4.7)$$

where $\mathbf{u}'_T \stackrel{\text{def}}{=} \mathbf{u}'_{\text{linear}}(x, y, z, t_0 + T)$, $\mathbf{u}'_0 \stackrel{\text{def}}{=} \mathbf{u}'_{\text{linear}}(x, y, z, t_0)$ and T is the time-horizon for which the gain G is computed.

The energy, being a bilinear form, can be expressed as an inner product, e.g.,

$$(\mathbf{u}', \mathbf{u}') \stackrel{\text{def}}{=} \langle \mathbf{u}' \cdot \mathbf{u}' \rangle_{xyz}. \quad (4.8)$$

Using the definition (4.8) and the form of the propagator (4.5) for the frozen linear operator $\tilde{\mathcal{L}}_0$, the energy gain is rewritten as:

$$G(t_0, T, \mathbf{u}'_0) = \frac{(\mathbf{u}'_T, \mathbf{u}'_T)}{(\mathbf{u}'_0, \mathbf{u}'_0)} = \frac{(e^{\tilde{\mathcal{L}}_0 T} \mathbf{u}'_0, e^{\tilde{\mathcal{L}}_0 T} \mathbf{u}'_0)}{(\mathbf{u}'_0, \mathbf{u}'_0)} = \frac{(\mathbf{u}'_0, e^{\tilde{\mathcal{L}}_0^\dagger T} e^{\tilde{\mathcal{L}}_0 T} \mathbf{u}'_0)}{(\mathbf{u}'_0, \mathbf{u}'_0)}. \quad (4.9)$$

In the last equality, dagger \dagger denotes the adjoint operator. Note that, for $T \rightarrow \infty$, the growth rate (4.9) tends to 0, since the operator $\tilde{\mathcal{L}}_0$ is exponentially stable. The maximum gain over all initial conditions \mathbf{u}'_0 , denoted by $G_{\max}(t_0, T) = \sup_{\mathbf{u}'_0} G$, is given by the square of the largest singular value of the stabilised linear propagator $\tilde{\Phi}_0$ ([Butler & Farrell 1993; Farrell & Ioannou 1996](#)),

$$\tilde{\Phi}_{t_0 \rightarrow t_0+T} = \exp(\tilde{\mathcal{L}}_0 T) \quad (4.10)$$

$$= \mathcal{M} \Sigma \mathcal{N}^\dagger, \quad (4.11)$$

where Σ is a diagonal matrix, whose positive entries σ_j are the singular values of $\exp(\tilde{\mathcal{L}}_0 T)$ and the columns of \mathcal{M} and of \mathcal{N} are the output modes (or left-singular vectors) and input modes (or right-singular vectors) of $\exp(\tilde{\mathcal{L}}_0 T)$, respectively.

The maximum gain G_{\max} for R180 as a function of the optimisation time T is shown in figure 9(a). The values of G_{\max} also depend on t_0 ; figure 9(a) features the mean and

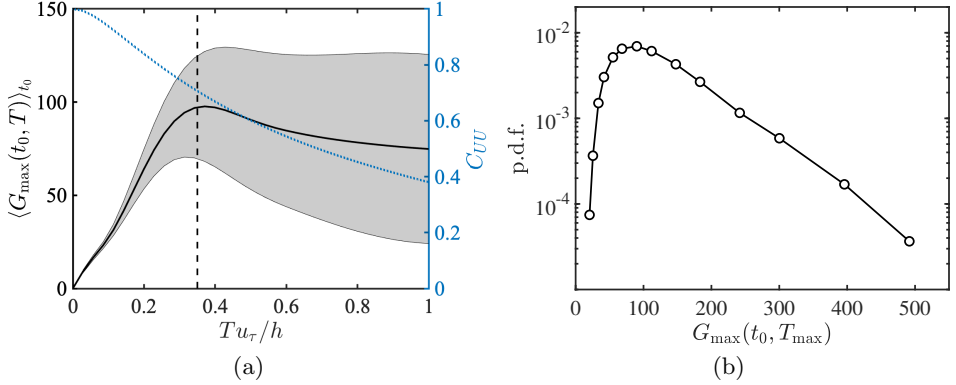


Figure 9: Energy transfer via transient growth with frozen-in-time base flow. (a) The ensemble average of the maximum energy gain $G_{\max}(t_0, T)$ (—, see Eq. (4.13)) over different initial instances t_0 , as a function of the time horizon T . Shaded regions denote \pm half standard deviation of $G_{\max}(t_0, T)$ for a given T . The vertical dashed line denotes $T_{\max} = 0.35h/u_\tau$. The blue dotted line is the auto-correlation of U , C_{UU} and its values appear on the right vertical axis. (b) Probability density function of gains $G_{\max}(t_0, T_{\max})$. Results for regular channel R180.

the standard deviation of G_{\max} for more than 1000 uncorrelated instants t_0 . Figure 9(a) reveals that non-normality alone is potentially able to produce fluctuation energy growth of the order of $G_{\max} \approx 100$. On average, the time-horizon for maximum gain is attained at $T_{\max} \approx 0.35h/u_\tau$. Thus, the maximum non-normal energy gain is obtained at a similar time-scale as the bursting time, T_p (see § 3). For an elapsed time of T_{\max} , the auto-correlation of the base flow,

$$C_{UU} \stackrel{\text{def}}{=} \left\langle [U(y, z, t) - \langle U \rangle_t] [U(y, z, t + T) - \langle U \rangle_t] \right\rangle_{yzt}, \quad (4.12)$$

has a value of 0.7, as shown in figure 9(a), which is reasonably high to justify the ‘frozen-base-flow’ assumption underlying the calculation of G . The p.d.f. of G_{\max} at T_{\max} (figure 9b) shows that $U(y, z, t_0)$ at certain times can support gains as high as 300.

The results here support the hypothesis of transient growth of the “frozen” mean streamwise flow $U(y, z, t_0)$ as a tenable candidate to sustain wall turbulence. It is worth noting that the maximum gain G_{\max} provided by the streak base flow $U(y, z, t_0)$ is considerably larger than the limited gains of around 10 reported in previous studies focused in the buffer layer (Del Álamo & Jiménez 2006; Pujals *et al.* 2009; Cossu *et al.* 2009). In these works, the base flow selected was $\langle u \rangle_{xzt}$, which lacks any spanwise z -structure and, hence supports much lower gains compared to $U(y, z, t_0)$.

Figure 10 provides an example of the input and output modes associated with the maximum optimal gain for one selected instant t_0 . The flow displays a sinuous backwards-leaning perturbation (input mode) that is being tilted forward by the mean shear over the time T (output mode). The process is reminiscent of the linear Orr/lift-up mechanism driven by continuity and wall-normal transport of momentum characteristic of the bursting process and streak formation (Orr 1907; Ellingsen & Palm 1975; Kim & Lim 2000; Jiménez 2013). Unlike the studies that used the base flow $\langle u \rangle_{xzt}$, our choice of a spanwise-varying base flow $U(y, z, t) = \langle u \rangle_x$ limits both the spanwise extent and

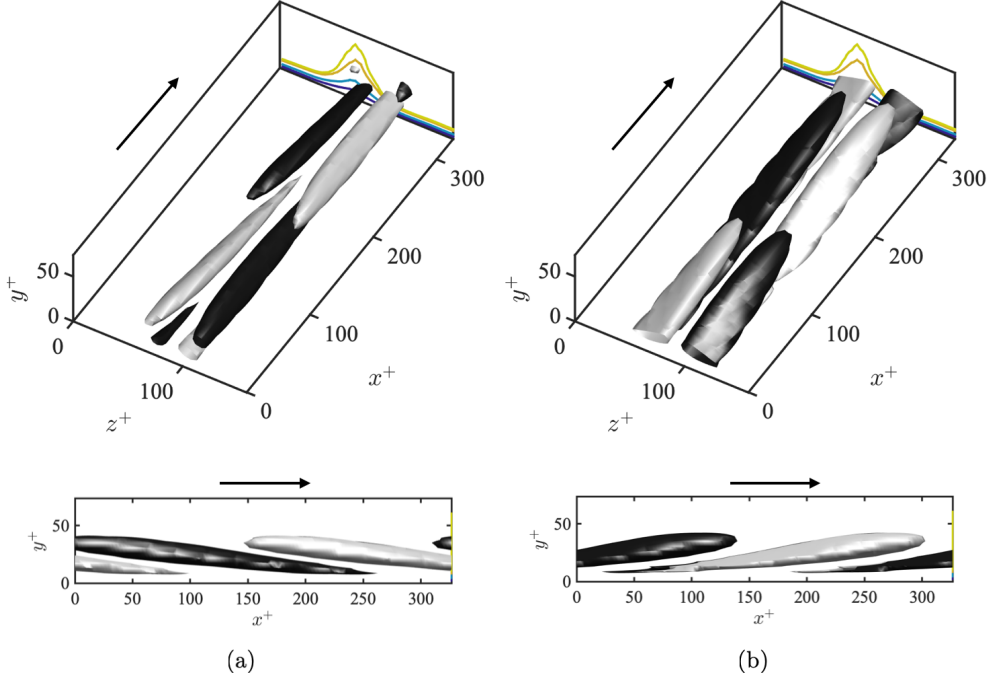


Figure 10: Representative sinuous input and output modes associated with transient growth of the streak. Isosurfaces of (a) the input and (b) the output wall-normal velocity mode associated with the largest singular value of $\tilde{\Phi}_{t_0 \rightarrow t_0+T}$ from (4.9) at $T = 0.35h/u_\tau$. The isosurfaces are -0.5 (dark) and 0.5 (light) of the maximum wall-normal velocity. The gain is $G_{\max} = 136$. The coloured lines at $x = L_x$ are $0.2, 0.4, 0.6$, and 0.7 of the maximum velocity of the base flow. The result is for the regular channel R180.

location of the input and output modes, which are controlled by the spanwise location of the streak.

4.3. Energy transfer via transient growth with time-varying base flow

In the previous section we have considered frozen-in-time base flows. We now relax this assumption such that the (stabilised) linear operator is time-dependent $\tilde{\mathcal{L}}(U(y, z, t))$. The propagator $\tilde{\Phi}_{t_0 \rightarrow t_0+T}^t$ (now with superscript t), is given by the Peano-Baker series (Rugh 1996),

$$\tilde{\Phi}_{t_0 \rightarrow t_0+T}^t = \mathcal{I} + \int_{t_0}^{t_0+T} \tilde{\mathcal{L}}(t_1) dt_1 + \int_{t_0}^{t_0+T} \tilde{\mathcal{L}}(t_1) \int_{t_0}^{t_1} \tilde{\mathcal{L}}(t_2) dt_2 dt_1 + \dots, \quad (4.13)$$

where \mathcal{I} is the identity matrix and we have simplified the notation to $\tilde{\mathcal{L}}(t) = \tilde{\mathcal{L}}(U(y, z, t))$. The propagator $\tilde{\Phi}_{t_0 \rightarrow t_0+T}^t$ represents the cumulative effect of $U(y, z, t)$ from t_0 to $t_0 + T$ accounting for time-variations in the base flow. The gain of (4.13) is denoted by

$$G^t(t_0, T, \mathbf{u}'_0) = \frac{\left(\mathbf{u}'_0, (\tilde{\Phi}_{t_0 \rightarrow t_0+T}^t)^\dagger (\tilde{\Phi}_{t_0 \rightarrow t_0+T}^t) \mathbf{u}'_0 \right)}{(\mathbf{u}'_0, \mathbf{u}'_0)}. \quad (4.14)$$

In contrast with the frozen-base-flow propagator $\tilde{\Phi}_{t_0 \rightarrow t_0+T}$ in (4.9), the time variations of the operator $\tilde{\mathcal{L}}(U)$ can either weaken or enhance the energy transfer from \mathbf{U} to \mathbf{u}' .

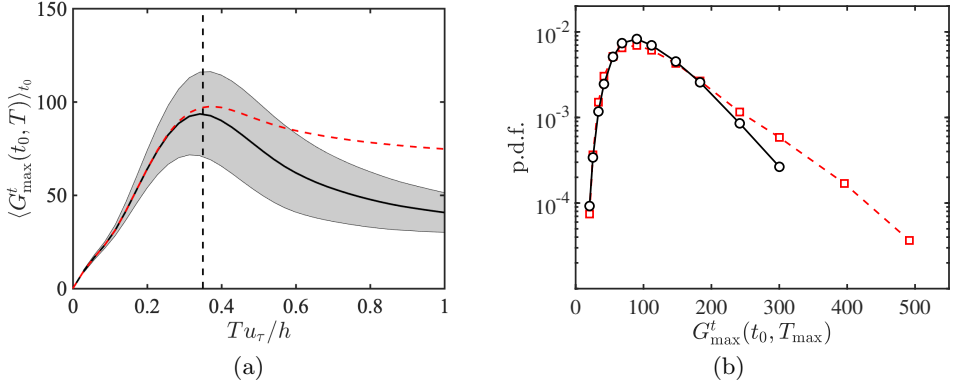


Figure 11: Energy transfer via transient growth with time-varying base flow. (a) The ensemble average of the maximum energy gain $G_{\max}^t(t_0, T)$ (—, see Eq. (4.13)) and $G_{\max}(t_0, T)$ (---, see Eq. (4.11)) over different initial instances t_0 , as a function of the time horizon T . Shaded regions denote \pm half standard deviation of $G_{\max}^t(t_0, T)$ for a given T . The vertical dashed line denotes $T_{\max} = 0.35h/u_\tau$. (b) Probability density function of gains for $G_{\max}^t(t_0, T_{\max})$ (—) and $G_{\max}(t_0, T_{\max})$ (---). Results for regular channel R180.

Another difference is that the G^t now admits a finite value at $T \rightarrow \infty$, despite that $\tilde{\mathcal{L}}(U)$ is modally stable at all instances. One potential route to enhance the gain for short times and/or achieve finite gains for long times is the parametric instability of the streak discussed in the introduction (Farrell & Ioannou 2012). However, it is shown below that none of these effects seem to be at play.

To evaluate the transient growth with time-varying base flows, we reconstruct the propagator without exponential instabilities $\tilde{\Phi}_{t_0 \rightarrow t_0+T}^t$ for case R180. In virtue of the property $\tilde{\Phi}_{t_0 \rightarrow t_0+T}^t = \tilde{\Phi}_{t_0 \rightarrow t_1}^t \tilde{\Phi}_{t_1 \rightarrow t_0+T}^t$ for $t_0 \leq t_1 \leq t_0+T$, the propagator is numerically computed by the ordered product of exponentials under the assumption of small Δt as

$$\tilde{\Phi}_{t_0 \rightarrow t_0+T}^t \approx \exp \left[\tilde{\mathcal{L}}(t_0 + n\Delta t) \Delta t \right] \cdots \exp \left[\tilde{\mathcal{L}}(t_0 + \Delta t) \Delta t \right] \exp \left[\tilde{\mathcal{L}}(t_0) \Delta t \right], \quad (4.15)$$

where $T = n\Delta t$, with n a positive integer. We saved the time-history of $U(y, z, t)$ from R180 at all time steps and used it to compute $\tilde{\Phi}_{t_0 \rightarrow t_0+T}^t$ via (4.15). We take $\Delta t^+ \approx 0.05$, which is the time step to integrate the equations of motion. The maximum gain supported by $\tilde{\Phi}_{t_0 \rightarrow t_0+T}^t$ is compared with its frozen-base-flow counterpart $\tilde{\Phi}_{t_0 \rightarrow t_0+T}$ in figure 11. The results reveal that energy growth with time-varying base flows is almost identical to the energy growth under the frozen-base-flow assumption up to $T \approx T_{\max} = 0.35h/u_\tau$, which also corresponds to the time for maximum gain for $\tilde{\Phi}_{t_0 \rightarrow t_0+T}^t$. For longer times $T > T_{\max}$, the gain with time-varying base flows is depleted with respect of the that of the frozen-base-flow, and tends to zero for $T \rightarrow \infty$ (not shown). The results show that accounting for time-variations of the base flow has a negligible effect for short times, but gains for frozen base-flows are over estimated for long times otherwise.

The propagator $\tilde{\Phi}_{t_0 \rightarrow t_0+T}^t$ can also be analysed in terms of input and output modes. The input and output modes for the time-varying base flow are again a backwards-leaning perturbation (input mode) that is being tilted forward by the mean shear (output mode), very similar to the example shown in figure 10, but not shown here for brevity.

5. Cause-and-effect discovery with interventions

The analysis above was performed *a posteriori* by interrogating the data from R180 in a non-intrusive manner. This provides a valuable insight about the energy injection into the fluctuations but hinders our ability to faithfully assess cause-and-effect links between linear mechanisms and their actual impact on the fully nonlinear system.

The most intuitive definition of causality relies on *interventions*: manipulation of the causing variable leads to changes in the effect (Eichler 2013; Pearl 2009). More precisely, to describe the causal effect that a process A (e.g., exponential growth of instability) exerts on another process B (e.g., growth of turbulent kinetic energy), we consider the intervention in the governing equations of the system that sets A to a modified value A_i and observe the post-intervention consequences. How to identify the intervention A_i that best unveils the causality from A to B is not trivial and relies on our knowledge of the system and shrewdness to modify it (Eberhardt & Scheines 2007; Hyttinen *et al.* 2013). When we do not have any prior knowledge of how A might affect B , we need to resort to randomised interventions for discovering causal relationships (Fisher 1936).

As turbulence is a high-dimensional chaotic system, we are concerned with the statistical alterations in the system after the intervention rather than changes in individual events. The probability distribution of the process B for the non-intervened system is measured by $\mathbb{P}(B)$. The causal effect of A on B can be quantified by any functional of the post-intervention distribution $\mathbb{P}(B|A = A_i)$, where $\mathbb{P}(\cdot|A = A_i)$ is the probability of the intervened system. The most commonly used measure of the statistical effect of A on B is the mean causal effect defined as the average increase or decrease in value caused by the intervention.

In the next section, we follow this approach to assess the relevance of different linear mechanisms on the energy transfer from the base flow \mathbf{U} to the fluctuations \mathbf{u}' . The starting point is the R180 system (3.1), which is sensibly modified to suppress a targeted linear mechanism.

6. Linear theories of self-sustaining wall turbulence: cause-and-effect analysis

6.1. Wall turbulence without explicit feedback from \mathbf{u}' to \mathbf{U}

In previous sections, we have acted as if

$$\frac{\partial \mathbf{u}'}{\partial t} = \mathcal{L}(U)\mathbf{u}' + \mathbf{N}(\mathbf{u}'), \quad (6.1)$$

is linear in the term $\mathcal{L}(U)\mathbf{u}'$. This is obviously not true because $U(y, z, t)$ depends on \mathbf{u}' via the nonlinear feedback term $-\langle \mathbf{u}' \cdot \nabla \mathbf{u}' \rangle_x$ (see the base-flow evolution equation (3.1b)).

Prior to investigating the cause-and-effect links of linear mechanisms in $\mathcal{L}(U)$, we derive a surrogate system in which the energy injection is strictly linear by preventing the explicit feedback from \mathbf{u}' to \mathbf{U} . To achieve this, we proceed as follows:

- (i) We perform a simulation of R180 for $600h/u_\tau$ units of time (after transients) with a constant time step.
- (ii) We store the base flow at all time steps. We denote the time-series of this base flow as $U_0 = U(y, z, t)$ from case R180.
- (iii) We time-integrate the system

$$\frac{\partial \mathbf{u}'}{\partial t} = \mathcal{L}(U_0)\mathbf{u}' + \mathbf{N}(\mathbf{u}'), \quad (6.2)$$

$$U_0 = U(y, z, t) \text{ from case R180.} \quad (6.3)$$

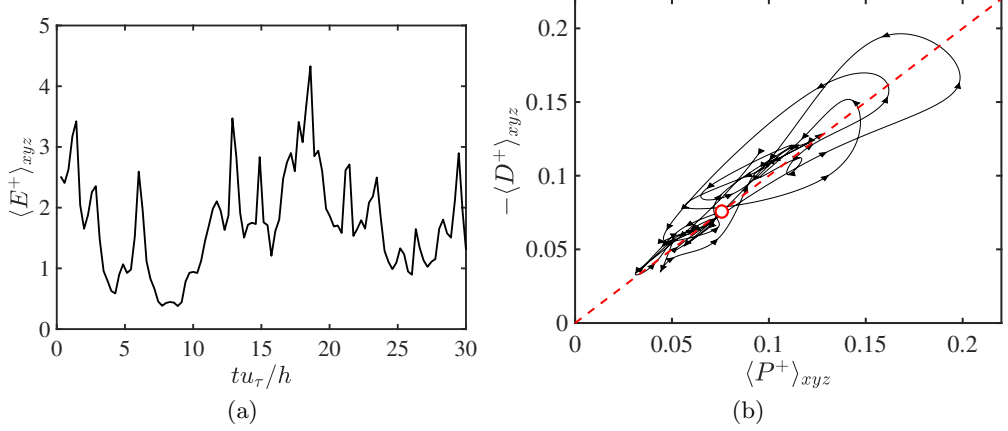


Figure 12: (a) The history of the domain-averaged turbulent kinetic energy of the fluctuations $\langle E \rangle_{xyz}$. Note that only $30h/u_\tau$ units of time are shown in the panel but the simulation was carried out for $600h/u_\tau$. (b) Projection of the flow trajectory onto the average production rate $\langle P \rangle_{xyz}$ and dissipation rate $\langle D \rangle_{xyz}$ plane. The arrows indicate the time direction of the trajectory, which on average rotates counter-clockwise. The red dashed line is $\langle P \rangle_{xyz} = -\langle D \rangle_{xyz}$ and the red circle $\langle P \rangle_{xyzt} = -\langle D \rangle_{xyzt}$. The trajectory projected covers $15h/u_\tau$ units of time. The results are for NF180.

Equation (6.2) is initialised from a random, incompressible velocity field and it is integrated for $600h/u_\tau$ units of time using the same time step as in R180. Equation (6.2) is akin to the Navier–Stokes equations, in which the equation of motion of \mathbf{U} is replaced by $\mathbf{U} = (U_0, 0, 0)$. We refer to this case as “channel flow with no-feedback” or NF180 for short. Note that the base flow U_0 has no *explicit* feedback from \mathbf{u}' in (6.2), although it has been *implicitly* ‘shaped’ by the velocity fluctuations of R180 and, as such, it contains dynamic information of actual wall turbulence. The key difference in (6.2) is that the term $\mathcal{L}(U_0)\mathbf{u}'$ is now strictly linear while preserving the modal and non-modal properties of $\mathcal{L}(\mathbf{U})$ in R180.

The flow sustained in NF180 is turbulent as revealed by the history of the turbulent kinetic energy in figure 12(a). Moreover, the footprint of the flow trajectory projected onto the $\langle P \rangle_{xyz}$ – $\langle D \rangle_{xyz}$ plane in figure 12(b) also exhibits a similar behaviour to R180: the flow is organised around $\langle P \rangle_{xyz} = -\langle D \rangle_{xyz}$ with excursions into the high/low dissipation and production regions with predominantly counter-clockwise motions. This assessment is merely qualitative and some differences are expected between the $\langle P \rangle_{xyz}$ – $\langle D \rangle_{xyz}$ trajectories in R180 and NF180.

The mean turbulence intensities for NF180 are shown in figure 13. Statistics are collected once the system reaches the statistically steady state. The mean velocity profile is omitted as it is identical to that of R180 in figure 6(b). For comparison, figure 13 includes one-point statistics for R180 (previously shown in figure 6(c,d,e)). The main consequence of precluding the non-linear feedback from \mathbf{u}' to \mathbf{U} is an increase of the level of the turbulence intensities, i.e., the feedback mechanism counteracts the growth of fluctuating velocities in R180. Despite these differences, we can still argue that the turbulence intensities in NF180 are alike those in R180 by noting that the friction velocity u_τ is no longer the appropriate scaling velocity for NF180. The traditional argument for u_τ as the relevant velocity-scale for the energy-containing eddies is that the turbulence

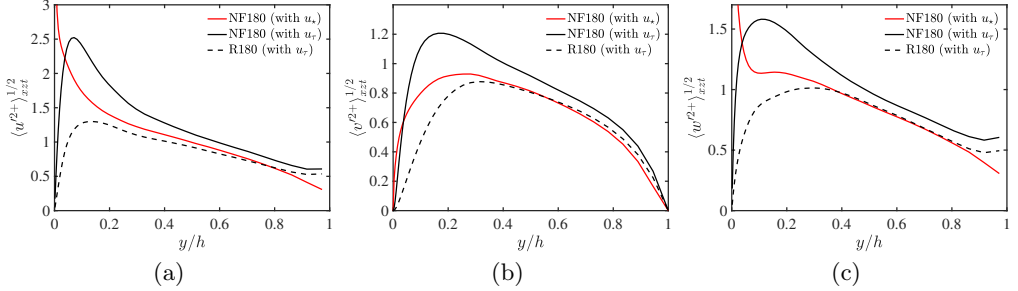


Figure 13: (a) Streamwise, (b) wall-normal, and (c) spanwise mean root-mean-squared fluctuating velocities as a function of the wall-normal distance for case R180 normalised by u_τ (---), case NF180 normalised by u_τ (—), and NF180 normalised by u_* (—).

intensities equilibrate to comply with the mean integrated momentum balance,

$$-\langle uv \rangle \approx u_\tau^2(1 - y/h), \quad (6.4)$$

after viscous effects are neglected (Townsend 1976; Tuerke & Jiménez 2013). As a result, $u_\tau \approx \sqrt{-\langle uv \rangle / (1 - y/h)}$ stands as the characteristic velocity for all wall-normal distances. However, we have altered the momentum equation for case NF180, which renders the balance in (6.4) invalid. A more general argument was made by Lozano-Durán & Bae (2019) by which the characteristic velocity of the energy-containing eddies, u_* , is controlled by the characteristic production rate of turbulent kinetic energy, $P_* \sim u_*^2/t_*$, where t_* is the time-scale to extract energy from the mean shear

$$t_* \sim \frac{1}{\sqrt{(\partial U / \partial y)^2 + (\partial U / \partial z)^2}}. \quad (6.5)$$

Taking as characteristic production rate

$$P_* \sim \sqrt{\left(u'v' \frac{\partial U}{\partial y}\right)^2 + \left(u'w' \frac{\partial U}{\partial z}\right)^2}, \quad (6.6)$$

a characteristic velocity-scale is constructed as

$$u_*(y) \stackrel{\text{def}}{=} \sqrt{\frac{\langle P_* t_* \rangle_{xzt}}{1 - y/h}}, \quad (6.7)$$

which generalises the concept of friction velocity. The factor $1/\sqrt{1 - y/h}$ is introduced for convenience in analogy with u_τ in (6.4) so that u_* reduces to u_τ for the regular wall turbulence.

Figure 13 shows that the turbulence intensities, when scaled with u_* , resemble those of R180, at least for $y > 0.1h$ where viscous effects are negligible. This suggests that the underlying flow dynamics of NF180 is of similar nature as the regular channel case R180 under the proper scaling. Thus, hereafter we utilise NF180 as reference case for comparisons as we have shown that it exhibits similar dynamics to regular wall turbulence while being truly linear in $\tilde{\mathcal{L}}(U)\mathbf{u}'$. Occasionally, we allow back the feedback $\mathbf{u}' \rightarrow \mathbf{U}$.

6.2. Wall turbulence without exponential instability of the streaks

We modify the operator $\mathcal{L}(U_0)$ so that all the unstable eigenmodes are rendered stable at all times. We refer to this case as the “non-feedback channel with suppressed exponential instabilities” (NF-SEI180) and we inquire whether turbulence is sustained under those conditions. The approach is implemented by replacing $\mathcal{L}(U_0)$ at each time-instance by its exponentially-stable counterpart $\tilde{\mathcal{L}}(U_0)$, introduced in (4.6). The governing equations for the channel with suppressed exponential instabilities are

$$\frac{\partial \mathbf{u}'}{\partial t} = \tilde{\mathcal{L}}(U_0)\mathbf{u}' + \mathbf{N}(\mathbf{u}'), \quad (6.8)$$

$$U_0 = U(y, z, t) \text{ from case R180.} \quad (6.9)$$

The stable counterpart of $\mathcal{L}(U_0)$ given by $\tilde{\mathcal{L}}(U_0)$ guarantees an exponentially stable wall turbulence with respect to the base flow at all times, while leaving other linear mechanisms almost intact. Note that the analysis §4.1 was performed *a posteriori* using data from R180, while in the present case the nonlinear dynamical system (6.8) is actually integrated in time. The simulation was initialised using a flow field from R180, from which the unstable and neutral modes are projected out, and integrated in time for $300h/u_\tau$ after transients. It was assessed that initialising the equation with a random velocity field yields exactly the same conclusions.

It is useful to note that the stabilisation of $\mathcal{L}(U_0)$ in (6.8) can be interpreted as the addition of a forcing term to the right-hand size of (6.8) by considering the approximation to $\tilde{\mathcal{L}}(U_0)$

$$\hat{\mathcal{L}}(U_0) = \mathcal{L}(U_0) - \sum_{j=1}^n 2\lambda_j \mathbf{U}_j \mathbf{U}_j^\dagger \approx \tilde{\mathcal{L}}(U_0), \quad (6.10)$$

where \mathbf{U}_j is the eigenmode of $\mathcal{L}(U_0)$ associated with eigenvalue $\lambda_j > 0$, and n is the total number of unstable eigenvalues. The factor 2 on the right-hand size of (6.10) transforms $\lambda_j > 0$ for $\mathcal{L}(U_0)$ into $-\lambda_j$ for $\hat{\mathcal{L}}(U_0)$ in analogy with the stabilised operator $\tilde{\mathcal{L}}$; see (4.6). Equation (6.10) is approximate, as $\mathcal{L}(U_0)$ is highly non-normal. However, we confirmed that the largest eigenvalues and eigenmodes of $\hat{\mathcal{L}}(U_0)$ and $\tilde{\mathcal{L}}(U_0)$ are almost identical most of the time (Appendix E). In virtue of (6.10), the modification of $\mathcal{L}(U_0)$ in (6.10) is easily interpretable: **stabilising $\mathcal{L}(U_0)$ is equivalent to introducing a linear drag term, $-\mathcal{F}\mathbf{u}'$, in which the drag coefficient depends on the base flow $U(y, z, t)$** , i.e.,

$$\mathcal{F}(U) = \sum_{j=1}^n 2\lambda_j \mathbf{U}_j \mathbf{U}_j^\dagger, \quad (6.11)$$

that counteracts the growth of the unstable modes at a rate proportional of the growth rate of the mode itself.

The results of integrating (6.8) are presented in figures 14 and 15. The p.d.f.s of λ_j and a segment of the time-series of the maximum modal growth rate of $\tilde{\mathcal{L}}(U_0)$ are shown in figure 14, which confirms that the system is successfully stabilised.

Figure 15(a) shows the history of the turbulent kinetic energy for NF-SEI180 after initial transients. The result verifies that turbulence persists when $\mathcal{L}(U_0)$ is replaced by $\tilde{\mathcal{L}}(U_0)$. The patterns of the flow trajectories projected onto the production–dissipation plane (figure 15b) exhibits features similar to those discussed above for R180 and NF180.

The turbulence intensities for NF-SEI180 are presented in figure 16 and compared with those for NF180. The mean profile is the same as R180 (not shown). Notably, the channel flow without exponential instabilities is capable of sustaining turbulence. The

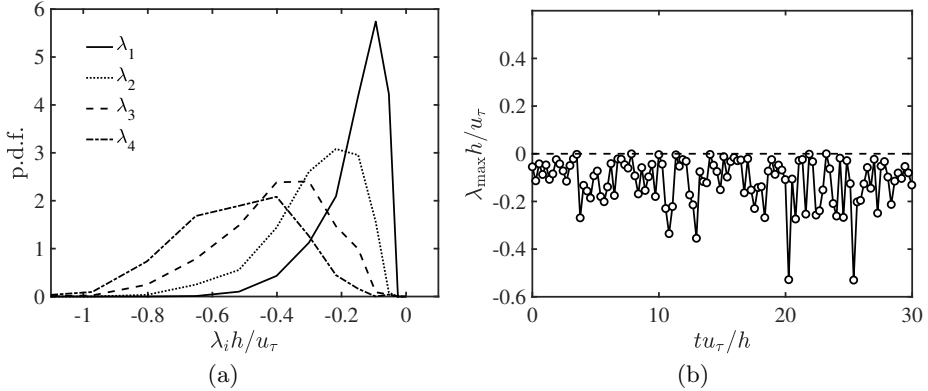


Figure 14: (a) Probability density functions of the growth rate of the four least stable eigenvalues of $\tilde{\mathcal{L}}(U_0)$, $\lambda_1 > \lambda_2 > \lambda_3 > \lambda_4$. (b) The history of the most unstable eigenvalue λ_{\max} of $\tilde{\mathcal{L}}(U_0)$. Results are for the channel with suppressed modal instabilities NF-SEI180.

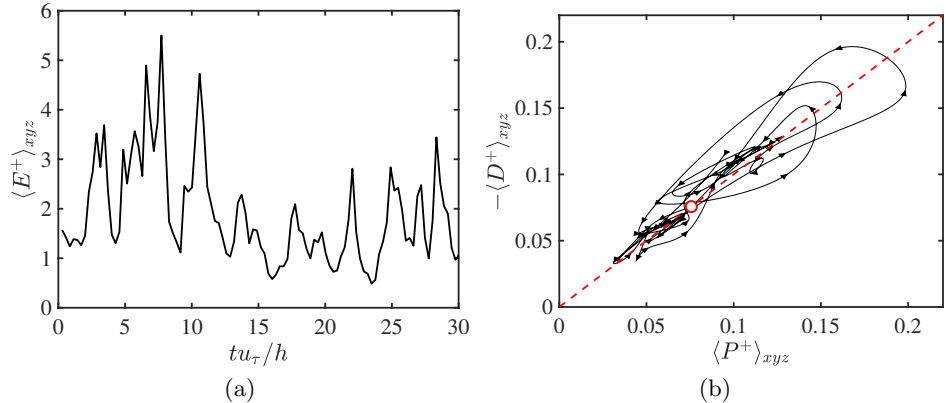


Figure 15: (a) The history of the domain-averaged turbulent kinetic energy of the fluctuations $\langle E \rangle_{xyz}$. Note that only $30h/u_\tau$ units of time are shown in the panel but the simulation was carried out for more than $300h/u_\tau$. (b) Projection of the flow trajectory onto the average production rate $\langle P \rangle_{xyz}$ and dissipation rate $\langle D \rangle_{xyz}$ plane. The arrows indicate the time direction of the trajectory, which on average rotates counter-clockwise. The red dashed line is $\langle P \rangle_{xyz} = -\langle D \rangle_{xyz}$ and the red circle $\langle P \rangle_{xyzt} = -\langle D \rangle_{xyzt}$. The trajectory projected covers $15h/u_\tau$ units of time. Results are for the channel with suppressed modal instabilities NF-SEI180.

new flow equilibrates at a state with fluctuations depleted by roughly 10%–20%. The outcome demonstrates that, even if the linear instabilities of the streak manifest in the flow, they are not required for maintaining wall turbulence.

It is worth emphasising that, according to the post-processing analysis in §4, modal instabilities stand as a viable mechanism to explain the energy transfer from \mathbf{U} to \mathbf{u}' . Yet, we have demonstrated here that turbulence remains almost unchanged in their absence. This illustrates very vividly the risks of evaluating linear (and other) theories *a posteriori* without accounting for the cause-and-effect relations in the actual flow.

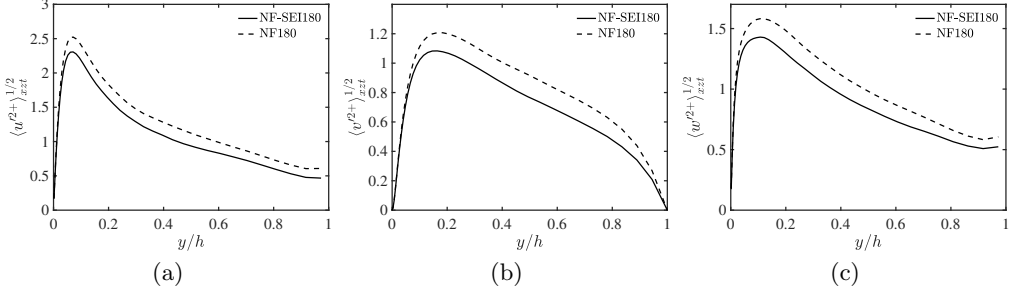


Figure 16: (a) Streamwise, (b) wall-normal, and (c) spanwise root-mean-squared fluctuating velocities as a function of the wall-normal distance for the non-feedback channel NF180 (---) and the non-feedback channel with suppressed exponential instabilities NF-SEI180 (—).

6.2.1. Case with explicit feedback from \mathbf{u}' to \mathbf{U} allowed

It was shown above that turbulence is sustained despite the absence of exponential instabilities. This was demonstrated for NF-SEI180, in which the nonlinear feedback from \mathbf{u}' to \mathbf{U} was excluded. We have seen in §6.1 that inhibiting the feedback from \mathbf{u}' to \mathbf{U} actually enhances the turbulence intensities with respect to u_τ . This may cast doubts on whether the ‘weaker’ fluctuations from R180 can be sustained when modal instabilities are also cancelled out. To clarify this point, we resolve a channel with suppressed exponential instabilities in which the feedback from \mathbf{u}' to \mathbf{U} is allowed. The equations of motion in this case are:

$$\frac{\partial \mathbf{u}'}{\partial t} = \tilde{\mathcal{L}}(\mathbf{U})\mathbf{u}' + \mathbf{N}(\mathbf{u}'), \quad (6.12a)$$

$$\frac{\partial \mathbf{U}}{\partial t} = -\mathbf{U} \cdot \nabla \mathbf{U} - \mathcal{D}\langle \mathbf{u}' \cdot \nabla \mathbf{u}' \rangle_x - \frac{\mathcal{D}}{\rho} \nabla \langle p \rangle_x + \nu \nabla^2 \mathbf{U} + \mathbf{f}, \quad \nabla \cdot \mathbf{U} = 0. \quad (6.12b)$$

We refer to this case as “regular channel with suppressed exponential instabilities” or R-SEI180. Note that the only difference of (6.12) from the original Navier–Stokes equations (2.1) is the modally stable $\tilde{\mathcal{L}}(\mathbf{U})$ instead of $\mathcal{L}(\mathbf{U})$. The base flow \mathbf{U} is now dynamically coupled to \mathbf{u}' via the nonlinear term $-\mathcal{D}\langle \mathbf{u}' \cdot \nabla \mathbf{u}' \rangle_x$ in (6.12b). We initialise simulations of (6.12) from a flow field of R180 after projecting out the unstable and neutral modes. It was checked that using random velocities as initial condition yields the same results.

The history of λ_{\max} for $\tilde{\mathcal{L}}(\mathbf{U})$, shown in figure 17(a), confirms that modal instabilities are successfully removed. Figure 17(b) contains the evolution of the turbulent kinetic energy and shows that turbulence persists under the stabilised linear dynamics of (6.12a). The flow trajectories projected onto the production–dissipation plane (figure 17c) also exhibit similar features to those discussed above for R180 and NF-SEI180.

The mean velocity profiles and turbulence intensities for R-SEI180 and R180 are shown in figure 18. The results are consistent with the trends reported in figure 16 for NF-SEI180 and NF180 simulations: turbulence without modal instabilities is sustained despite allowing the feedback from \mathbf{u}' to \mathbf{U} . As in NF-SEI180, the resulting velocity fluctuations are diminished by roughly 10%. Figure 19 portrays snapshots of the streamwise velocity at three different instants for the R-SEI180 simulation. As in R180 (cf. figure 5), the spatial organisation of the streak cycles through different stages of elongated straight motion, meandering and breakdown, although the first two states (panels (a) and (b))

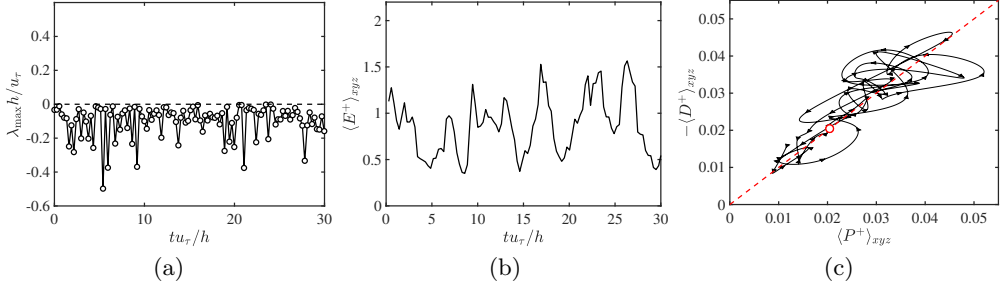


Figure 17: (a) The history of the most unstable eigenvalue λ_{\max} of $\tilde{\mathcal{L}}(U)$. Results for channel with suppressed modal instabilities and feedback from \mathbf{u}' to \mathbf{U} allowed (R-SEI180). (b) The history of the turbulent kinetic energy of the fluctuation energy $E = \frac{1}{2}\mathbf{u}' \cdot \mathbf{u}'$ averaged over the channel domain. Note that only $30h/u_\tau$ units of time are shown in the panels (a) and (b) but the simulation was carried out for more than $300h/u_\tau$. (c) Projection of the flow trajectory onto the average production rate $\langle P \rangle_{xyz}$ and dissipation rate $\langle D \rangle_{xyz}$ plane. The arrows indicate the time direction of the trajectory, which on average rotates counter-clockwise. The red dashed line is $\langle P \rangle_{xyz} = -\langle D \rangle_{xyz}$ and the red circle $\langle P \rangle_{xyzt} = -\langle D \rangle_{xyzt}$. The trajectory projected covers $15h/u_\tau$ units of time. Results for channel with suppressed modal instabilities but with feedback from \mathbf{u}' to \mathbf{U} allowed (R-SEI180).

occur more frequently than in R180. Indeed, if we consider the common definition for the streamwise velocity fluctuation $u'' = u - \langle u \rangle_{xzt}$, which contains part of the streaky flow, the new flow in R-SEI180 attains an augmented streak intensity as clearly depicted in figure 18(b). The outcome is consistent with the occasional inhibition of the streak meandering or breakdown via exponential instability, which enhances u'' , whereas wall-normal ($v'' = v'$) and spanwise ($w'' = w'$) turbulence intensities are diminished due to a lack of vortices succeeding the collapse of the streak (namely, mechanism (i) discussed in the introduction). This behaviour was also observed in many drag reduction investigations (Jung *et al.* 1992; Laadhari *et al.* 1994; Choi & Clayton 2001; Ricco & Quadrio 2008).

As a final comment, Lozano-Durán *et al.* (2018) showed in a preliminary work that turbulence was not sustained when $\mathcal{L}(U)$ was stabilised by $\mathcal{L}(U) - \mu\mathcal{I}$, where $\mu > 0$ is a damping parameter and \mathcal{I} is the identity operator. However, it can be shown that introducing the linear drag $-\mu\mathbf{u}'$ reduces the gains supported by $\mathcal{L}(U)$ by a factor of $\exp(-2\mu T)$, with T the optimisation time. Hence, stabilising $\mathcal{L}(U)$ via a linear drag term $-\mu\mathbf{u}'$ also disrupts the transient growth mechanism severely and this was the cause for the lack of sustained turbulence in Lozano-Durán *et al.* (2018). Conversely, we have shown that $\tilde{\mathcal{L}}(U)$ is physically interpretable as the stabilisation of $\mathcal{L}(U)$ via a linear forcing directed toward modal instabilities ($\tilde{\mathcal{L}}(U)\mathbf{u}' \approx \mathcal{L}(U)\mathbf{u}' - \mathcal{F}\mathbf{u}'$, see (6.11)). This entails a much gentler modification which leaves almost intact the transient growth mechanisms of $\mathcal{L}(U)$, as opposed to $\mathcal{L}(U) - \mu\mathcal{I}$.

6.3. Wall turbulence exclusively supported by transient growth

The effect of non-modal transient growth as the main source for energy injection from \mathbf{U} into \mathbf{u}' is now assessed by “freezing” the base flow $U(y, z, t_i)$ at the instant t_i . In order to steer clear of the potential effect of exponential instabilities, the numerical experiment here is performed using the stabilised linear operator $\tilde{\mathcal{L}}(U(y, z, t_i))$. For a

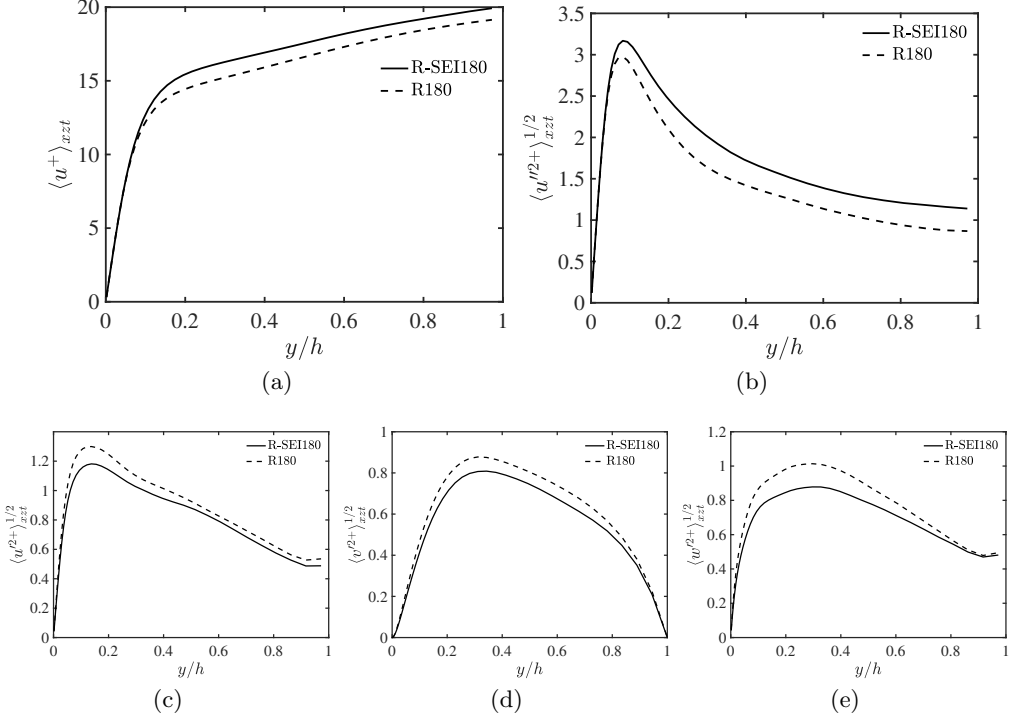


Figure 18: (a) Streamwise mean velocity profile, and (b, c) streamwise, (d) wall-normal, and (e) spanwise mean root-mean-squared fluctuating velocities as a function of the wall-normal distance for the regular channel (R180) (---) and the channel with suppressed exponential instabilities but with the feedback from u' to \mathbf{U} allowed (R-SEI180) (—). Note that the streamwise fluctuating velocity in panel (b) is defined as $u'' = u - \langle u \rangle_{xzt}$, while in panel (c) is defined as $u' = u - U$.

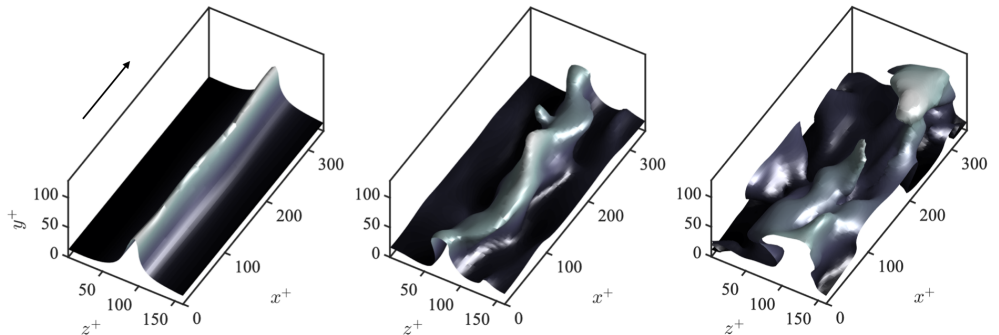


Figure 19: Instantaneous isosurface of the streamwise velocity at different times for R-SEI180. The value of the isosurface is 0.65 of the maximum streamwise velocity. Shading represents the distance to the wall from dark ($y = 0$) to light ($y = h$). The arrow indicates the mean flow direction.

given $U(y, z, t_i)$, we refer to this case as ‘‘channel flow with modally-stable, frozen-in-time base-flow’’, or NF-TG180 $_i$, with i an index indicating the case number. Let us denote the flow for NF-TG180 $_i$ as $\mathbf{u}_{\{i\}}$ (and similarly for other flow quantities). The governing equations for NF-TG180 $_i$ are

$$\frac{\partial \mathbf{u}'_{\{i\}}}{\partial t} = \tilde{\mathcal{L}}_{\{i\}} \mathbf{u}'_{\{i\}} + \mathbf{N}(\mathbf{u}'_{\{i\}}), \quad (6.13)$$

$$U_{\{i\}} = U(y, z, t_i) \text{ from case R180,} \quad (6.14)$$

where $\tilde{\mathcal{L}}_{\{i\}} = \tilde{\mathcal{L}}(U(y, z, t_i))$. The set-up in (6.13) disposes of energy transfers that are due to both modal and parametric instabilities, while allowing the transient growth of fluctuations. For a given t_i , the simulation is initialised from NF-SEI180 at $t = t_i$ (projecting out neutral and unstable modes), and continued for $t > t_i$. We performed more than 500 simulations using different frozen base flows $U(y, z, t_i)$ extracted from R180.

The evolution of the turbulent kinetic energy is shown in figure 20(a) for ten cases NF-TG180 $_i$, $i = 1, \dots, 10$. After freezing the base flow at t_i , most of the cases remain turbulent, while some others decay before $40h/u_\tau$. Turbulence was sustained in 80% of the NF-TG180 $_i$ simulations. In the cases for which turbulence persists, the projection of the flow trajectory onto the $\langle P \rangle_{xyz} - \langle D \rangle_{xyz}$ plane is reminiscent of the self-sustaining cycle for R180; an example is shown in figure 20(b). Since $\tilde{\mathcal{L}}_{\{i\}}$ is modally stable, a key ingredient to sustain turbulence in NF-TG180 $_i$ is the scattering and generation of new disturbances by $\mathbf{N}(\mathbf{u}'_{\{i\}})$. Indeed, we verify in Appendix F that the system (6.13) decays when the nonlinear term $\mathbf{N}(\mathbf{u}'_{\{i\}})$ is discarded.

The one-point statistics for each NF-TG180 $_i$ vary for different $U(y, z, t_i)$. To illustrate the differences among cases, figures 20(c,d,e,f) contain the mean velocity profiles and fluctuating velocities for NF-TG180 $_i$, $i = 1, \dots, 10$. Note that this is only a small sample; the total number of cases simulated is above 500. In some occasions, $U(y, z, t_i)$ is such that the system equilibrates in a state of intensified turbulence with respect to NF-SEI180 (i.e., $\langle E \rangle_{xyzt}$ for NF-TG180 $_i$ larger than for NF-SEI180), while other base flows result in weakened turbulence. Figure 21 shows instances of the streamwise velocity for representative cases with intensified (top panels) and weakened (bottom panels) turbulent states. The intensified turbulence features a highly disorganised state akin to the a broken streak, whereas the weakened turbulence resembles the quiescent stages of wall turbulence with a well-formed persistent streak.

Figure 22 shows the average turbulent kinetic energy of a given case NF-TG180 $_i$ as a function of the maximum gain $G_{\{i\},\max}$ at $T = T_{\max}$. The results reveal that turbulence is not maintained when $G_{\{i\},\max} \lesssim 50$, although this critical gain might be Reynolds number dependent. The trend also suggests that the level of the turbulence intensities for NF-TG180 $_i$ increases with the amount of transient growth supported by $U(y, z, t_i)$ and scales approximately as,

$$\langle E_{\{i\}} \rangle_{xyzt} \sim G_{\{i\},\max}. \quad (6.15)$$

We attempt to explain this observation by invoking the severe assumption that $\mathbf{N}(\mathbf{u}'_{\{i\}})$ acts as a time-varying forcing whose net effect is independent of $\mathbf{u}'_{\{i\}}$, i.e. $\mathbf{N}(\mathbf{u}'_{\{i\}}) \approx \mathbf{N}_{\{i\}}(t)$ (see, for instance Farrell & Ioannou 1993b; Zare *et al.* 2020; Jovanović 2020). Under those conditions, the solution to (6.13) is obtained via the Green’s function as:

$$\mathbf{u}'_{\{i\}}(t) \approx \tilde{\Phi}_{\{i\}}(t - t_i) \mathbf{u}'_{\{i\}}(t_i) + \int_{t_i}^t \tilde{\Phi}_{\{i\}}(t - \tau) \mathbf{N}_{\{i\}}(\tau) d\tau, \quad (6.16)$$

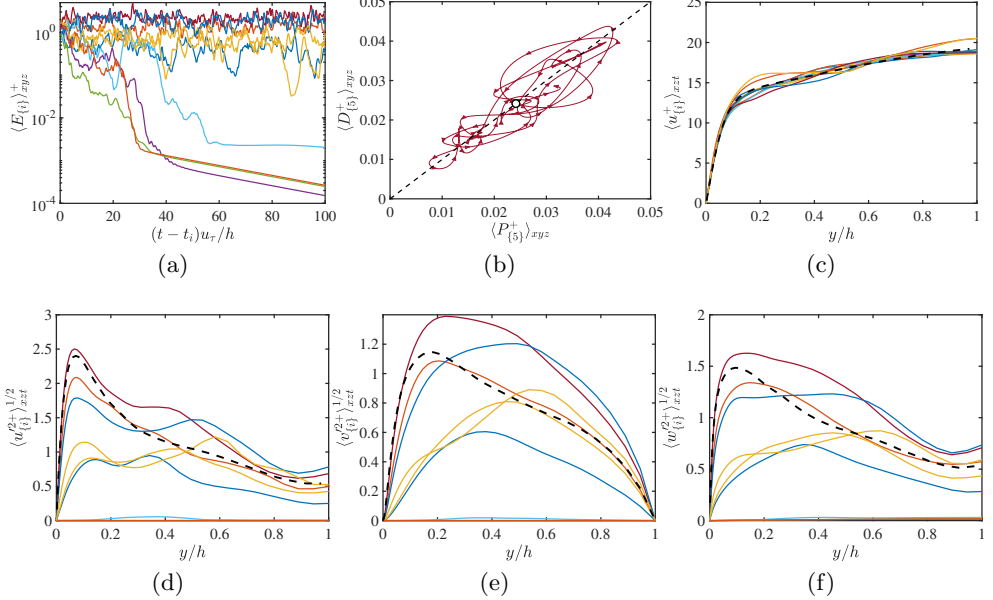


Figure 20: (a) The history of the domain-averaged turbulent kinetic energy of the fluctuations $\langle E_{\{i\}} \rangle_{xyz}$. Different colours denote various case of NF-TG180 $_i$ for $i = 1, \dots, 10$. The time t_i is the instant at which the mean flow is frozen in time. (b) Projection of the flow trajectory onto the average production rate $\langle P_{\{5\}} \rangle_{xyz}$ and dissipation rate $\langle D_{\{5\}} \rangle_{xyz}$ plane for NF-TG180 $_5$. The arrows indicate the time direction of the trajectory, which on average rotates counter-clockwise. The red dashed line is $\langle P_{\{5\}} \rangle_{xyz} = -\langle D_{\{5\}} \rangle_{xyz}$ and the red circle $\langle P_{\{5\}} \rangle_{xyzt} = -\langle D_{\{5\}} \rangle_{xyzt}$. The trajectory projected covers $15h/u_\tau$ units of time. (c) Mean velocity profile, and (d-f) root-mean-squared streamwise, wall-normal, and spanwise fluctuating velocities for ten cases NF-TG180 $_i$, $i = 1, \dots, 10$. The dashed line is for NF-SEI180.

with $\tilde{\Phi}_{\{i\}}(t) = \exp \left[\tilde{\mathcal{L}}_{\{i\}}(t) \right]$. The turbulent kinetic energy of (6.16), after transients, is

$$\langle E_{\{i\}} \rangle_{xyzt} = \frac{1}{2} \left\langle \left(\int_{t_i}^t \tilde{\Phi}_{\{i\}}(t-\tau) \mathcal{N}_{\{i\}}(\tau) d\tau, \int_{t_i}^t \tilde{\Phi}_{\{i\}}(t-\tau) \mathcal{N}_{\{i\}}(\tau) d\tau \right) \right\rangle_t. \quad (6.17)$$

After considering the singular-value decomposition on $\tilde{\Phi}_{\{i\}} = M_{\{i\}} \Sigma_{\{i\}} N_{\{i\}}^\dagger$ then,

$$\langle E_{\{i\}} \rangle_{xyzt} \sim \sigma_{\{i\},\max}^2 \sim G_{\{i\},\max}, \quad (6.18)$$

which establishes a link between the level of turbulent kinetic energy and the non-normal energy gain provided by the linear dynamics as anticipated by figure 22. Nonetheless, the scatter of the data in figure 22 is still large and the relation between $\langle E_{\{i\}} \rangle_{xyzt}$ and $G_{\{i\},\max}$ is not perfectly linear. This is not surprising as the actual mechanism regulating the intensity of turbulence does not depend exclusively on $G_{\{i\},\max}$ but also on the replenishment of fluctuations given by the projection of $\mathbf{N}(\mathbf{u}'_{\{i\}})$ onto $\tilde{\Phi}_{\{i\}}$.

To evaluate the compound result of NF-TG180 $_i$, we define the ensemble average of a

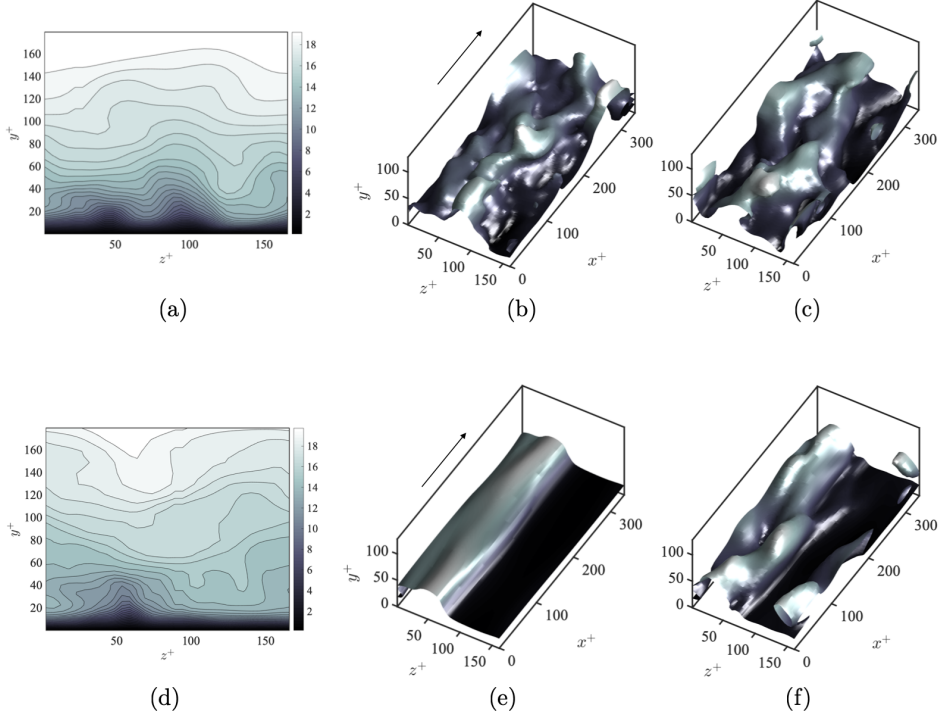


Figure 21: Examples of base flows (a,d) and instantaneous isosurfaces of the streamwise velocity at different times (b,c,e,f). Top panels are for NF-TG180₅, which is representative of a state with weakened turbulence intensities. Bottom panels are for NF-TG180₁₀, which is representative of a state with intensified turbulence. In panels (b,c,e,f), the value of the isosurfaces is 0.65 of the maximum streamwise velocity and colours represent the distance to the wall located at $y = 0$. The arrow indicates the mean flow direction.

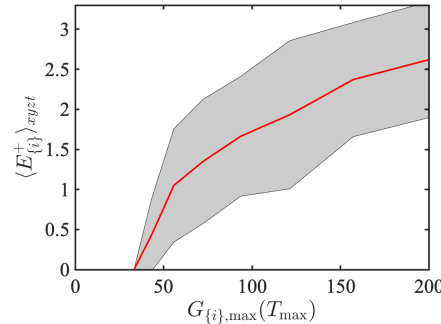


Figure 22: Mean turbulent kinetic energy conditioned to the maximum gain $G_{\{i\},\max}$ at $T = T_{\max}$ compiled over NF-TG180_i; (—) represents the mean value; the shaded area is \pm one standard deviation.

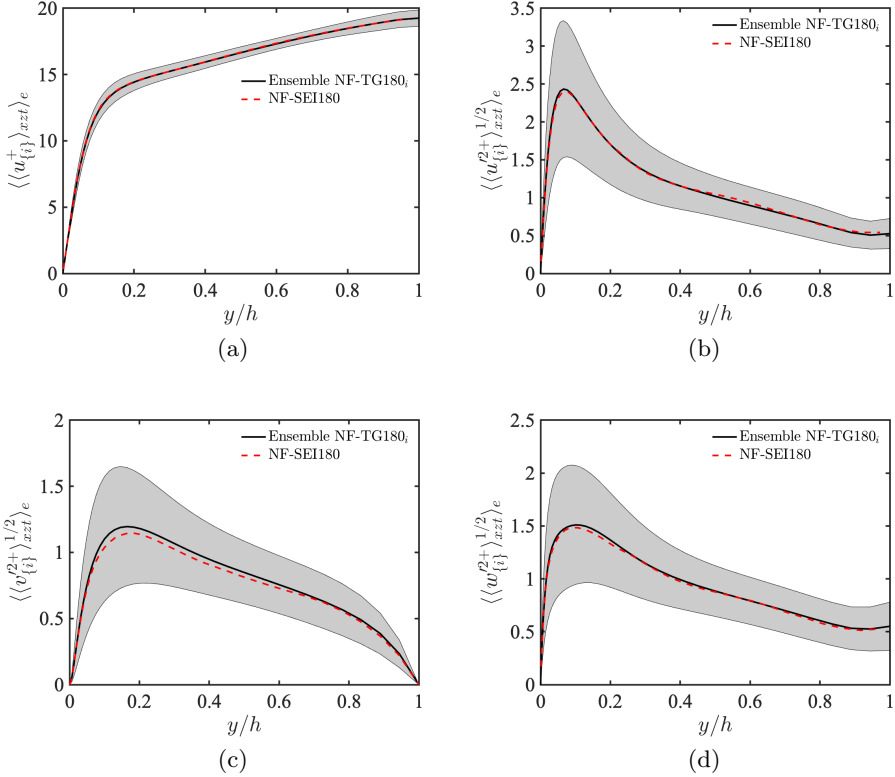


Figure 23: (a) Mean velocity profile, (b) root-mean-squared streamwise, (c) wall-normal, and (d) spanwise fluctuating velocities: (—), the ensemble average of turbulent cases NF-TG180_i , namely, $\langle\langle u_{\{i\}} \rangle_{xzt} \rangle_e$, $\langle\langle u_{\{i\}}'^2 \rangle_{xzt} \rangle_e^{1/2}$, $\langle\langle v_{\{i\}}'^2 \rangle_{xzt} \rangle_e^{1/2}$, and $\langle\langle w_{\{i\}}'^2 \rangle_{xzt} \rangle_e^{1/2}$; the shaded region is \pm one standard deviation with respect to the ensemble average operator $\langle \cdot \rangle_e$; (---) is $\langle u'^2 \rangle_{xzt}$, $\langle v'^2 \rangle_{xzt}$, and $\langle w'^2 \rangle_{xzt}$ for NF-SEI180.

quantity $\phi_{\{i\}}$ over cases NF-TG180_i as

$$\langle \phi_{\{i\}} \rangle_e = \sum_{i=1}^N \frac{\phi_{\{i\}}}{N}, \quad (6.19)$$

where $1, \dots, N$ is the collection of cases NF-TG180_i which remain turbulent. The ensemble average of the mean and rms fluctuating velocities are presented in figure 23. The results are compared with those from NF-SEI180, which is similar to NF-TG180_i but with time-varying U . The outcome is striking: the ensemble averages over NF-TG180_i cases (black solid lines) coincide almost perfectly with the one-point statistics for NF-SEI180 (dashed red lines). Given that the current setup is composed of ‘static’ base flows, $\partial U / \partial t (= 0)$ does not play any role in the flow dynamics of NF-TG180_i . Thus, we conclude that parametric instabilities (intimately related to $\partial U / \partial t$) are not required to sustain the flow. Time-variations of U are only necessary to sample the phase space of ‘regular’ turbulence with different non-normal gains so that the ensemble of NF-TG180_i results in nominal wall turbulence statistics.

The wall-normal behaviour of the turbulence intensities for NF-TG180_i are determined

by the fluctuation energy balance

$$\langle \mathbf{u}'_{\{i\}} \cdot \tilde{\mathcal{L}}_{\{i\}} \mathbf{u}'_{\{i\}} + \mathbf{u}'_{\{i\}} \cdot \mathbf{N}(\mathbf{u}'_{\{i\}}) \rangle_{xzt} = 0. \quad (6.20)$$

Similarly, the average turbulent kinetic energy for NF-SEI180 is dictated by the balance

$$\langle \mathbf{u}' \cdot \tilde{\mathcal{L}}(U) \mathbf{u}' + \mathbf{u}' \cdot \mathbf{N}(\mathbf{u}') \rangle_{xzt} = 0, \quad (6.21)$$

where $\tilde{\mathcal{L}}(U)$ and \mathbf{u}' are now the linear operator and velocity vector, respectively, for case NF-SEI180. The excellent agreement between NF-SEI180 and the ensemble average over NF-TG180_i suggests that

$$\langle \mathbf{u}'_{\{i\}} \cdot \tilde{\mathcal{L}}_{\{i\}} \mathbf{u}'_{\{i\}} \rangle_{xzte} \approx \langle \mathbf{u}' \cdot \tilde{\mathcal{L}} \mathbf{u}' \rangle_{xzt}. \quad (6.22)$$

An interpretation of (6.22) (and of figure 23) is that the collection of linear transient-growth events due to frozen $U(y, z, t_i)$ at different instances t_i provides an accurate representation of the actual time-varying energy transfer from \mathbf{U} to \mathbf{u}' in NF-SEI180. From a dynamical-systems viewpoint: the sampling of the phase-space under the time-varying U is statistically equivalent to an ensemble average of solutions in equilibrium with frozen instances of U . This is an indication that the nonlinear dynamics supported by \mathbf{N} are in quasi-equilibrium with $\mathcal{L}(U)$, i.e., the way the energy is input into the system changes slowly in time. The latter argument can be posed in terms of the time scales of the base flow T_U and turbulent kinetic energy T_E . Defining T_U as the time at which the auto-correlation of U (see (4.12)) decays to 0.5 (similarly for T_E from the auto-correlation of E), the ratio T_U/T_E is found to be roughly 10. Therefore, changes in the base flow are ten times slower than changes in the turbulent kinetic energy, which is consistent with the discussion above.

As a final note, in a preliminary work Lozano-Durán *et al.* (2020) noticed that turbulent channel flows decayed when freezing the base flow, which may initially seem inconsistent with the present results. However, a main difference is that in the present work we are imposing the base flow from actual wall turbulence (R180), while Lozano-Durán *et al.* (2020) imposed a base flow from modified turbulence. The statistical sample used in the present work is also larger than in Lozano-Durán *et al.* (2020).

6.4. Distilling the transient growth mechanisms

We have shown above that transient growth is the simplest linear model to explain self-sustaining turbulence. In this section we further dissect the relevance of different transient growth mechanisms and the implications for the streaky structure of the base flow. We turn our attention back to (6.2), which can be written as

$$\frac{\partial u'}{\partial t} = -U_0 \frac{\partial u'}{\partial x} - v' \frac{\partial U_0}{\partial y} - w' \frac{\partial U_0}{\partial z} - \frac{1}{\rho} \frac{\partial p'}{\partial x} + \nu \nabla^2 u' + N_{u'}, \quad (6.23a)$$

$$\frac{\partial v'}{\partial t} = -U_0 \frac{\partial v'}{\partial x} - \frac{1}{\rho} \frac{\partial p'}{\partial y} + \nu \nabla^2 v' + N_{v'}, \quad (6.23b)$$

$$\frac{\partial w'}{\partial t} = -U_0 \frac{\partial w'}{\partial x} - \frac{1}{\rho} \frac{\partial p'}{\partial z} + \nu \nabla^2 w' + N_{w'}, \quad (6.23c)$$

$$0 = \frac{\partial u'}{\partial x} + \frac{\partial v'}{\partial y} + \frac{\partial w'}{\partial z}, \quad (6.23d)$$

where we have explicitly expanded the linear components, and $N_{u'}$, $N_{v'}$ and $N_{w'}$ stand for the remaining nonlinear terms. The baseflow is $U_0 = U(y, z, t)$ from case R180 (no

feedback from u' to U). Equations (6.23) allow for exponential and parametric instabilities, but we have shown that these are inconsequential for sustaining the flow. Hence, we admit the possibility of both instabilities for the sake of reducing the computational cost of solving (6.23).

We define the streak flow by $U_{\text{streak}} = U_0(y, z, t) - \langle u \rangle_{xz}$, and proceed to examine three transient growth mechanisms:

- i) Linear lift-up of the streak by $-v' \partial U_{\text{streak}} / \partial y$ in (6.23a).
- ii) Linear push-over of the streak by $-w' \partial U_{\text{streak}} / \partial z$ in (6.23a).
- iii) Linear Orr of the streak by $-\partial p' / \partial y$ in (6.23b) and continuity in (6.23d).

In mechanisms i) and ii), velocities perpendicular to the base-shear $(0, \partial U_0 / \partial y, \partial U_0 / \partial z)$ extract energy from the latter to energise the streamwise perturbations, which persist after transients (Ellingsen & Palm 1975). For perturbations in the form of v' , the active linear term for energy transfer is $-v' \partial U_{\text{streak}} / \partial y$, which is referred to as lift-up effect. For perturbations in the form of w' , the energy is transferred through $-w' \partial U_{\text{streak}} / \partial z$. We label the latter as ‘push-over effect’ to make a clear distinction from the lift-up mechanism. The terminology varicose and sinuous is commonly used to refer to the perturbations from mechanism i) and mechanism ii), respectively. In mechanism iii), velocities perpendicular to the base-shear are amplified when backwards-leaning perturbations are tilted forward until they are roughly normal to the base-shear, and are damped as they continue to be tilted past that point. Mechanisms i) and ii) occurs concurrently with mechanisms iii), but the amplification in the latter is driven by continuity. In mechanisms iii), the pressure inhibits the cross-shear velocities when the structures are strongly tilted, and releases the inhibition when they are closer to vertical (Orr 1907; Jiménez 2013).

We perform three additional experiments each aiming to suppress one of the linear mechanisms discussed above. In the first experiment, we modify (6.23a) to suppress the linear lift-up of the streak,

$$\frac{\partial u'}{\partial t} = -U_0 \frac{\partial u'}{\partial x} - v' \cancel{\frac{\partial U_{\text{streak}}}{\partial y}} - v' \frac{\partial \langle u \rangle_{xz}}{\partial y} - w' \frac{\partial U_{\text{streak}}}{\partial z} - \frac{1}{\rho} \frac{\partial p'}{\partial x} + \nu \nabla^2 u' + N_{u'}, \quad (6.24)$$

while the equations for v' , w' and continuity remain intact. We labelled this case as NF-NFU180 (no-feedback & no-lift-up). The second experiment consists of a channel without linear push-over mechanism of the streak,

$$\frac{\partial u'}{\partial t} = -U_0 \frac{\partial u'}{\partial x} - v' \frac{\partial U_{\text{streak}}}{\partial y} - v' \frac{\partial \langle u \rangle_{xz}}{\partial y} - w' \cancel{\frac{\partial U_{\text{streak}}}{\partial z}} - \frac{1}{\rho} \frac{\partial p'}{\partial x} + \nu \nabla^2 u' + N_{u'}, \quad (6.25)$$

which is referred to as NF-NPO180 (no-feedback & no-push-over). Again the equations for v' , w' and continuity remain the same. In the third experiment, we modify the linear dynamics of v' to constrain mechanism iii). The equation dictating the linear Orr is given by

$$\frac{\partial v'_{\text{linear}}}{\partial t} + U_0 \frac{\partial v'_{\text{linear}}}{\partial x} = -\frac{1}{\rho} \frac{\partial p'_{\text{linear}}}{\partial y}, \quad (6.26)$$

where we have neglected the viscous effects. As seen in (6.26), the Orr amplification of v'_{linear} is controlled by p'_{linear} , which is the only source term in the right-hand side of the equation. The linear pressure can be easily obtained by solving

$$\frac{1}{\rho} \nabla^2 p'_{\text{linear}} = -2 \frac{\partial U_0}{\partial y} \frac{\partial v'}{\partial x} - 2 \frac{\partial U_0}{\partial z} \frac{\partial w'}{\partial x}. \quad (6.27)$$

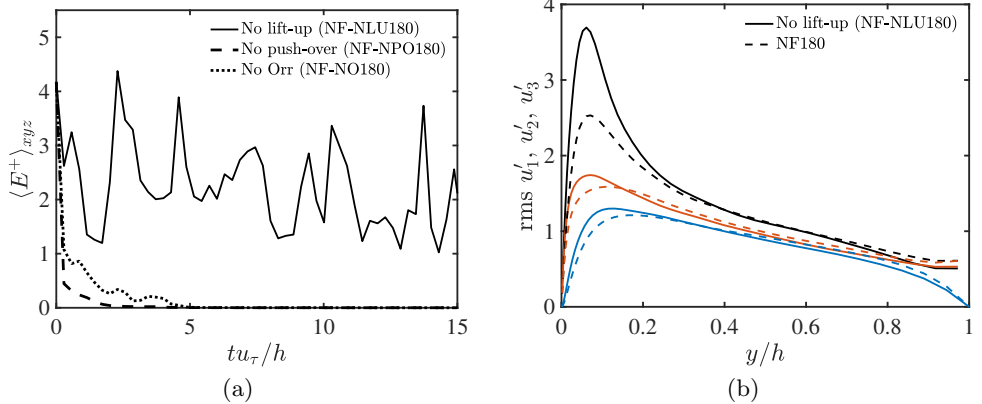


Figure 24: (a) The history of the domain-averaged turbulent kinetic energy of the fluctuations $\langle E \rangle_{xyz}$ for NF-NLU180 (—); NF-NPO180 (---); and NF-NO180 (····). The time $t = 0$ is the instant at which the simulation are started. (a) The root-mean-squared streamwise (— and ---), wall-normal (— and ---), and spanwise (— and ---) fluctuating velocities for NF-NLU180 (solid lines) and NF180 (dashed lines).

If we focus on the linear pressure induced by the streak, then

$$\frac{1}{\rho} \nabla^2 p'_{\text{linear}} = -2 \frac{\partial U_{\text{streak}}}{\partial y} \frac{\partial v'}{\partial x} - 2 \frac{\partial U_{\text{streak}}}{\partial z} \frac{\partial w'}{\partial x}. \quad (6.28)$$

We inhibit the linear Orr mechanism of the streak by introducing a forcing term f_{Orr} in the right-hand-side of the v' equation to counteract the gradient of the linear pressure

$$f_{\text{Orr}} = -\frac{1}{\rho} \frac{\partial p'_{\text{linear}}}{\partial y}. \quad (6.29)$$

Then, the system (6.23a)-(6.23d) is modified by replacing (6.23b) by

$$\frac{\partial v'}{\partial t} = -U_0 \frac{\partial v'}{\partial x} - \frac{1}{\rho} \frac{\partial p'}{\partial y} + \nu \nabla^2 v' + N_{v'} - f_{\text{Orr}}. \quad (6.30)$$

We refer to this case as NF-NO180 (no-feedback & no-Orr).

The three cases are initialised using flow fields from NF180. Different initial conditions were tested and the subsequent evolution of the flow was similar regardless of the details of the initial velocity. The evolution of the turbulent kinetic energy for one initialisation is shown in figure 24(a). The case without streak lift-up (NF-NLU180) is the only one sustained. The rms velocity fluctuations after transients for NF-NLU180 are shown in figure 24(b). Interestingly, blocking the streak lift-up enhances u'_1 close to the wall, implying that the wall-normal variations of the streak provides a stabilising effect. Conversely, the cases without streak push-over (NF-NPO180) or Orr mechanisms (NF-NO180) decay in less than $5u_\tau/h$. Therefore we conclude that both streak push-over and Orr amplification are essential transient growth mechanisms for sustaining the fluctuations. Three more cases analogous to NF-NLU180, NF-NPO180, and NF-NO180 were conducted by allowing the feedback of the fluctuations back into the base flow. The conclusions drawn for these cases are similar to the ones presented above, and they are not included here for the sake of brevity.

The necessity of push-over ($-w' \partial U_{\text{streak}} / \partial z$) points at the spanwise variations of U_{streak}

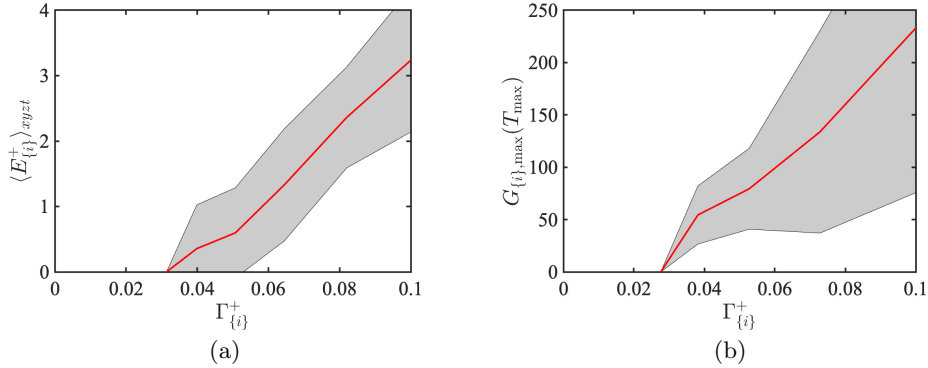


Figure 25: (a) Mean turbulent kinetic energy and (b) maximum gain $G_{\{i\},\max}$ at $T = T_{\max}$ conditioned to the marker for the spanwise-shear strength $\Gamma_{\{i\}} = \langle (\partial U_0(y, z, t_i)/\partial z)^2 \rangle_{yzt}^{1/2}$ compiled over NF-TG180 $_i$; (—) represents the mean value; the shaded area is \pm one standard deviation.

(similarly of U_0) as a key structural feature to sustain turbulence. To test this claim, we resort to the cases NF-TG180 $_i$ presented in §6.3 and inspect their mean turbulent kinetic energy conditioned to the marker for the spanwise-shear strength

$$\Gamma_{\{i\}} = \left\langle \left(\frac{\partial U_{\text{streak}}(y, z, t_i)}{\partial z} \right)^2 \right\rangle_{yzt}^{1/2}. \quad (6.31)$$

The results, shown in figure 25(a), corroborate the hypothesis that the average kinetic energy of the flow depends on the strength of $\partial U_{\text{streak}}(y, z, t_i)/\partial z$. Additionally, frozen base flows with $\Gamma_{\{i\}}$ below the critical value of $\Gamma_{\{i\},c}^+ \approx 0.03$ are too feeble to maintain turbulence. This is further supported by figure 25(b), which shows that the maximum gain of the base flow also increases with $\Gamma_{\{i\}}$. A visual impression of base flows that are either able or unable to sustain turbulence can be gained from the examples shown in figure 26. The message conveyed by figure 26 agrees with the discussion above: base flows capable of sustaining turbulence are accompanied by strong spanwise variations, $\partial U_{\text{streak}}/\partial z$, while base flows unable to maintain turbulence have milder $\partial U_{\text{streak}}/\partial z$.

7. Conclusions

We have investigated the processes responsible for the energy transfer in wall turbulence from the streamwise-averaged mean-flow $U(y, z, t)$ to the fluctuating flow $\mathbf{u}'(x, y, z, t)$. This energy transfer is the backbone of self-sustaining wall turbulence and a subject of heated debates. It has long been hypothesised that the mechanism by which the energy is transferred from U to \mathbf{u}' can be captured by the linearised Navier–Stokes equations and various linear theories stand as tenable candidates to rationalise this process. The most prominent theories are exponential instabilities of the base flow, neutral modes, non-modal transient growth, and non-modal transient growth supported by parametric instability, among others (see table 1). To date, a conclusive study regarding the role played by each linear mechanism has been elusive due to the lack of methodologies designed to unveil causal inference in the flow.

In the present work, we have used cause-and-effect analysis based on interventions

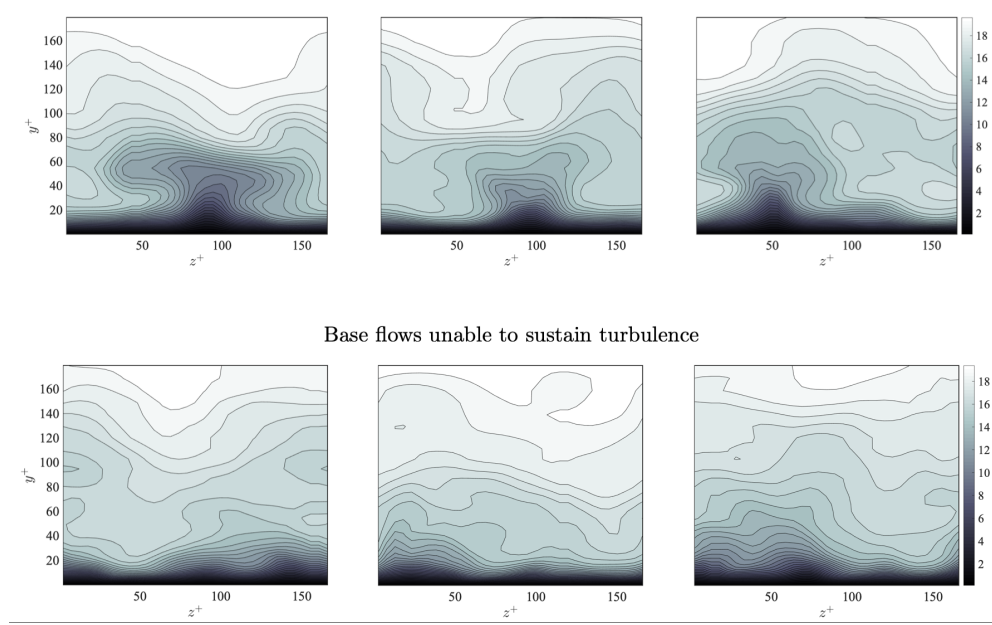


Figure 26: Examples of base flows able to support turbulence (three top panels) and unable to support turbulence (three bottom panels) from cases NF-TG180_i discussed in §6.3.

to assess the role played by different linear mechanisms in sustaining turbulence. The approach is rooted on the concept that manipulation of the causing variable leads to changes in the effect. To that end, we sensibly modified the Navier–Stokes equations of a turbulent channel flow to preclude one or various linear mechanisms participating in the energy transfer from U to \mathbf{u}' . We devised a set of numerical experiments tailored for minimal turbulent channel units at $Re_\tau \approx 180$ in which the feedback from $\mathbf{u}' \rightarrow U$ is blocked to isolate the energy transfer from $U \rightarrow \mathbf{u}'$. The active linear mechanisms for each numerical experiment and its consequences are summarised in table 2. In the first set of the experiments, the linear Navier–Stokes operator is modified to render any exponential instabilities of the streaks stable, thus precluding the energy transfer from $U \rightarrow \mathbf{u}'$ via exponential growth or interaction with neutral modes. In the second set of experiments, we simulated turbulent channel flows with prescribed, frozen-in-time, exponentially stable base flows, such that both parametric instabilities as well as exponential instabilities are suppressed. The last set of experiments is devoted to further pinpoint the process for energy transfer via transient growth by constraining the linear Orr, lift-up, or push-over mechanisms, the latter being analogous to the lift-up effect but in the spanwise direction.

The main contribution of this work is to establish that transient growth alone is capable of sustaining wall turbulence with realistic mean velocity and turbulence intensities in the absence of exponential instabilities, neutral modes, and parametric instabilities. We have further shown that transient growth originates mostly from the Orr/push-over mechanisms due to spanwise variations of U . Our results are obtained for the fully nonlinear Navier–Stokes equations in which the scattering of fluctuations by the nonlinear term is required in combination with transient growth. Exponential instabilities also manifest in the flow, but they are only responsible for about 10% of the turbulent fluctuating

velocities, and more importantly, turbulence persists when they are inhibited. We have also shown that turbulence persists when disposing of parametric instabilities by using exponentially-stable frozen-in-time base flows. In these cases, the statistics of the resulting turbulence depend on the particular frozen base-flow selected. However, the ensemble average of cases with different frozen-in-time base-flows reproduces the statistics of actual (time-varying- U) turbulence with striking accuracy. This was justified by showing that the way the energy is input from U into the system changes slowly compared to the nonlinear dynamics of \mathbf{u}' . In summary, turbulence statistics are essentially explained by linear transient growth in conjunction with nonlinear scattering.

The outcome of this study is consistent with Schoppa & Hussain (2002). However, as inferred from the literature review in table 1, the transient-growth scenario is far from being widely accepted. The possibility of turbulence exclusively supported by transient growth has been long hypothesised (Trefethen *et al.* 1993), but its relevance has never been persuasively shown in the full Navier–Stokes equations using cause-and-effect analysis. To our best knowledge, our results are the most conclusive demonstration of transient growth (via Orr/push-over) as a key driving mechanisms of self-sustaining turbulence. It is important to emphasise that our conclusions do not imply that other mechanisms are not active in wall turbulence. Indeed, we have shown that modal instabilities do manifest in the flow, and to some extent this and other mechanisms have been observed by previous investigators. We have also shown that time-variations of U are necessary to sample the perturbation phase-space and recovery nominal turbulence statistics. The picture promoted here is that the linear energy transfer via transient growth overwhelms others competing mechanisms and, as such, is able to explain most of the flow statistics. This simplifies the conceptual model of wall turbulence and unravels the linear processes that should be targeted in turbulence modelling and control.

Our conclusions regarding the dynamics of wall turbulence were drawn using direct numerical simulations of the Navier–Stokes equations at low Reynolds numbers representative of the buffer layer. It remains to establish whether similar conclusions apply to higher Re_τ . The analysis was also performed in channels computed using minimal flow units, chosen as simplified representations of naturally occurring wall turbulence. Yet, we have shown that our results are qualitatively similar when the domain size is doubled. We expect that the approach presented here paves the way for future investigations at high-Reynolds-numbers turbulence obtained in larger unconstrained domains, in addition to extensions to different flow configurations in which the role of linear mechanisms remains unsettled.

This work was also supported by the Coturb project of the European Research Council (ERC-2014.AdG-669505) during the 2019 Coturb Turbulence Summer Workshop at the Universidad Politécnica de Madrid. M.-A.N. acknowledges the support of the Hellenic Foundation for Research and Innovation, and the General Secretariat for Research and Technology (Grant No. 1718/14518). A.L.-D. acknowledges the support of the NASA Transformative Aeronautics Concepts Program (Grant No. NNX15AU93A) and the Office of Naval Research (Grant No. N00014-16-S-BA10). N.C.C. was supported by the Australian Research Council (Grant No. CE170100023). We thank Jane Bae, Brian Farrell, Petros Ioannou, and Javier Jiménez for insightful discussions.

Declaration of Interests

The authors report no conflict of interest.

Appendix A. Sensitivity to the size of the computational domain

The minimum size of the computational domain required to sustain turbulence in channels at low Reynolds number was extensively studied by Jiménez & Moin (1991). The streamwise and spanwise lengths of our simulations were selected to comply with these minimum requirements. We also verified that decreasing the streamwise (L_x) and spanwise (L_z) extends of our domain any further in the current setup leads to laminarisation of the flow. In this appendix, we focus on the sensitivity of our results to increasing L_x and L_z . The former is potentially the most critical length as the base flow is defined by taking the streamwise average of u . We have also seen that the most dangerous instabilities occur for the wavenumber $k_x = 2\pi/L_x$, which is the harmonic excitation and, hence, might be susceptible to changes in L_x . Therefore, we centre our attention on L_x and the role of subharmonic instabilities. Some comments are made at the end of the appendix on the sensitivity to L_z .

Prior to conducting the sensitivity analysis for L_x , we can anticipate that the subharmonic instabilities associated with $k_x = 2\pi/(nL_x)$ with $n > 1$ are probably of little relevance for sustaining the flow. The most obvious reason is that wavenumbers equal or smaller than $k_x = \pi/L_x$ are not accommodated in the domain (they simply do not fit in x) and subharmonic instabilities cannot manifest in the flow. Given that our simulations show that turbulence is sustained with realistic mean profile and fluctuating velocities for the chosen L_x , the importance of the (nonexistent) subharmonic instabilities must be minor. To ascertain that this is the case, we i) perform an *a posteriori* analysis of the stability of $U(y, z, t)$ assuming that instabilities from $k_x = \pi/L_x$ are realisable, and ii) conduct additional simulations by doubling the streamwise domain.

We study the stability of $U(y, z, t)$ from case R180, similar to the analysis in §4.1. In this occasion, we focus on the growth rates for perturbations with streamwise wavenumbers $k_x = \pi/L_x$ and $k_x = 2\pi/L_x$ denoted by $\lambda_{\max}^{k_x=\pi/L_x}$ and $\lambda_{\max}^{k_x=2\pi/L_x}$, respectively. It is important to remark that $\lambda_{\max}^{k_x=\pi/L_x}$ is the hypothetical growth rate of exponential instabilities with wavenumber $k_x = \pi/L_x$ if they were allowed to manifest in the flow (which they are not). The p.d.f. of the ratio $\lambda_{\max}^{k_x=2\pi/L_x}/\lambda_{\max}^{k_x=\pi/L_x}$ for a given base flow at time t_i , $U(y, z, t_i)$, is plotted in figure 27(a), and shows that the harmonic instability (which are realisable in the simulation) prevails over the (hypothetical) subharmonic instability. The data also reveal that $\lambda_{\max}^{k_x=2\pi/L_x} > \lambda_{\max}^{k_x=\pi/L_x}$ about 80% of the time. The result proves that the base flows for case R180 are more receptive to harmonic instabilities than they are to subharmonic instabilities.

The second analysis consists of an actual simulation with streamwise domain length equal to $2L_x^+ \approx 673$ ($2L_x \approx 3.66h$), such that the instabilities associated with $k_x = \pi/L_x$ are now allowed in the flow (L_x and L_z signify the domain size of R180). We label this case as R-2Lx-180, which is analogous to R180 but with doubled streamwise domain length. Figure 28 illustrates the flow decomposition into base flow and fluctuations for R-2Lx-180 and figure 29 depicts three examples of base flows. Consistently, the base flows for R-2Lx-180 are defined as $U(y, z, t) = \langle u \rangle_x = 1/2L_x \int_0^{2L_x} u dx$.

Figure 30 shows the rms fluctuating velocities for R-2Lx-180 compared with the minimal channel flow R180. The main effect of enlarging the domain in x is an increase in u' , which comes from the larger scales accommodated by the computational box. The energy in u' is now closer to the nominal value in non-minimal domains, but we have argued in §3 that this additional energy is not strictly required to sustain turbulence.

The stability analysis of $U(y, z, t)$ for R-2Lx-180 and wavenumbers $k_x = \pi/L_x$ and $k_x = 2\pi/L_x$ is included in figure 27(b). The outcome is similar to R180: $\lambda_{\max}^{k_x=2\pi/L_x}$

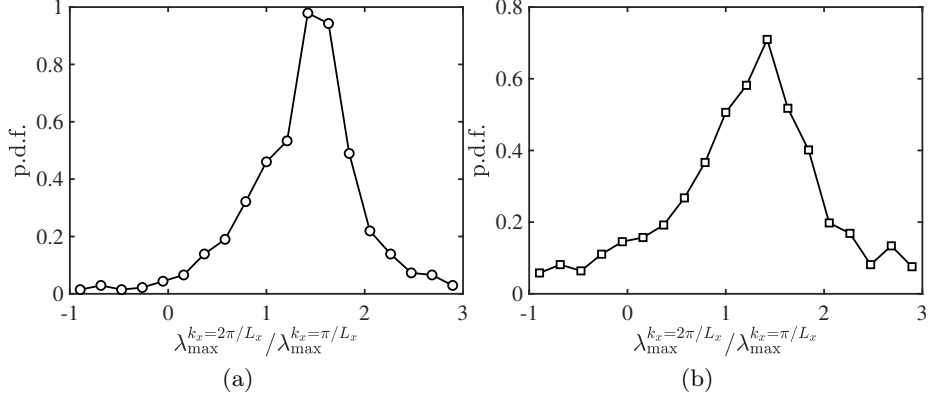


Figure 27: The probability density function of the ratio of the largest growth rates $\lambda_{\max}^{k_x=2\pi/L_x} / \lambda_{\max}^{k_x=\pi/L_x}$ of a given base flow at time t_i , $U(y, z, t_i)$ for (a) case R180 and (b) case R-2Lx-180.

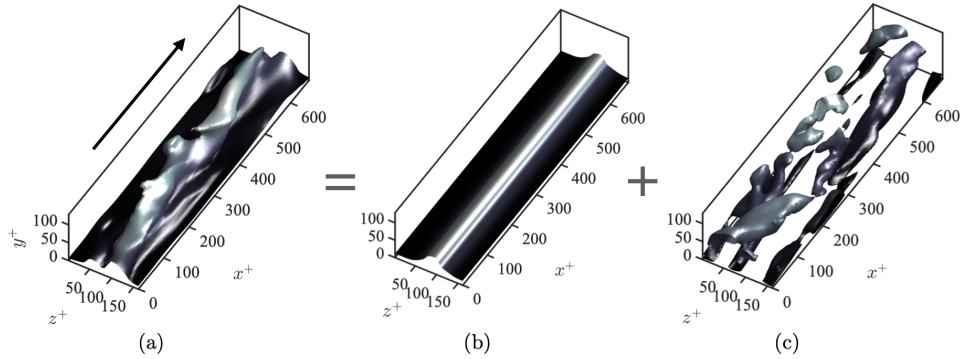


Figure 28: Decomposition of the instantaneous flow into a streamwise mean base flow and fluctuations for case R-2Lx-180. Instantaneous isosurface of streamwise velocity for (a) the total flow u , (b) the streak base flow U , and (c) the absolute value of the fluctuations $|u'|$. The values of the isosurfaces are 0.6 (a and b) and 0.1 (c) of the maximum streamwise velocity. Shading represents the distance to the wall from dark ($y = 0$) to light ($y = h$). The arrow in panel (a) indicates the mean flow direction.

prevails over $\lambda_{\max}^{k_x=\pi/L_x}$ most of the time, and this is true even if now the streamwise domain is $2L_x$. This suggests that the most unstable wavelength should be around the length of the minimal channel.

To complete the analysis and build confidence in the results presented in the paper, we perform two simulations with constrained linear dynamics using R-2Lx-180 as baseline. In the first case, a selected base flow from R-2Lx-180 is frozen in time and the exponential instabilities are removed. We denote this case as NF-TG-2Lx-180 $_{\{1\}}$ (similar to cases NF-TG180 $_{\{i\}}$ in §6.3). In the second case, the linear push-over mechanisms are cancelled out (similar to case NF-NPO180 in §6.4). The cases are initialised from R-2Lx-180,

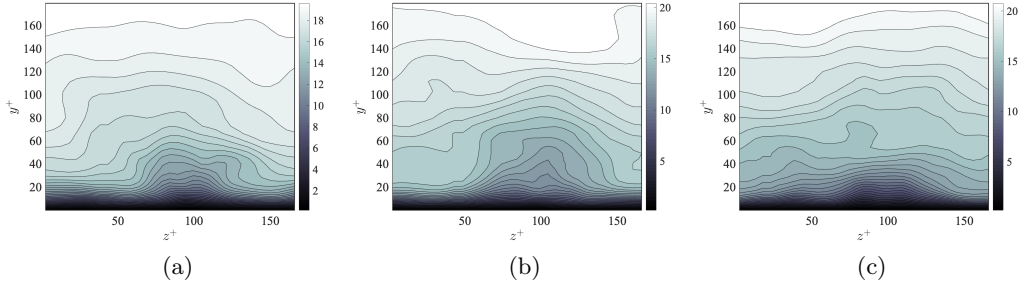


Figure 29: Examples of base flow $U(y, z, t)$ for case R-2Lx-180.

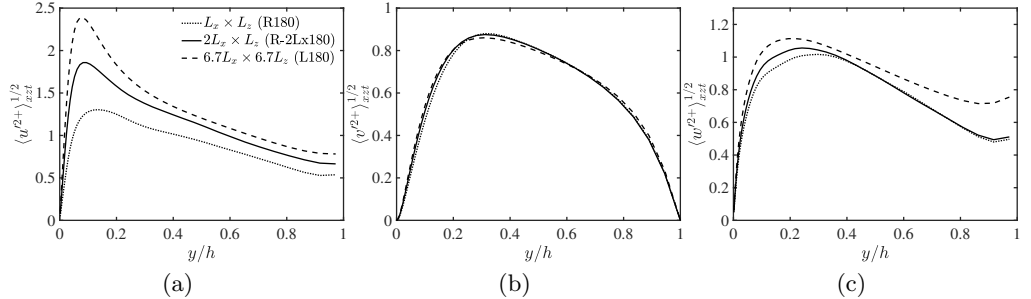


Figure 30: (a) Streamwise (—), (c) wall-normal (---), and (c) spanwise (····) root-mean-squared fluctuating velocities as a function of the wall-normal distance for R-2Lx-180 (—) and equivalent non-minimal channel (L180) with $6.7L_x^+\times 6.7L_z^+ = 2312\times 1156$ ($\approx 12.5h \times 6.3h$) (---), where L_x and L_z signify the channel domain for R180.

although it was assessed that the conclusions are independent of the initial condition. The evolution of the turbulence kinetic energy for both cases is shown in figure 31. For NF-TG-2Lx-180_{1}, turbulence is maintained despite the lack of exponential and parametric instabilities. For the particular base flow chosen in NF-TG-2Lx-180_{1}, the turbulent kinetic energy is on average larger than that for R-2Lx-180, although other base flows (not shown) exhibit a lower value. Conversely, the turbulent kinetic energy decays for NF-NPO-2Lx-180, where the linear push-over is suppressed. Therefore, the main conclusions drawn from simulations with a streamwise domain equal to $2L_x$ are consistent with those discussed in the paper with streamwise domain L_x .

Finally, we carried out simulations analogous to those described above doubling the spanwise length of the domain. Our conclusions remain unchanged. This is not unexpected as enlarging L_z mostly translates into an increment on the number of coherent structures contained in the domain along the z direction. The new channel is not minimal as it contains more than one elementary flow unit, but the characteristics of the base flow are barely affected.

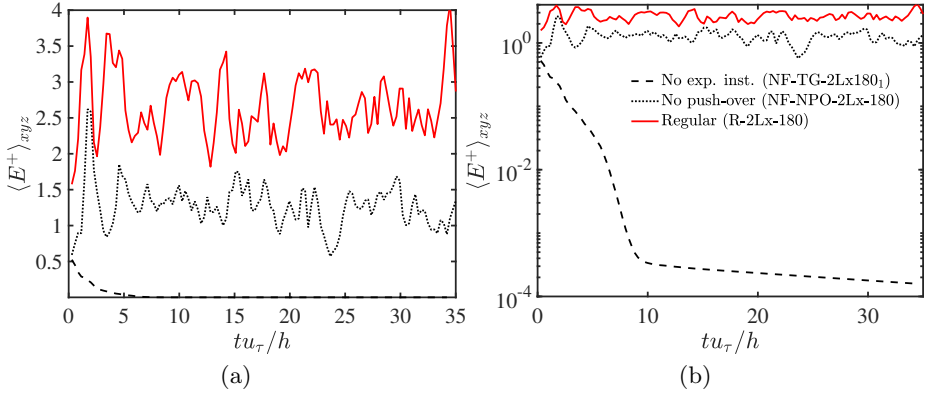


Figure 31: The history of the domain-averaged turbulent kinetic energy of the fluctuations $\langle E \rangle_{xyz}$ for the case with frozen base flow without exponential instabilities (NF-TG-2Lx-180_{1}, —), channel without linear push-over (NF-NPO-2Lx-180, ---), and regular channel flow (R-2Lx-180, ···). The vertical axis is linear in panel (a) and logarithmic in panel (b).

Appendix B. Results for base flow (U, V, W)

For completeness, we repeat the analysis in §6 using this time the streamwise-averaged v and w as part of our base flow, i.e.,

$$\mathbf{U} \stackrel{\text{def}}{=} (U, V, W) = (\langle u \rangle_x, \langle v \rangle_x, \langle w \rangle_x). \quad (\text{B } 1)$$

Consequently, the perturbations are now defined as $u' = u - U$, $v' = v - V$, and $w' = w - W$. We carried out simulations analogous to those discussed in table 2. The conclusions drawn using (U, V, W) as the base flow are similar to those using $(U, 0, 0)$. Here we report some of the key results.

The new equation for \mathbf{U} is obtained by replacing the operator \mathcal{D} used to set the y - and z -components, namely,

$$\mathcal{D} = \begin{bmatrix} 1 & 0 & 0 \\ 0 & 0 & 0 \\ 0 & 0 & 0 \end{bmatrix}, \quad (\text{B } 2)$$

by the identity operator $\mathcal{D} = \mathcal{I}$ such that

$$\frac{\partial \mathbf{U}}{\partial t} + \mathbf{U} \cdot \nabla \mathbf{U} = -\langle \mathbf{u}' \cdot \nabla \mathbf{u}' \rangle_x - \frac{1}{\rho} \nabla \langle p \rangle_x + \nu \nabla^2 \mathbf{U} + \mathbf{f}, \quad (\text{B } 3a)$$

$$\nabla \cdot \mathbf{U} = 0. \quad (\text{B } 3b)$$

The equation for the new fluctuating velocity vector is

$$\frac{\partial \mathbf{u}'}{\partial t} = \mathcal{L}(\mathbf{U}) \mathbf{u}' + \mathbf{N}(\mathbf{u}'), \quad (\text{B } 4a)$$

$$\mathcal{L}(\mathbf{U}) \mathbf{u}' = \mathcal{P} [-\mathbf{U} \cdot \nabla \mathbf{u}' - \mathbf{u}' \cdot \nabla \mathbf{U} + \nu \nabla^2 \mathbf{u}'], \quad (\text{B } 4b)$$

$$\mathbf{N}(\mathbf{u}') = \mathcal{P} [-\mathbf{u}' \cdot \nabla \mathbf{u}' + \langle \mathbf{u}' \cdot \nabla \mathbf{u}' \rangle_x]. \quad (\text{B } 4c)$$

First, we remove the explicit feedback from \mathbf{u}' to (U, V, W) and refer to this case as $\widetilde{\text{NF180}}$ (analogous to NF180). Figure 32 shows that the effect of blocking the feedback from \mathbf{u}' to (U, V, W) is to enhance the fluctuating velocities, similarly to NF180. The

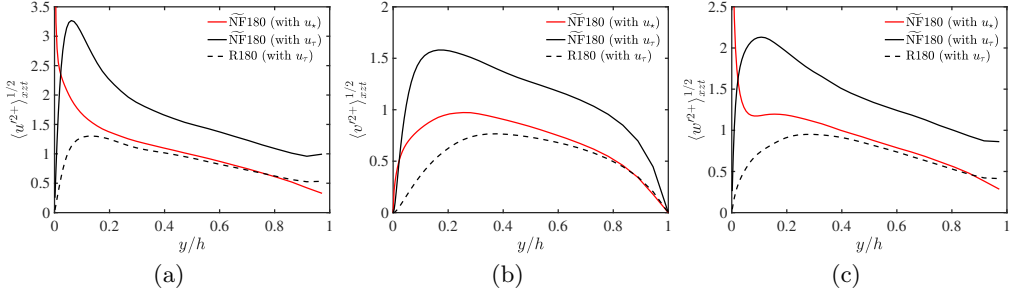


Figure 32: (a) Streamwise, (b) wall-normal, and (c) spanwise mean root-mean-squared fluctuating velocities as a function of the wall-normal distance for case R180 normalised by u_τ (---), case $\widetilde{\text{NF}}180$ normalised by u_τ (—), and $\widetilde{\text{NF}}180$ normalised by u_* (—).

results exhibit an improved collapse when the velocities are scaled by u_* , which is more representative of characteristic flow velocity.

In the second experiment, we remove the exponential instability of the streaks and label the case as $\widetilde{\text{NF-SEI}}180$ (analogous to NF-SE180). The results, included in figure 33 (red dashed lines), show that turbulence is maintained in the absence of exponential instabilities. When comparing $\widetilde{\text{NF-SEI}}180$ with $\widetilde{\text{NF}}180$, the former exhibits a mildly reduced level of fluctuating velocities (similar to the observation from NF-SEI180 compared to NF180).

Finally, we perform simulations freezing the base flow in addition to removing the exponential instabilities as in §6.3. The cases are denoted as $\widetilde{\text{NF-TG}}180_i$ (analogous to $\widetilde{\text{NF-TG}}180_i$). Turbulence is sustained in 90% of the cases. From figure 33, we conclude that the discussion in §6.3 is broadly applicable to the base flow (U, V, W): wall turbulence exclusively supported by transient growth is sustained and able to produce realistic flow statistics.

Appendix C. Details of the stability analysis

In this appendix we describe the linear stability analysis of a base flow, $U(y, z, t)$, which is inhomogeneous in two spatial directions (e.g., Karp & Cohen 2014). At given time $t = t_0$, we assume the following velocity field

$$\mathbf{u} = (U(y, z, t_0), 0, 0) + \varepsilon \mathbf{u}', \quad 0 < \varepsilon \ll 1, \quad (\text{C } 1)$$

where the base flow U is assumed parallel, steady, and streamwise independent, and \mathbf{u}' is the disturbance. Substituting (C1) into the incompressible Navier–Stokes equations (2.1), neglecting terms of order ε^2 and higher, and gathering the terms at order ε , we obtain

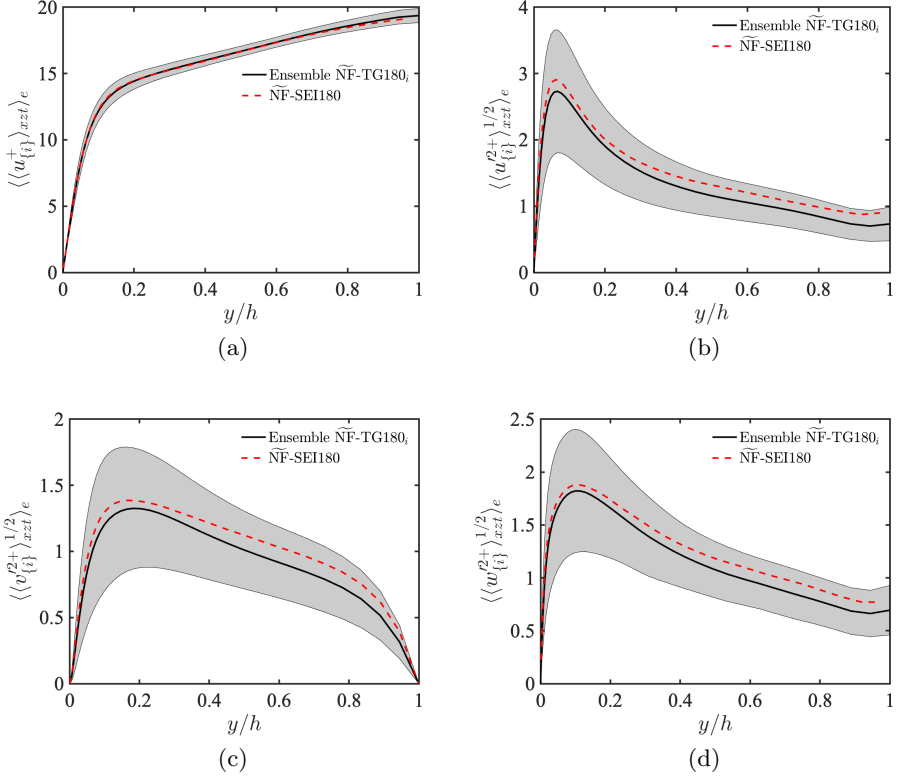


Figure 33: (a) Mean velocity profile, (b) root-mean-squared streamwise, (c) wall-normal, and (d) spanwise fluctuating velocities: (—), the ensemble average of turbulent cases $\widetilde{\text{NF}}\text{-TG180}_i$, namely, $\langle\langle u_{\{i\}} \rangle_{xzt} \rangle_e$, $\langle\langle u'_{\{i\}} \rangle_{xzt}^{1/2} \rangle_e$, $\langle\langle v'_{\{i\}} \rangle_{xzt}^{1/2} \rangle_e$, and $\langle\langle w'_{\{i\}} \rangle_{xzt}^{1/2} \rangle_e$; the shaded region is \pm one standard deviation with respect to the ensemble average operator $\langle \cdot \rangle_e$; (---) is $\langle u'^2 \rangle_{xzt}$, $\langle v'^2 \rangle_{xzt}$, and $\langle w'^2 \rangle_{xzt}$ for $\widetilde{\text{NF}}\text{-SEI180}$.

the linearised equations for the disturbances:

$$\frac{\partial u'}{\partial x} + \frac{\partial v'}{\partial y} + \frac{\partial w'}{\partial z} = 0, \quad (\text{C } 2a)$$

$$\frac{\partial u'}{\partial t} + U \frac{\partial u'}{\partial x} + v' \frac{\partial U}{\partial y} + w' \frac{\partial U}{\partial z} = -\frac{1}{\rho} \frac{\partial p'}{\partial x} + \nu \nabla^2 u', \quad (\text{C } 2b)$$

$$\frac{\partial v'}{\partial t} + U \frac{\partial v'}{\partial x} = -\frac{1}{\rho} \frac{\partial p'}{\partial y} + \nu \nabla^2 v', \quad (\text{C } 2c)$$

$$\frac{\partial w'}{\partial t} + U \frac{\partial w'}{\partial x} = -\frac{1}{\rho} \frac{\partial p'}{\partial z} + \nu \nabla^2 w'. \quad (\text{C } 2d)$$

The boundary conditions are no slip at the wall and free slip for u' and w' and impermeability for v' at the top. Homogeneity in x and t allows us to assume that all flow fields for the disturbances take the form, e.g.,

$$u' = \hat{u}'(y, z) e^{(\lambda + i\omega)t + ik_x x}, \quad (\text{C } 3)$$

where k_x is the streamwise wavenumber, and $\lambda + i\omega$ is the temporal complex eigenvalue. (Similarly for v' , w' , and p' .)

Substituting (C3) into the linearised equations (C2), they can be rearranged as a generalised eigenvalue problem,

$$\begin{pmatrix} \mathbf{D}_x & \mathbf{D}_y & \mathbf{D}_z & \mathbf{O} \\ \mathbf{C} & \mathbf{U}_y & \mathbf{U}_z & \mathbf{D}_x \\ \mathbf{O} & \mathbf{C} & \mathbf{O} & \mathbf{D}_y \\ \mathbf{O} & \mathbf{O} & \mathbf{C} & \mathbf{D}_z \end{pmatrix} \begin{pmatrix} \tilde{u}' \\ \tilde{v}' \\ \tilde{w}' \\ \tilde{p}' \end{pmatrix} = (\lambda + i\omega) \begin{pmatrix} \mathbf{O} & \mathbf{O} & \mathbf{O} & \mathbf{O} \\ -\mathbf{I} & \mathbf{O} & \mathbf{O} & \mathbf{O} \\ \mathbf{O} & -\mathbf{I} & \mathbf{O} & \mathbf{O} \\ \mathbf{O} & \mathbf{O} & -\mathbf{I} & \mathbf{O} \end{pmatrix} \begin{pmatrix} \tilde{u}' \\ \tilde{v}' \\ \tilde{w}' \\ \tilde{p}' \end{pmatrix}. \quad (\text{C4})$$

Here, \mathbf{I} is the identity matrix, \mathbf{O} is a zero matrix, \tilde{u}' is a one-dimensional representation of a two-dimensional vector

$$\tilde{u}' \stackrel{\text{def}}{=} (\hat{u}'(y_1, z_1), \dots, \hat{u}'(y_1, z_{N_z}), \dots, \hat{u}'(y_{N_y}, z_1), \dots, \hat{u}'(y_{N_y}, z_{N_z}))^\top, \quad (\text{C5})$$

and similarly for \tilde{v}' , \tilde{w}' , and \tilde{p}' . Furthermore, the matrices \mathbf{C} , \mathbf{U}_y , \mathbf{U}_z , \mathbf{D}_x , \mathbf{D}_y , and \mathbf{D}_z are given by

$$\mathbf{C} = ik_x \operatorname{diag}(\mathbf{U}) - \nu (\bar{\mathbf{I}}_z \otimes \bar{\mathbf{D}}_y^2 + \bar{\mathbf{D}}_z^2 \otimes \bar{\mathbf{I}}_y - k_x^2 \bar{\mathbf{I}}_z \otimes \bar{\mathbf{I}}_y), \quad (\text{C6a})$$

$$\mathbf{U}_y = \operatorname{diag}\{(\bar{\mathbf{I}}_z \otimes \bar{\mathbf{D}}_y) \mathbf{U}\}, \quad (\text{C6b})$$

$$\mathbf{U}_z = \operatorname{diag}\{(\bar{\mathbf{D}}_z \otimes \bar{\mathbf{I}}_y) \mathbf{U}\}, \quad (\text{C6c})$$

$$\mathbf{D}_x = ik_x \bar{\mathbf{I}}_z \otimes \bar{\mathbf{I}}_y, \quad (\text{C6d})$$

$$\mathbf{D}_y = \bar{\mathbf{I}}_z \otimes \bar{\mathbf{D}}_y, \quad (\text{C6e})$$

$$\mathbf{D}_z = \bar{\mathbf{D}}_z \otimes \bar{\mathbf{I}}_y, \quad (\text{C6f})$$

where \otimes is the Kronecker product and \mathbf{U} is the one-dimensional representation of U (similarly to \tilde{u}'). The matrices $\bar{\mathbf{I}}_y$ and $\bar{\mathbf{I}}_z$ are the identity matrices of dimensions $N_y \times N_y$ and $N_z \times N_z$, respectively, and $\bar{\mathbf{D}}_y$ and $\bar{\mathbf{D}}_z$ are the matrices that represent differentiation in y and z directions, respectively. The eigenvalue problem is solved numerically for all streamwise wavenumbers k_x on-the-fly during the simulations.

Appendix D. Validation of eigenvalue calculation

The eigenvalue calculation described in Appendix C was numerically implemented in the code which solves the equations of motion such that, at a given time t , the eigenvalues of $\mathcal{L}(U(y, z, t))$ are computed on-the-fly. To verify the implementation, a second independent solver was used, which takes as input the base flows $U(y, z, t)$ stored from the simulation. The second algorithm solves the eigenvalues problem in the y -vorticity–Laplacian of v formulation discretised with first-order finite differences in a collocated grid. We have referred to the real part of the eigenvalues computed by the first solver as λ_j . Let us denote the eigenvalues computed by the second solver as $\check{\lambda}_j$. Figure 34 shows the history of the real part of the two most unstable eigenvalues λ_1 and λ_2 , and $\check{\lambda}_1$ and $\check{\lambda}_2$. On average, the error $|\lambda_j - \check{\lambda}_j| / |\lambda_j|$ for all unstable eigenvalues is of the order of 0.1%. These small differences are expected, as the numerical details of the two solvers differ. Yet, the errors are small enough to provide confidence in the calculation of the modal instabilities. An additional validation is presented in Appendix F.

Appendix E. Approximate calculation of $\tilde{\mathcal{L}}(U)$ using linear forcing

This appendix presents an alternative approach to suppress exponential instabilities of $\mathcal{L}(U)$, which aids the interpretation of the stabilisation of the operator. The eigende-

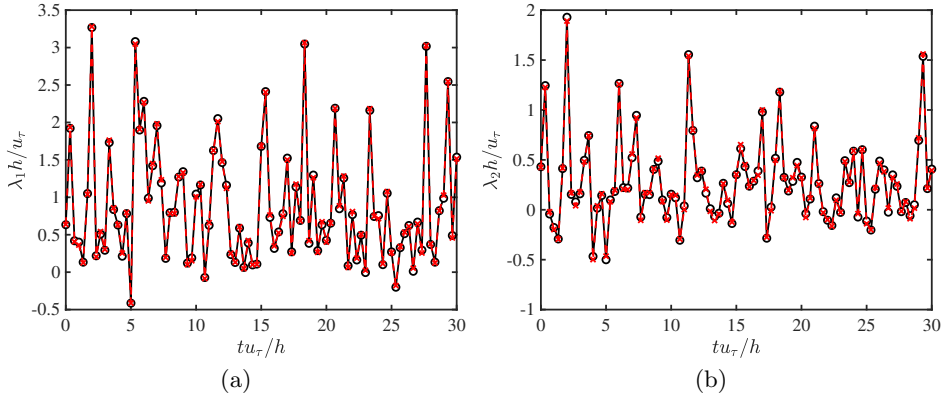


Figure 34: The history of the real part of the two most unstable eigenvalues (a) λ_1 , $\check{\lambda}_1$ and (b) λ_2 , $\check{\lambda}_2$ of $\mathcal{L}(U)$ computed on-the-fly by the solver which integrates the equations of motion for the fluctuating velocities ($-○-$) and computed *a posteriori* by a second independent solver ($-×-$).

composition of a normal operator \mathcal{A} is given by $\mathcal{A} = Q\Lambda Q^\dagger$. Operator \mathcal{A} is stabilised if we subtract its projection to all the eigenspaces that correspond to unstable eigenvalues, i.e., eigenvalues with real part $\lambda_j > 0$, $j = 1, \dots, N$:

$$\hat{\mathcal{A}} = \mathcal{A} - \sum_{j=1}^N a\lambda_j \mathcal{U}_j \mathcal{U}_j^\dagger, \quad (\text{E1})$$

where a is a real coefficient $a > 1$, and \mathcal{U}_j is the j -th eigenmode. The operator $\mathcal{L}(U)$ is nonnormal and, therefore its eigendecomposition relies on Q^{-1} and not Q^\dagger . Thus, an approximation like (E1), i.e.,

$$\hat{\mathcal{L}}(U) = \mathcal{L}(U) - \sum_{i=1}^N 2\lambda_i \mathcal{U}_i \mathcal{U}_i^\dagger \quad (\text{E2})$$

(where we have chosen $a = 2$), is not guaranteed to stabilise \mathcal{L} , although we show here that it works reasonably well. Figure 35 compares the real part of the three most unstable eigenvalues of the properly stabilised $\tilde{\mathcal{L}}(U)$ (denoted by λ_i) and those of $\hat{\mathcal{L}}(U)$ (denoted by $\check{\lambda}_i$). The approximate method $\hat{\mathcal{L}}(U)$ succeeds in stabilising $\mathcal{L}(U)$ with the largest eigenvalues (now stable) obtained within to more than 0.1% accuracy when compared to $\tilde{\mathcal{L}}(U)$.

In addition to providing an intuitive interpretation of the stabilisation, the approximate approach is also included here given its easier implementation using the power method. The power method solves the linearised Navier–Stokes equations rescaling the velocity field amplitude at each time step to track the most unstable mode. The process can be repeated iteratively to obtain approximations of the first, second, third,... most unstable modes and eigenvalues. The advantage of the power method is that it does not require constructing \mathcal{L} explicitly nor performing the eigendecomposition of the operator, which might be beneficial when computing $\mathcal{L}(U)$ is impractical. We repeated cases NF-SEI180 and R-SEI180 using $\hat{\mathcal{L}}(U)$ and tested that our conclusions remains the same.

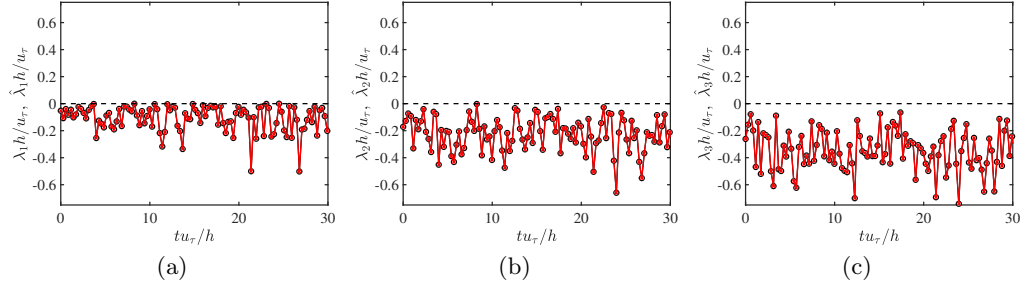


Figure 35: The history of the real part of the three most unstable eigenvalues (a) λ_1 , $\hat{\lambda}_1$, (b) λ_2 , $\hat{\lambda}_2$, (c) λ_3 , $\hat{\lambda}_3$ of $\tilde{\mathcal{L}}(U)$ ($- \circ -$) and $\hat{\mathcal{L}}(U)$ ($- \times -$).

Appendix F. Linear analysis of channel flow with modally-stable base-flow

We consider the governing equations for the linear channel flow with modally-stable frozen base-flow

$$\frac{\partial \mathbf{u}'}{\partial t} = \tilde{\mathcal{L}}(U) \mathbf{u}', \quad (\text{F } 1a)$$

$$\mathbf{U} = (U(y, z, t_0), 0, 0) \text{ from case R180,} \quad (\text{F } 1b)$$

where we have disposed of the nonlinear term $\mathbf{N}(\mathbf{u}')$. We repeat the simulations in §6.3 using the same set-up. As an example, the evolution of the turbulent kinetic energy for ten cases is shown in figure 36(a). Given that $\tilde{\mathcal{L}}(U)$ is modally stable, the turbulent kinetic energy decays without exception. We verified that this was the case for all the simulations considered in § 6.3 once $\mathbf{N}(\mathbf{u}')$ is set to zero. Conversely, if we consider the system

$$\frac{\partial \mathbf{u}'}{\partial t} = \mathcal{L}(U) \mathbf{u}', \quad (\text{F } 2a)$$

$$\mathbf{U} = (U(y, z, t_0), 0, 0) \text{ from case R180,} \quad (\text{F } 2b)$$

in which modal instabilities are allowed, the turbulent kinetic energy grows exponentially as seen in figure 36(b) given that the ten cases considered are all such that $\mathcal{L}(U)$ is modally unstable. It was also verified that the growth rate obtained by integrating (F 2) coincides with the growth rate λ_1 of the most unstable mode as predicted by the eigenvalue analysis of $\mathcal{L}(U)$. The present appendix serves as validation of the successful suppression of modal instabilities in $\mathcal{L}(U)$, and complements the results in figure 14 and the analysis in Appendix D.

Finally, we consider the governing equations for the linear channel flow with modally-stable time-varying base-flow

$$\frac{\partial \mathbf{u}'}{\partial t} = \tilde{\mathcal{L}}(U) \mathbf{u}', \quad (\text{F } 3a)$$

$$\mathbf{U} = (U(y, z, t), 0, 0) \text{ from case R180,} \quad (\text{F } 3b)$$

where base flow is now allowed to change in time. The system (F 3) is supported by transient growth potentially assisted by parametric instabilities. Thus, turbulence could survive even if $\tilde{\mathcal{L}}(U)$ is modally stable at all instances. However, we found that this is not the case and (F 3) is unable to sustain turbulence: \mathbf{u}' decays after a few eddy turnover times.

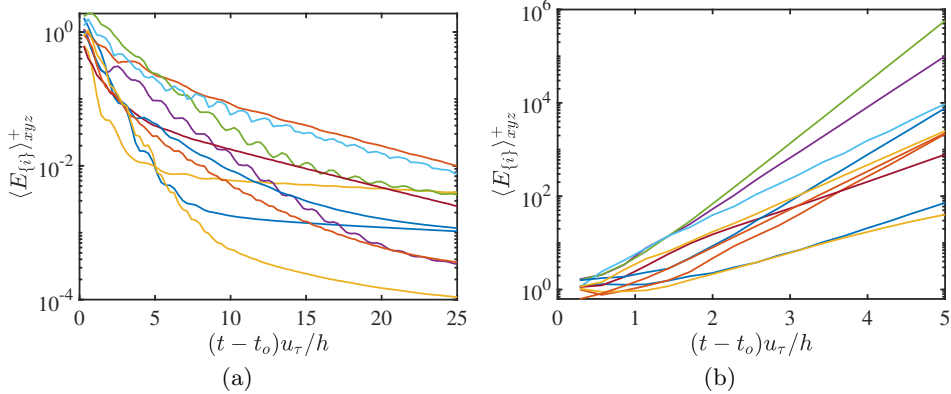


Figure 36: The history of the domain-averaged turbulent kinetic energy of the fluctuations $\langle E \rangle_{xyz}$. Different colours are for cases for (a) modally-stable system (F1) and (b) modally-unstable system (F2). t_0 is initial time to integrate the system.

REFERENCES

- ADRIAN, R. J. 2007 Hairpin vortex organization in wall turbulence. *Phys. Fluids* **19** (4), 041301.
- AHMADI, MO., VALMORBIDA, G., GAYME, D. & PAPACHRISTODOULOU, A. 2019 A framework for inputoutput analysis of wall-bounded shear flows. *J. Fluid Mech.* **873**, 742–785.
- ALIZARD, FRÉDÉRIC 2015 Linear stability of optimal streaks in the log-layer of turbulent channel flows. *Phys. Fluids* **27** (10), 105103.
- ANDERSSON, P., BRANDT, L., BOTTARO, A. & HENNINGSON, D. S. 2001 On the breakdown of boundary layer streaks. *J. Fluid Mech.* **428**, 29–60.
- ASAI, MASAHIKO, MINAGAWA, MASAYUKI & NISHIOKA, MICHIO 2002 The instability and breakdown of a near-wall low-speed streak. *J. Fluid Mech.* **455**, 289–314.
- BAE, H. J., ENCINAR, M. P. & LOZANO-DURÁN, A. 2018a Causal analysis of self-sustaining processes in the logarithmic layer of wall-bounded turbulence. *J. Phys.: Conf. Series* **1001**, 012013.
- BAE, H. J., LOZANO-DURÁN, A., BOSE, S. T. & MOIN, P. 2018b Turbulence intensities in large-eddy simulation of wall-bounded flows. *Phys. Rev. Fluids* **3**, 014610.
- BAE, H. J., LOZANO-DURÁN, A., BOSE, S. T. & MOIN, P. 2019 Dynamic slip wall model for large-eddy simulation. *J. Fluid Mech.* **859**, 400–432.
- BATCHELOR, G. K. & PROUDMAN, IAN 1954 The effect of rapid distortion of a fluid in turbulent motion. *The Quarterly Journal of Mechanics and Applied Mathematics* **7** (1), 83–103.
- BEEBEE, H., HITCHCOCK, C. & MENZIES, P. 2012 *The Oxford Handbook of Causation*. OUP Oxford.
- BOTTARO, A & KLINGMANN, G. B. 1996 On the linear breakdown of görler vortices. *Eur. J. Mech. B/Fluids* **15**, 301.
- BRETHEIM, J. U., MENEVEAU, C. & GAYME, D. F. 2018 A restricted nonlinear large eddy simulation model for high Reynolds number flows. *J. Turb.* **19** (2), 141–166.
- BROWN, GARRY L. & ROSHKO, ANATOL 1974 On density effects and large structure in turbulent mixing layers. *J. Fluid Mech.* **64** (4), 775–816.
- BROWN, GARRY L. & THOMAS, ANDREW S. W. 1977 Large structure in a turbulent boundary layer. *Phys. Fluids* **20** (10), S243–S252.
- BUTLER, K. M. & FARRELL, B. F. 1993 Optimal perturbations and streak spacing in wall-bounded turbulent shear flow. *Phys. Fluids A* **5**, 774.
- CAMBON, CLAUDE & SCOTT, JULIAN F. 1999 Linear and nonlinear models of anisotropic turbulence. *Annu. Rev. Fluid Mech.* **31** (1), 1–53.
- CASSINELLI, ANDREA, DE GIOVANETTI, MATTEO & HWANG, YONGYUN 2017 Streak instability in near-wall turbulence revisited. *J. Turb.* **18** (5), 443–464.

- CHERNYSHENKO, S. I. & BAIG, M. F. 2005 The mechanism of streak formation in near-wall turbulence. *J. Fluid Mech.* **544**, 99–131.
- CHINI, G. P., MONTEMURO, B., WHITE, C. M. & KLEWICKI, J. 2017 A self-sustaining process model of inertial layer dynamics in high Reynolds number turbulent wall flows. *Philos. Trans. Royal Soc. A* **375** (2089), 20160090.
- CHOI, K.-S. & CLAYTON, B. R. 2001 The mechanism of turbulent drag reduction with wall oscillation. *Int. J. Heat Fluid Fl.* **22** (1), 1–9.
- CONSTANTINOU, N C, LOZANO-DURÁN, A, NIKOLAIDIS, M-A, FARRELL, B F, IOANNOU, P J & JIMÉNEZ, J 2014 Turbulence in the highly restricted dynamics of a closure at second order: comparison with DNS. *J. Phys.: Conf. Series* **506**, 012004.
- COSSU, C. & HWANG, Y. 2017 Self-sustaining processes at all scales in wall-bounded turbulent shear flows. *Philos. Trans. Royal Soc. A* **375** (2089).
- COSSU, C., PUJALS, G. & DEPARDON, S. 2009 Optimal transient growth and very large-scale structures in turbulent boundary layers. *J. Fluid Mech.* **619**, 79–94.
- DEGUCHI, KENGO & HALL, PHILIP 2015 Free-stream coherent structures in growing boundary layers: a link to near-wall streaks. *J. Fluid Mech.* **778**, 451–484.
- DEGUCHI, KENGO, HALL, PHILIP & WALTON, ANDREW 2013 The emergence of localized vortexwave interaction states in plane couette flow. *J. Fluid Mech.* **721**, 58–85.
- DEL ÁLAMO, J. C. & JIMÉNEZ, J. 2006 Linear energy amplification in turbulent channels. *J. Fluid Mech.* **559**, 205–213.
- EBERHARDT, FREDERICK & SCHEINES, RICHARD 2007 Interventions and causal inference. *Philosophy of Science* **74** (5), 981–995.
- EICHLER, MICHAEL 2013 Causal inference with multiple time series: principles and problems. *Philos. Trans. Royal Soc. A* **371** (1997), 20110613, arXiv: <https://royalsocietypublishing.org/doi/pdf/10.1098/rsta.2011.0613>.
- ELLINGSEN, T. & PALM, E. 1975 Stability of linear flow. *Phys. Fluids* **18** (4), 487–488.
- ENCINAR, MIGUEL P. & JIMÉNEZ, JAVIER 2020 Momentum transfer by linearised eddies in turbulent channel flows. *J. Fluid Mech.* **895**, A23.
- FARRELL, B. F., GAYME, D. F. & IOANNOU, P. J. 2017a A statistical state dynamics approach to wall turbulence. *Philos. Trans. Royal Soc. A* **375** (2089), 20160081.
- FARRELL, B. F. & IOANNOU, P. J. 1993a Optimal excitation of three-dimensional perturbations in viscous constant shear flow. *Physics of Fluids A: Fluid Dynamics* **5** (6), 1390–1400.
- FARRELL, BRIAN F. & IOANNOU, PETROS J. 1993b Stochastic forcing of the linearized navierstokes equations. *Phys. Fluids* **5** (11), 2600–2609.
- FARRELL, B. F. & IOANNOU, P. J. 1996 Generalized stability theory. Part I: Autonomous operators. *J. Atmos. Sci.* **53** (14), 2025–2040.
- FARRELL, B. F. & IOANNOU, P. J. 1999 Perturbation growth and structure in time dependent flows. *J. Atmos. Sci.* (56), 3622–3639.
- FARRELL, B. F. & IOANNOU, P. J. 2012 Dynamics of streamwise rolls and streaks in turbulent wall-bounded shear flow. *J. Fluid Mech.* **708**, 149–196.
- FARRELL, BRIAN F. & IOANNOU, PETROS J. 2019 Statistical state dynamics: A new perspective on turbulence in shear flow. *Zonal Jets Phenomenology, Genesis, and Physics*. pp. 380–400.
- FARRELL, B. F., IOANNOU, P. J., JIMÉNEZ, J., CONSTANTINOU, N. C., LOZANO-DURÁN, A. & NIKOLAIDIS, M.-A. 2016 A statistical state dynamics-based study of the structure and mechanism of large-scale motions in plane Poiseuille flow. *J. Fluid Mech.* **809**, 290–315.
- FARRELL, BRIAN F., IOANNOU, PETROS J. & NIKOLAIDIS, MARIOS-ANDREAS 2017b Instability of the roll-streak structure induced by background turbulence in pretransitional couette flow. *Phys. Rev. Fluids* **2**, 034607.
- FISHER, RONALD AYLMER 1936 Design of experiments. *Br Med J* **1** (3923), 554–554.
- FLORES, O. & JIMÉNEZ, J. 2010 Hierarchy of minimal flow units in the logarithmic layer. *Phys. Fluids* **22** (7), 071704.
- GIBSON, J. F., HALCROW, J. & CVITANOVÍČ, P. 2009 Equilibrium and travelling-wave solutions of plane Couette flow. *J. Fluid Mech.* **638**, 243–266.
- DE GIOVANETTI, M., SUNG, H.J. & HWANG, Y. 2017 Streak instability in turbulent channel flow: the seeding mechanism of large-scale motions. *J. Fluid Mech.* **832**, 483–513.

- GUSTAVSSON, L. H. 1991 Energy growth of three-dimensional disturbances in plane Poiseuille flow. *J. Fluid Mech.* **224**, 241–260.
- HACK, M. J. P. & MOIN, P. 2018 Coherent instability in wall-bounded shear. *J. Fluid Mech.* **844**, 917–955.
- HACK, M. J. P. & ZAKI, T. A. 2014 Streak instabilities in boundary layers beneath free-stream turbulence. *J. Fluid Mech.* **741**, 280–315.
- HALL, P. 2018 Vortex-wave interaction arrays: a sustaining mechanism for the log layer? *J. Fluid Mech.* **850**, 46–82.
- HALL, PHILIP & SHERWIN, SPENCER 2010 Streamwise vortices in shear flows: harbingers of transition and the skeleton of coherent structures. *J. Fluid Mech.* **661**, 178–205.
- HALL, P. & SMITH, F. T. 1988 The nonlinear interaction of Tollmien–Schlichting waves and Taylor-Görtler vortices in curved channel flows. *Proc. Royal Soc. Lond* **417** (1853), 255–282.
- HALL, P. & SMITH, F. T. 1991 On strongly nonlinear vortex/wave interactions in boundary-layer transition. *J. Fluid Mech.* **227**, 641–666.
- HAMILTON, J. M., KIM, J. & WALEFFE, F. 1995 Regeneration mechanisms of near-wall turbulence structures. *J. Fluid Mech.* **287**, 317–348.
- HØPFNER, JÉRÔME, BRANDT, LUCA & HENNINGDON, DAN S. 2005 Transient growth on boundary layer streaks. *J. Fluid Mech.* **537**, 91–100.
- HÖGBERG, M., BEWLEY, T. R. & HENNINGSON, D. S. 2003 Linear feedback control and estimation of transition in plane channel flow. *J. Fluid Mech.* **481**, 149–175.
- HUSSAIN, A. K. M. F. & REYNOLDS, W. C. 1970 The mechanics of an organized wave in turbulent shear flow. *J. Fluid Mech.* **41** (2), 241–258.
- HWANG, Y. & COSSU, C. 2010a Amplification of coherent streaks in the turbulent Couette flow: an input–output analysis at low Reynolds number. *J. Fluid Mech.* **643**, 333–348.
- HWANG, Y. & COSSU, C. 2010b Linear non-normal energy amplification of harmonic and stochastic forcing in the turbulent channel flow. *J. Fluid Mech.* **664**, 51–73.
- HWANG, Y. & COSSU, C. 2010c Self-sustained process at large scales in turbulent channel flow. *Phys. Rev. Lett.* **105**, 044505.
- HWANG, Y. & COSSU, C. 2011 Self-sustained processes in the logarithmic layer of turbulent channel flows. *Phys. Fluids* **23** (6), 061702.
- HWANG, Y., WILLIS, A. P. & COSSU, C. 2016 Invariant solutions of minimal large-scale structures in turbulent channel flow for Re_τ up to 1000. *J. Fluid Mech.* **802**, R1.
- HYTTINEN, ANTTI, EBERHARDT, FREDERICK & HOYER, PATRIK O. 2013 Experiment selection for causal discovery. *Journal of Machine Learning Research* **2013** (14), 3041–3071.
- JIMÉNEZ, J. 1987 Coherent structures and dynamical systems. *CTR - Proc. Summer Prog.* pp. 323–324.
- JIMÉNEZ, J. 2012 Cascades in wall-bounded turbulence. *Annu. Rev. Fluid Mech.* **44**, 27–45.
- JIMÉNEZ, J. 2013 How linear is wall-bounded turbulence? *Phys. Fluids* **25**, 110814.
- JIMÉNEZ, J. 2015 Direct detection of linearized bursts in turbulence. *Phys. Fluids* **27** (6), 065102.
- JIMÉNEZ, J. 2018 Coherent structures in wall-bounded turbulence. *J. Fluid Mech.* **842**, P1.
- JIMÉNEZ, JAVIER 2018 Machine-aided turbulence theory. *J. Fluid Mech.* **854**, R1.
- JIMÉNEZ, JAVIER 2020 Monte carlo science. *J. Turb.* **0** (0), 1–23.
- JIMÉNEZ, J., KAWAHARA, G., SIMENS, M. P., NAGATA, M. & SHIBA, M. 2005 Characterization of near-wall turbulence in terms of equilibrium and “bursting” solutions. *Phys. Fluids* **17** (1), 015105.
- JIMÉNEZ, J. & MOIN, P. 1991 The minimal flow unit in near-wall turbulence. *J. Fluid Mech.* **225**, 213–240.
- JIMÉNEZ, J. & PINELLI, A. 1999 The autonomous cycle of near-wall turbulence. *J. Fluid Mech.* **389**, 335–359.
- JOVANOVIĆ, MIHAJLO R 2020 From bypass transition to flow control and data-driven turbulence modeling: An input-output viewpoint. *arXiv preprint arXiv:2003.10104*.
- JOVANOVIĆ, MIHAJLO R. & BAMIEH, BASSAM 2005 Componentwise energy amplification in channel flows. *J. Fluid Mech.* **534**, 145–183.
- JUNG, WJ, MANGIAVACCHI, N & AKHAVAN, R 1992 Suppression of turbulence in wall-bounded

- flows by high-frequency spanwise oscillations. *Physics of Fluids A: Fluid Dynamics* **4** (8), 1605–1607.
- KARP, MICHAEL & COHEN, JACOB 2014 Tracking stages of transition in Couette flow analytically. *J. Fluid Mech.* **748**, 896–931.
- KARP, M. & COHEN, J. 2017 On the secondary instabilities of transient growth in Couette flow. *J. Fluid Mech.* **813**, 528–557.
- KARP, MICHAEL & HACK, M. J. PHILIPP 2018 Transition to turbulence over convex surfaces. *J. Fluid Mech.* **855**, 1208–1237.
- KAWAHARA, G., JIMÉNEZ, J., UHLMANN, M. & PINELLI, A. 2003 Linear instability of a corrugated vortex sheet – a model for streak instability. *J. Fluid Mech.* **483**, 315–342.
- KAWAHARA, G. & KIDA, S. 2001 Periodic motion embedded in plane Couette turbulence: regeneration cycle and burst. *J. Fluid Mech.* **449**, 291–300.
- KAWAHARA, G., UHLMANN, M. & VAN VEEN, L. 2012 The significance of simple invariant solutions in turbulent flows. *Annu. Rev. Fluid Mech.* **44** (1), 203–225.
- KIM, J. & BEWLEY, T. R. 2006 A linear systems approach to flow control. *Annu. Rev. Fluid Mech.* **39**, 383–417.
- KIM, J., KLINE, S. J. & REYNOLDS, W. C. 1971 The production of turbulence near a smooth wall in a turbulent boundary layer. *J. Fluid Mech.* **50**, 133–160.
- KIM, JOHN & LIM, JUNWOO 2000 A linear process in wall-bounded turbulent shear flows. *Phys. Fluids* **12** (8), 1885–1888.
- KIM, J. & MOIN, P. 1985 Application of a fractional-step method to incompressible Navier–Stokes equations. *J. Comp. Phys.* **59**, 308–323.
- KLEBANOFF, P. S., TIDSTROM, K. D. & SARGENT, L. M. 1962 The three-dimensional nature of boundary-layer instability. *J. Fluid Mech.* **12** (1), 1–34.
- KLINE, S. J., REYNOLDS, W. C., SCHRAUB, F. A. & RUNSTADLER, P. W. 1967 The structure of turbulent boundary layers. *J. Fluid Mech.* **30** (4), 741–773.
- KREILOS, T. & ECKHARDT, B. 2012 Periodic orbits near onset of chaos in plane Couette flow. *Chaos* **22** (4), 047505.
- LAADHARI, F., SKANDAJI, L & MOREL, R. 1994 Turbulence reduction in a boundary layer by a local spanwise oscillating surface. *Phys. Fluids* **6** (10), 3218–3220.
- LANDAHL, M. T. 1975 Wave breakdown and turbulence. *SIAM J. Appl. Math.* **28**, 735–756.
- LANDAHL, M. T. 1990 On sublayer streaks. *J. Fluid Mech.* **212**, 593–614.
- LEE, M. J., KIM, J. & MOIN, P. 1990 Structure of turbulence at high shear rate. *J. Fluid Mech.* **216**, 561–583.
- LI, FEI & MALIK, MUJEEB R. 1995 Fundamental and subharmonic secondary instabilities of görtler vortices. *J. Fluid Mech.* **297**, 77–100.
- LIANG, X. S. & LOZANO-DURÁN, A. 2017 A preliminary study of the causal structure in fully developed near-wall turbulence. *CTR - Proc. Summer Prog.* pp. 233–242.
- LOZANO-DURÁN, A. & BAE, H.J. 2019 Characteristic scales of Townsend's wall-attached eddies. *J. Fluid Mech.* **868**, 698–725.
- LOZANO-DURÁN, A., BAE, H.J. & ENCINAR, M.P. 2019 Causality of energy-containing eddies in wall turbulence. *J. Fluid Mech.* **882**, A2.
- LOZANO-DURÁN, A. & BAE, H. J. 2016 Turbulent channel with slip boundaries as a benchmark for subgrid-scale models in LES. *Center for Turbulence Research - Annual Research Briefs* pp. 97–103.
- LOZANO-DURÁN, A. & JIMÉNEZ, J. 2014 Time-resolved evolution of coherent structures in turbulent channels: characterization of eddies and cascades. *J. Fluid. Mech.* **759**, 432–471.
- LOZANO-DURÁN, A., KARP, M. & CONSTANTINOU, N. C. 2018 Wall turbulence with constrained energy extraction from the mean flow. *Center for Turbulence Research - Annual Research Briefs* pp. 209–220.
- LOZANO-DURÁN, A., NIKOLAIDIS, M.-A., CONSTANTINOU, N. C. & KARP, M. 2020 Alternative physics to understand wall turbulence: Navier–Stokes equations with modified linear dynamics. *J. Phys.: Conf. Ser.* **1522** (012003), in press.
- MALKUS, W. V. R. 1956 Outline of a theory of turbulent shear flow. *J. Fluid Mech.* **1** (5), 521–539.

- MARQUILLIE, M., EHRENSTEIN, U. & LAVAL, J.-P. 2011 Instability of streaks in wall turbulence with adverse pressure gradient. *J. Fluid Mech.* **681**, 205–240.
- MCKEON, B. J. 2017 The engine behind (wall) turbulence: perspectives on scale interactions. *J. Fluid Mech.* **817**, P1.
- MCKEON, B. J. & SHARMA, A. S. 2010 A critical-layer framework for turbulent pipe flow. *J. Fluid Mech.* **658**, 336–382.
- MOARREF, RASHAD, SHARMA, ATI S., TROPP, JOEL A. & MCKEON, BEVERLEY J. 2013 Model-based scaling of the streamwise energy density in high-Reynolds-number turbulent channels. *J. Fluid Mech.* **734**, 275–316.
- MONTEMURO, BRANDON, WHITE, CHRISTOPHER M., KLEWICKI, JOSEPH C. & CHINI, GREGORY P. 2020 A self-sustaining process theory for uniform momentum zones and internal shear layers in high reynolds number shear flows, arXiv: 2006.15801.
- MORRA, P., SEMERARO, O., HENNINGSON, D. S. & COSSU, C. 2019 On the relevance of Reynolds stresses in resolvent analyses of turbulent wall-bounded flows. *J. Fluid Mech.* **867**, 969–984.
- NAGATA, M. 1990 Three-dimensional finite-amplitude solutions in plane Couette flow: bifurcation from infinity. *J. Fluid Mech.* **217**, 519–527.
- NIKOLAIDIS, M.-A., FARRELL, B. F., IOANNOU, P. J., GAYME, D. F., LOZANO-DURÁN, A. & JIMÉNEZ, J. 2016 A POD-based analysis of turbulence in the reduced nonlinear dynamics system. *J. Phys.: Conf. Series* **708**, 012002.
- ORLANDI, P. 2000 *Fluid Flow Phenomena: A Numerical Toolkit*. Springer.
- ORR, W. M'F. 1907 The stability or instability of the steady motions of a perfect liquid and of a viscous liquid. Part II: A viscous liquid. *Math. Proc. Royal Ir. Acad.* **27**, 69–138.
- PANTON, R. L. 2001 Overview of the self-sustaining mechanisms of wall turbulence. *Prog. Aerosp. Sci.* **37** (4), 341–383.
- PARK, DANIEL S. & HUERRE, PATRICK 1995 Primary and secondary instabilities of the asymptotic suction boundary layer on a curved plate. *J. Fluid Mech.* **283**, 249–272.
- PARK, JUNHO, HWANG, YONGYUN & COSSU, CARLO 2011 On the stability of large-scale streaks in turbulent Couette and Poiseulle flows. *Comptes Rendus Mécanique* **339** (1), 1 – 5.
- PARK, JAE SUNG & GRAHAM, MICHAEL D. 2015 Exact coherent states and connections to turbulent dynamics in minimal channel flow. *J. Fluid Mech.* **782**, 430–454.
- PEARL, J. 2009 *Causality: Models, Reasoning and Inference*, 2nd edn. New York, NY, USA: Cambridge University Press.
- PHILLIPS, W. R. C., WU, Z. & LUMLEY, J. L. 1996 On the formation of longitudinal vortices in a turbulent boundary layer over wavy terrain. *J. Fluid Mech.* **326**, 321–341.
- PUJALS, G., GARCÍA-VILLALBA, M., COSSU, C. & DEPARDON, S. 2009 A note on optimal transient growth in turbulent channel flows. *Phys. Fluids* **21** (1), 015109.
- REDDY, S. C. & HENNINGSON, D. S. 1993 Energy growth in viscous channel flows. *J. Fluid Mech.* **252**, 209–238.
- REDDY, S. C., SCHMID, P. J., BAGGETT, J. S. & HENNINGSON, D. S. 1998 On the stability of streamwise streaks and transition thresholds in plane channel flows. *J. Fluid Mech.* **365**, 269–303.
- REED, H L, SARIC, W S & ARNAL, D 1996 Linear stability theory applied to boundary layers. *Annu. Rev. Fluid Mech.* **28** (1), 389–428.
- REYNOLDS, W. C. & TIEDERMAN, W. G. 1967 Stability of turbulent channel flow, with application to malkus's theory. *J. Fluid Mech.* **27** (2), 253–272.
- RICCO, P. & QUADRID, M. 2008 Wall-oscillation conditions for drag reduction in turbulent channel flow. *Int. J. Heat Fluid Fl.* **29** (4), 891 – 902.
- RICHARDSON, L.F. 1922 *Weather Prediction by Numerical Process*. Cambridge University Press.
- ROBINSON, S K 1991 Coherent motions in the turbulent boundary layer. *Annu. Rev. Fluid Mech.* **23** (1), 601–639.
- ROWLEY, CLARENCE W. & DAWSON, SCOTT T.M. 2017 Model reduction for flow analysis and control. *Annu. Rev. Fluid Mech.* **49** (1), 387–417.
- RUGH, WILSON J. 1996 *Linear System Theory (2nd Ed.)*. USA: Prentice-Hall, Inc.
- SARIC, WILLIAM S., REED, HELEN L. & WHITE, EDWARD B. 2003 Stability and transition of three-dimensional boundary layers. *Annual Review of Fluid Mechanics* **35** (1), 413–440.

- SCHMID, P.J. & HENNINGSON, D.S. 2012 *Stability and Transition in Shear Flows*. Springer New York.
- SCHMID, PETER J. 2007 Nonmodal stability theory. *Annu. Rev. Fluid Mech.* **39** (1), 129–162.
- SCHOPPA, W. & HUSSAIN, F. 2002 Coherent structure generation in near-wall turbulence. *J. Fluid Mech.* **453**, 57–108.
- SKOTE, M., HARITONIDIS, J. H. & HENNINGSON, D. S. 2002 Varicose instabilities in turbulent boundary layers. *Phys. Fluids* **14** (7), 2309–2323.
- SMITS, A. J., MCKEON, B. J. & MARUSIC, I. 2011 High-Reynolds number wall turbulence. *Annu. Rev. Fluid Mech.* **43** (1), 353–375.
- SWEARINGEN, JERRY D. & BLACKWELDER, RON F. 1987 The growth and breakdown of streamwise vortices in the presence of a wall. *J. Fluid Mech.* **182**, 255–290.
- SYMON, SEAN, ROSENBERG, KEVIN, DAWSON, SCOTT T. M. & MCKEON, BEVERLEY J. 2018 Non-normality and classification of amplification mechanisms in stability and resolvent analysis. *Phys. Rev. Fluids* **3**, 053902.
- THOMAS, VAUGHAN L., FARRELL, BRIAN F., IOANNOU, PETROS J. & GAYME, DENNICE F. 2015 A minimal model of self-sustaining turbulence. *Phys. Fluids* **27** (10), 105104.
- TISSOT, G., LOZANO-DURÁN, A., JIMÉNEZ, J., CORDIER, L. & NOACK, B. R. 2014 Granger causality in wall-bounded turbulence. *J. Phys. Conf. Ser.* **506** (1), 012006.
- TOH, SADAYOSHI & ITANO, TOMOAKI 2003 A periodic-like solution in channel flow. *J. Fluid Mech.* **481**, 67–76.
- TOWNE, A., LOZANO-DURÁN, A. & YANG, X. 2020 Resolvent-based estimation of space–time flow statistics. *J. Fluid Mech.* **883**, A17.
- TOWNSEND, A. A. 1976 *The structure of turbulent shear flow*. Cambridge University Press.
- TREFETHEN, LLOYD N., TREFETHEN, ANNE E., REDDY, SATISH C. & DRISCOLL, TOBIN A. 1993 Hydrodynamic stability without eigenvalues. *Science* **261** (5121), 578–584.
- TUERKE, F. & JIMÉNEZ, J. 2013 Simulations of turbulent channels with prescribed velocity profiles. *J. Fluid Mech.* **723**, 587–603.
- VAN VEEN, L. & KAWAHARA, G. 2011 Homoclinic tangle on the edge of shear turbulence. *Phys. Rev. Lett.* **107**, 114501.
- VISWANATH, D. 2007 Recurrent motions within plane couette turbulence. *J. Fluid Mech.* **580**, 339–358.
- WALEFFE, F. 1995 Hydrodynamic stability and turbulence: Beyond transients to a self-sustaining process. *Stud. Appl. Math.* **95** (3), 319–343.
- WALEFFE, F. 1997 On a self-sustaining process in shear flows. *Phys. Fluids* **9** (4), 883–900.
- WALEFFE, F. 2001 Exact coherent structures in channel flow. *J. Fluid Mech.* **435**, 93–102.
- WANG, J., GIBSON, J. & WALEFFE, F. 2007 Lower branch coherent states in shear flows: Transition and control. *Phys. Rev. Lett.* **98**, 204501.
- WEDIN, H. & KERSWELL, R. R. 2004 Exact coherent structures in pipe flow: travelling wave solutions. *J. Fluid Mech.* **508**, 333–371.
- WRAY, A. A. 1990 Minimal-storage time advancement schemes for spectral methods. *Tech. Rep.*, NASA Ames Research Center.
- YU, XIUYANG & LIU, J. T. C. 1991 The secondary instability in goertler flow. *Phys. Fluids* **3** (8), 1845–1847.
- YU, XIUYANG & LIU, JOSEPH T. C. 1994 On the mechanism of sinuous and varicose modes in three-dimensional viscous secondary instability of nonlinear görler rolls. *Phys. Fluids* **6** (2), 736–750.
- ZARE, A., GEORGIOU, T. T. & JOVANOVIĆ, M.R. 2020 Stochastic dynamical modeling of turbulent flows. *Annu. Rev. Control Robot. Auton. Syst.* **3** (1), 195–219.
- ZARE, ARMIN, JOVANOVIĆ, MIHAJLO R. & GEORGIOU, TRYPHON T. 2017 Colour of turbulence. *J. Fluid Mech.* **812**, 636–680.